Copyright
by
Nicholas Ethan Bradley
2014

The Dissertation Committee for Nicholas Ethan Bradley
certifies that this is the approved version of the following dissertation:

Initial Guess and Optimization Strategies for Multi-Body Space Trajectories with Application to Free Return Trajectories to Near-Earth Asteroids

Committee:

Ryan P. Russell, Supervisor

Cesar Ocampo, Co-Supervisor

Wallace Fowler

Bob Schutz

Behcet Acikmese

Shyamkumar Bhaskaran

Initial Guess and Optimization Strategies for Multi-Body Space Trajectories with Application to Free Return Trajectories to Near-Earth Asteroids

by

Nicholas Ethan Bradley, B.S.A.S.E., M.S.

DISSERTATION

Presented to the Faculty of the Graduate School of

The University of Texas at Austin

in Partial Fulfillment

of the Requirements

for the Degree of

DOCTOR OF PHILOSOPHY

THE UNIVERSITY OF TEXAS AT AUSTIN

August 2014

To whom else would this work be dedicated?

"My flesh and my heart may fail, but God is the strength of my heart and my portion forever."

Acknowledgments

The process of pursuing an advanced degree is often long, slow, and tedious work. It takes the insight and wisdom of those around you to provide encouragement and perspective when it is difficult to do so yourself.

Always first and foremost, my thanks are to God, as all things are His to begin with. As the Puritan prayer says, He Himself is "the Gift of Gifts," and no amount of degrees earned, hours worked, or milestones accomplished can ever compare to the gift of life and grace through Jesus.

I am so thankful for my beautiful wife Rachel. We managed to pull off three years of a long-distance, Colorado-to-Texas relationship while dating and engaged, and she has been so patient, loving, kind, and caring through the entire process of my time at UT. Now through a year of marriage, she continues to amaze me with her knowledge, her kindness, her love of God, her compassion, and her culinary skills. Life is an adventure with my wonderful wife at my side.

My family has always cultivated a love for learning and of pursuing passions and dreams. I can't imagine growing up with a more loving family than with my Mom, Dad, sister Lindsey, and my grandparents. I want to specifically thank and acknowledge my grandfather for being the first in the family to earn a doctoral degree. He has always been an academic inspiration to me.

So many friends have walked along this path with me, both near and far away, both inside and outside my engineering sphere. I want to thank all my friends, whether in Colorado, Texas, or elsewhere. They continually give me life perspective, and I have never felt a lack of community and support.

I would like to thank both advisors that I have worked with during my time at UT. Dr. Ocampo brought me into his research program during my first year as a doctoral student, and he introduced me to the idea of free returns to asteroids. From the beginning, he was very instrumental in my research direction, and he has always invested his time and interest in the well-being of his students as a whole. Dr. Russell has been my advisor for the past year, and took me into his research program during an extremely busy time in his career. I am grateful to him for collaborating on the continuation work, for providing career and research guidance, and for helping me navigate my final year as a student.

I have served as a teaching assistant for six semesters at UT, and I am thankful both to the Department of Aerospace Engineering and to the faculty members with whom I worked for providing me the opportunity to interact with students, to earn a living, and to practice teaching. I am sure that the skills that I learned in classroom interaction and preparation will serve me well through my career and the rest of my life.

Finally, I am very thankful for the sources of funding that I have received through the Department of Aerospace Engineering and Engineering Mechanics and the Cockrell School of Engineering: the Warren A. and Alice L. Meyer Endowed Scholarship in Engineering, the Thrust 2000 Fellowship, and others. Without these

sources of funding, obtaining my degree would likely have been prohibitively difficult, and I am so grateful for donors and sponsors who recognize the value of an education. I hope to return the favor someday to a future generation of engineers and learners.

Initial Guess and Optimization Strategies for Multi-Body Space Trajectories with Application to Free Return Trajectories to Near-Earth Asteroids

Publication No. _____

Nicholas Ethan Bradley, Ph.D.
The University of Texas at Austin, 2014

Supervisors: Ryan P. Russell
Cesar Ocampo

This concept of calculating, optimizing, and utilizing a trajectory known as a "Free Return Trajectory" to facilitate spacecraft rendezvous with Near-Earth Asteroids is presented in this dissertation. A Free Return Trajectory may be defined as a trajectory that begins and ends near the same point, relative to some central body, without performing any deterministic velocity maneuvers (i.e., no maneuvers are planned in a theoretical sense for the nominal mission to proceed). Free Return Trajectories have been utilized previously for other purposes in astrodynamics, but they have not been previously applied to the problem of Near-Earth Asteroid rendezvous.

Presented here is a series of descriptions, algorithms, and results related to trajectory initial guess calculation and optimal trajectory convergence. First, Earth-

centered Free Return Trajectories are described in a general manner, and these trajectories are classified into several families based on common characteristics. Next, these trajectories are used to automatically generate initial conditions in the three-body problem for the purpose of Near-Earth Asteroid rendezvous. For several bodies of interest, example initial conditions are automatically generated, and are subsequently converged, resulting in feasible, locally-optimal, round-trip trajectories to Near-Earth Asteroids utilizing Free Return Trajectories. Subsequently, a study is performed on using an unpowered flyby of the Moon to lower the overall Δv cost for a nominal round-trip voyage to a Near-Earth Asteroid. Using the Moon is shown to appreciably decrease the overall mission cost.

In creating the formulation and algorithms for the Lunar flyby problem, an initial guess routine for generic planetary and lunar flyby tours was developed. This continuation algorithm is presented next, and details a novel process by which ballistic trajectories in a simplistic two-body force model may be iteratively converged in progressively more realistic dynamical models until a final converged ballistic trajectory is found in a full-ephemeris, full-dynamics model. This procedure is useful for constructing interplanetary transfers and moon tours in a realistic dynamical framework; an interplanetary and an inter-moon example are both shown.

To summarize, the material in this dissertation consists of: novel algorithms to compute Free Return Trajectories, and application of the concept to Near-Earth Asteroid rendezvous; demonstration of cost-savings by using a Lunar flyby; and a novel routine to transfer trajectories from a simplistic model to a more realistic dynamical representation.

Table of Contents

List of Tables

List of Figures

Chapter 1

Introduction and Literature Review

1.1 Problem definition

Near-Earth Asteroid (NEA) rendezvous has been a salient literature topic in astrodynamics for decades. Many authors have presented novel methods to reach these bodies, with solutions ranging from fast, direct transfers to spiraling solar sail spacecraft orbits. With increased interest in sending a manned mission to an NEA, it has become important to determine methods of reaching NEAs that are not only viable from a fuel or time perspective, but that also incorporate an element of safety.

A Free Return Trajectory (FRT) may be defined broadly as a trajectory that returns at or near its departure point after a finite amount of time without incorporating deterministic (planned) maneuvers or gravitational flybys. Further, we may consider FRTs in an Earth-centered interplanetary sense to only incorporate those trajectories that begin near the Earth, escape the Earth's immediate gravitational influence, and return to a point near the Earth without deterministic maneuvers. The starting and ending points do not have to coincide, nor is the trajectory required to be periodic (as may be the case with a halo or Lyapunov orbit, which may be considered to be free return in a different sense). These trajectories have been previously researched for manned missions, and have notably been incorporated in

the mission design for the Apollo missions to send humans to the Moon and return them safely to the Earth.

The most important contribution of an FRT is the risk reduction aspect. If a catastrophic failure occurs where an engine is rendered ineffective or useless, the spacecraft may remain on the FRT and return safely near its starting point. An FRT may be designed such that its return state is in a re-entry corridor in Earth's atmosphere. If an abort becomes necessary where the engine cannot be used, the spacecraft will return to the desired re-entry corridor. One disadvantage to using FRTs in mission design is that they tend to produce longer mission timelines and often incur a higher fuel cost to achieve desired objectives. Of course, eliminating the constraint of incorporating an FRT means that these costs may be lowered in the final mission design. The decision to use an FRT in actual mission design presents a qualitative trade-off between cost of consumables (fuel, food for humans, etc.) and overall mission safety by presenting a simple abort option.

At its core, this dissertation presents a study of how to obtain initial guesses and converged optimal solutions for FRTs as a method of reaching NEAs. In order to understand FRT transfers to NEAs, it is important to first understand FRTs in a destination-independent sense; that is, without regarding the ultimate goal of visiting an NEA, how FRTs are computed and how may they be classified. Previous work has been conducted extensively on both FRTs in general and NEA rendezvous, both of which are discussed in the literature review section. However, a systematic method of computing FRTs, classifying them into families, and utilizing these families to reach NEAs has not previously been presented.

As part of the work presented here, initial guesses of trajectories must be constructed at intermediate steps before a final, converged solution may be realized. While developing methods of obtaining initial guesses, an algorithm was developed using continuation methods that facilitates the conversion of point-mass patched conics trajectories to full-ephemeris trajectories in an actual dynamical system. This topic is presented as a standalone chapter at the end of the dissertation. In essence, the chapter addresses the problem of obtaining high-quality numerically integrated trajectories from the quickly-calculated and intuitive design space of the patched conics framework. Multiple methods have been previously presented on the topic of trajectory fidelity conversion, which are discussed in the literature review chapter. The method presented here is shown to function for interplanetary and inter-moon transfer trajectories, with the ability to chain multiple sequences together to obtain longer integrated trajectories.

The initial guess method may eventually be applied to the FRT-to-NEA solutions to obtain fully integrated trajectories that incorporate the full solar system dynamics, including actual asteroid masses. The method is presented here as a standalone approach for converting low-fidelity trajectories into high-fidelity models, and may be used for many other applications beyond NEA rendezvous.

1.2 Contributions

In an international effort to continue to explore our solar system with robotic and manned spacecraft, it is important to continually develop novel methods to reach bodies that have not previously been visited. The work in this dissertation

contributes a new method of reaching NEAs by utilizing FRTs; both NEA rendezvous and FRT utilization are not new concepts, but using FRTs specifically to reach NEAs has not previously been discussed. The calculations presented here are intended to be an overview of the types of mission profiles that are feasible for this sort of mission. However, the algorithms and intermediate results are applicable to a wide variety of other astrodynamical problems, such as interplanetary tour trajectory generation, periodic orbit calculation, and determination of reachable domains.

Of particular use outside of this dissertation is the continuation method chapter, which applies a continuation algorithm to low-fidelity trajectories to obtain trajectories in high-fidelity dynamics. Continuation as a broad topic is widely useful in fields outside of astrodynamics; the implementation of continuation may be useful for interplanetary and inter-moon tour generation, and orbit-to-orbit transfers in unstable dynamical environments.

Overall, the contribution of this dissertation is to present a trajectory-based risk reduction method of reaching NEAs, and to provide numerical and computational methods useful for computing these trajectories, as well as other related trajectories.

1.3 Organization of the dissertation

This dissertation is organized into several chapters. The first chapter is this introduction, giving a broad overview of the contributions of the work presented in this document, and continuing with a summary of the relevant literature on the topics of NEA rendezvous, FRT usage, continuation methods, and other previously

conducted work. Chapter 2 provides a brief summary of the dynamical models used in the dissertation, and gives constants and equations of motion.

Chapter 3 introduces the novel work of this dissertation with a discussion of destination-independent Earth-centered FRTs. In a two-body sense, FRTs are shown for half-, full-, resonant, and n-revolution cases. These trajectories are shown to exist in the Circular Restricted Three-Body Problem (CRTBP), and an algorithm is presented to obtain other CRTBP FRTs. The characteristics of these FRTs are examined, and the trajectories are classified by families.

Chapter 4 applies the trajectories found in Chapter 3 to the concept of NEA rendezvous. An algorithm is presented to automatically determine an initial guess in the CRTBP for NEA rendezvous with an FRT. Examples of initial guesses are shown, and these initial guesses are subsequently converged into locally-optimal solutions. Five NEA rendezvous cases are given, each for a different highly-accessible asteroid.

Chapter 5 investigates the concept of using a Lunar flyby to decrease the overall Δv cost of entering into an FRT for the purposes of NEA rendezvous. An initial guess is obtained and subsequently converged to rendezvous with one of the NEAs visited in Chapter 4, and the total mission Δv is shown to decrease substantially.

Chapter 6 presents the continuation method of converting an initial guess in a two-body patched conics framework to an n-body, full-ephemeris, fully-integrated trajectory. The work in this chapter developed from an effort to determine appropriate initial guesses for the Lunar flyby problem in Chapter 5, but the chapter stands alone as a method that is applicable to problems beyond NEA rendezvous

and FRT generation. The algorithm involves the creation of an auxiliary "Keplerian ephemeris," which is an approximation of the full body ephemerides for a system in a two-body framework. Utilizing this ephemeris and continuation techniques, the method is applied to interplanetary transfer and inter-moon transfer in the Jovian moon system, converting low-fidelity patched conics trajectories to fully-integrated full-ephemeris trajectories.

Finally, a conclusions chapter is presented that summarizes the novel and relevant findings of this dissertation. Appendices at the end of the dissertation contain analytical gradients utilized in the optimization procedures, which may be useful to researchers studying optimization of similar dynamical systems. Ancillary data is also provided in the Appendices.

1.4 Literature Review

The literature on the topic of numerical algorithms to generate specific classes of astrodynamical trajectories is quite rich, given that the topic is so broad. Ever since the early days of space exploration, engineers have produced novel theories and algorithms for reaching solar system bodies in creative and efficient ways.

The topics covered in this dissertation are not entirely without precedent. Although the combination and application of the information used is a novel contribution to the field, each separate topic is covered by a history of literature and previous work. This chapter contains some of the most pertinent work previously conducted on each topic utilized in this work, separated by subject. Within the chap-

ters of the dissertation, the sections in this chapter are referred to for background information and previous work conducted on each topic.

1.4.1 Asteroids as destinations

In recent decades, the idea of sending humans to asteroids (either Near-Earth Asteroids [NEAs] or main belt asteroids) has garnered much attention, as evidenced by such missions as NASA's current ARM (Asteroid Redirect Mission) proposal. A long-term goal of the space community is to send humans to Mars, and asteroids are seen as a logical technological stepping stone in reaching this goal. This dissertation is focused heavily toward applications of astrodynamical algorithms to reach NEAs, given the current direction of the space community's research and development efforts. Over the course of the last several decades, many authors have recognized this trend and have worked to identify candidate NEAs that make for good destinations. Various metrics are employed to determine what constitutes a "good" target NEA, with aspects such as low fuel usage, low travel time, body size, or body composition. Some pertinent works are summarized here with the intent of showing the variety of the literature on destination choice. Although this dissertation does not discuss destination choice extensively, it is important to recognize the breadth of research conducted on exactly which NEAs should be targeted for manned missions. The NEAs discussed in the following chapters are among those that are generally recognized as "most accessible".

A very early work investigating the possibility of manned travel to NEAs was penned by famed comet hunter Eugene Shoemaker and E.F. Helin in 1978 [99].

Shoemaker identified NEA rendezvous as an idea that had been present in the literature, but was receiving very little attention from the astrodynamics community. He investigated the few NEAs that were known at the time with a basic Lambert targeting method to determine how feasible it would be to reach these bodies, and concluded that with several launches of the Space Shuttle (under development at the time), humans could fairly easily perform a round-trip journey to an NEA.

Over three decades have elapsed since this early work, and humans have still not traveled beyond the Moon. However, much work has since been performed on identifying possible targets in the known catalogue of NEAs.

In 1987, Lau and Hulkower [60] catalogued all NEAs known at the time based on accessibility using a two-impulse rendezvous. Thousands of NEAs have since been discovered, and work has accelerated on identifying possible targets. The works by Cui et. al. [28], LeCompte et. al. [61], and Wagner and Wie [112] compile lists of destinations based on varying criteria, from overall flight time to nominal mission Δv. Other cataloguing work investigating basic targeting and categorization methods has been performed by Adamo et. al. [1], Gil-Fernandez, Cadenas, and Graziano [39], Perozzi, Rossi, and Valsecchi [81], and Zimmer and Messerschmid [118]. Specific interest has recently arisen regarding utilizing NEAs for their metals and resources; Sanchez and McInnes [96] created a catalog of NEAs that are useful for mining and are accessible with low-energy transfers. A recent conference proceeding by Landau and Strange [57] primarily investigates optimized trajectories to NEAs using electric propulsion, but also includes a description of culling the entire known NEA database to determine reasonable destination bodies.

An interesting study on destinations was given by Matloff and Wilga [66]. The authors investigate using NEAs that cross Earth's and Mars' orbits in an effort to identify NEAs that could be useful as literal shielding mechanisms on a transfer between the two planets. Several candidates are defined in their work.

The subject of asteroid discovery techniques and metrics for determining accessible asteroids is currently a rich study field. Although this dissertation does not deal directly with this topic, the material presented here benefits from previous and ongoing work in the field.

1.4.2 Previous and proposed missions

The topic of NEAs as potential robotic and/or human destinations for spaceflight has encouraged the proposal of missions to asteroids and other small bodies. Since a large portion of this dissertation addresses proposed mission design strategies to visit NEAs, it is pertinent to mention some of the literature on existing or proposed missions with similar destinations.

Two prominent NEA missions are the Hayabusa mission (Japan), which visited NEA 25143 Itokawa, and the planned OSIRIS-REx mission (USA) to the NEA 101955 Bennu (formerly 1999 RQ36). Hayabusa successfully returned a material sample from Itokawa's surface, and OSIRIS-REx is slated to perform similar tasks at its target asteroid[1].

[1]Current information on the planned OSIRIS-REx mission may be found on the mission website at `http://www.asteroidmission.org`. Last accessed 9 June 2014.

Another high-profile mission that is currently in operation is the Dawn spacecraft [89], visiting Vesta and Ceres in the main asteroid belt between Mars and Jupiter. While these bodies are not NEAs, missions such as Dawn represent a class of missions similar to those that may be flown using the algorithms and results of this dissertation. Other similar missions include the MarcoPolo-R mission to rendezvous with an NEA [6], the ASTER mission to an NEA [104], general proposed missions for NEA sample return [30], an NEA orbiter/lander mission [72], and deflection missions for currently known Potentially Hazardous Asteroids (PHAs), such as NEA 99942 Apophis [48].

A section in this dissertation addresses using Lunar flybys to enter into FRTs for the purpose of NEA rendezvous. A brief mention is made here to the work by Dunham, Farquhar, and McAdams [32], which details previous missions that utilized gravity assist maneuvers to accomplish their interplanetary objectives, such as MESSENGER (Mercury), New Horizons (Pluto), and STEREO (Solar observation).

1.4.3 Impact threat mitigation

Events within the last century have heightened humanity's collective awareness of the danger of an asteroid impacting the Earth. The giant Tunguska impact event (1908), and recent smaller events such as the Chelyabinsk meteor (2013) serve as reminders that our planet is regularly impacted by relatively large bodies. Impacts from even larger bodies pose the risk of continent-scale destruction.

Because of this, extensive work has been devoted to developing technologies related to steering PHAs out of their natural orbits, which may intersect Earth's

location at some future time. Although the vast body of literature cannot be fully referenced here, two works are given for some contextual motivation of why traveling to NEAs, and specifically PHAs, is important to our planet's safety. The concept of impact mitigation is an important driver in formulation of missions to NEAs; given that the topic of this dissertation is the development of algorithms to determine trajectories to reach NEAs, it is pertinent to mention the current work on this major application of visiting NEAs.

Schweickart [97] states the need for developing an international plan for asteroid threat mitigation. Works on policy, such as this one, must be coupled with scientific and technical publications to state the full case and solution for PHA impact mitigation. A paper by Casalino and Simeoni [20] investigates optimal trajectories to PHAs, and gives an intriguing algorithm to maximize the miss distance of a PHA deflection. Similar works exist, yet these two serve as a good impetus for developing trajectories to reach NEAs for the purposes of impact threat mitigation.

Given that PHAs are a subset of NEAs, it is important to recognize the application of the algorithms presented here to missions that travel to PHAs for the purpose of impact threat mitigation.

1.4.4 Free return trajectories

The concept of Free Return Trajectories (FRTs) is by no means novel; many previous works have detailed the usage of FRTs for a myriad of astrodynamical applications, and FRTs have been implemented on previous missions (most notably in the Apollo program). To the best knowledge of the author, the application of

FRTs to reach NEAs has not previously been posited by other authors, but there is a wealth of literature on the topic of FRTs in general. Since this specific class of trajectory is investigated in several of the following chapters, it is important to recognize previous work that has been conducted on the topic.

During the design of the Apollo trajectories to the Moon, an early work by Wagner [111] investigated the feasibility of using FRTs for manned missions to the Moon. This work lists benefits and detriments to using FRTs in general, noting that they provide an aspect of risk mitigation, but incur a slight penalty on overall mission time and fuel expenditure. This type of applied work has been followed up by many proposed methods and missions utilizing FRTs. Jesick and Ocampo [51–53] developed a generous set of papers describing, categorizing, generating, and optimizing FRTs from the Earth to the Moon, specifically focusing on conducting Lunar orbit insertion from an FRT. Peng, Shen, and Li [79] have also contributed to this topic, describing a method of generating Lunar FRTs.

Other celestial bodies have been the destination of FRTs, as well. Looking beyond the Moon, Wolf [114] applied the theory of FRTs to proposed missions to Mars, and developed a simple method for searching for different types of Earth-Mars-Earth FRTs. Miele, Wang, and Mancuso [69] outlined characteristics of FRTs, and computed solutions for Moon and Mars missions. Patel, Longuski, and Sims [78] catalogued all possible FRTs to Mars from Earth, noting specifically a set of fast trajectories with a round-trip time of about 1.4 years. Cometary missions have been studied using FRTs in a similar manner to those studied in this dissertation. Farquhar [36] gives an excellent summary of Earth-return trajectories used in the

past several decades for cometary flyby missions, including missions that conducted flybys of several comets by utilizing a variety of FRTs that returned near the vicinity of Earth. Farquhar and Dunham [35] also describe an Earth-return trajectory to fly by Halley's comet to collect dust and gas samples.

FRT research has been prolific in the theoretical realm, as well. A paper in 1969 by Hollister [47] investigated periodic orbits between planets, later known as cyclers, which belong to a certain class of FRTs. Luo, Yin, and Han [62] presented a pseudostate algorithm to calculate FRTs, and specifically apply the algorithm to Lunar FRTs. Russell and Ocampo have made significant contributions to the theoretical calculation of cyclers and FRTs. They categorize half- and full-revolution FRTs [90], and apply FRT theory to generate cyclers between Earth and Mars [91]. Additionally, they present a geometric analysis of FRTs after encountering a body in a gravitational flyby [92], and give an exhaustive algorithm using combinatorics to calculate all possible cycler trajectories between Earth and Mars using half-rev, full-rev, and generic FRTs [93]. These types of FRTs are summarized and described in Chapter 3.

The concept of half-rev, full-rev, and generic FRTs in the three-body realm is also discussed here, and the subsequent FRTs are utilized in an algorithm that develops round-trip trajectories to NEAs. In general, most previous works detailing the usage and calculation of FRTs assume that a second gravitating body effectively "turns" the trajectory (though there are exceptions). This dissertation focuses mostly on FRTs that do not require a gravitational flyby to return the spacecraft to

the Earth, though there is an investigation of using the Moon to improve the fuel usage and time required for Earth-returning FRTs in Chapter 5.

1.4.5 Human missions considerations and abort options

The application of FRTs in this dissertation, and in many previous works, is to facilitate risk reduction for manned missions to other celestial bodies. The Apollo program utilized FRTs and hybrid FRTs to provide for an abort option for the astronauts in the event of the spacecraft's inability to enter into Lunar orbit. Of specific relevance to this dissertation are works that explore human missions to NEAs and abort options for interplanetary missions that incorporate studies of FRTs. A primary intention of the work presented here is to show that, for a small penalty in Δv or time of flight, a FRT may be utilized to visit an NEA for the purposes of partially mitigating the risk of sending humans on a long voyage into interplanetary space.

The work by Drake [29] investigates the topic of sending humans beyond LEO, and discusses the feasibility of several different mission types, including missions with NEA destinations. In a qualitative sense, the author explores the challenges and benefits to sending manned missions beyond LEO, and places special emphasis on NEA missions. In studying manned missions to Mars, Landau and Longuski [58] show specifically that FRTs merit special consideration for abort options. Discussions in both works provide a persuasive rationale for visiting interplanetary destinations with manned missions, and the consideration of abort options demonstrates that FRTs may be included as a viable option for distant human missions.

Ocampo and Saudemont [74] introduce an algorithm to generate multi-impulse abort sequences to return to the Earth from the Moon, and explore the concept of "any-time abort" for Lunar missions. This work is representative of a larger class of studies that investigate abort options that require deterministic maneuvers, as opposed to FRTs, which require no additional deterministic maneuvers to proceed with a mission abort.

In the use of trajectories that escape Earth and return on a direct re-entry corridor, it is important to limit the anticipated re-entry speed to below a maximum threshold. Tauber, Palmer, and Yang [108] study Earth re-entries for spacecraft returning from Mars, and provide upper limits on re-entry speed and acceptable flight path angles. These factors must be considered when desigining FRT abort trajectories, especially if the FRT returns from outside the Earth-Moon system. Tartabini, Striepe, and Powell [107] describe abort options for manned Mars missions, and conclude that FRTs are not always a feasible option when considering re-entry speed limitations. Following the findings of these two works, the methods used in this dissertation incorporate limitations on re-entry speed and flight path angle that are comparable to limitations placed on similar missions in other studies. Actual re-entry mission data is used from Apollo 4 [45], Apollo 8 [71], Apollo 11 [8], and Hayabusa [70, 100, 117].

1.4.6 Methods to reach NEAs

Near-Earth Asteroids have been studied extensively over the past several decades; in addition to determination of appropriate destination targets and ratio-

nale for traveling to these bodies, there exists much literature on trajectory design from the Earth to these NEAs. It is important to summarize the previous work conducted in this rich field of study, because the primary findings here are results of employing various algorithmic methods to reach NEAs.

Beginning with the initial exploratory work by authors such as Shoemaker and Helin [99], many researchers have determined novel methods to reach NEAs in ways that reduce time of flight and fuel expenditure. This dissertation augments the library of methods used to reach NEAs and other solar system bodies by utilizing FRTs as mission abort segments. This method is novel in the literature, combining the two well-researched topics of NEA rendezvous and FRTs. The works listed in this section detail other methods proposed to reach NEAs and optimization strategies to ensure their optimality in a fuel, Δv, or time sense.

As mentioned previously, Shoemaker and Helin [99] initially proposed several NEAs as targets for study, and performed some basic numerical work using simple Lambert targeting to assess the reachability of these bodies. Qiao, Cui, and Cui [87] give another high-level discussion of NEA rendezvous opportunities, and give a general idea of mission time scale and Δv cost. In Ref. [86], the same authors employ hybrid optimization with genetic and sequential quadratic programming algorithms to design a mission to NEA 4660 Nereus.

Specific methods of reaching NEAs have been investigated, including general methods in low-thrust propulsion (Grigoriev and Zapletin [42], which gives methodology for optimizing long-duration low-thrust transfers; Colombo, Vasile, and Radice [26], which applies differential dynamic programming methods to low-thrust; Park

and Choi [76], which applies fast flight time and low thrust to intercept and rendezvous with Earth-crossing asteroids). Specific low-thrust methodologies have also been described, such as solar sails (Mengali and Quarta [68], which uses well-known NEA 99942 Apophis as an example), solar electric propulsion (Kluever [55], which gives a specific rendezvous example of comet Wilson-Harrington; Landau and Strange [57], which also details specific low-cost targets and database reduction), and a novel method of electric sails (Quarta and Mengali [88], which minimizes mission time to reach PHAs).

Gravity assists have also been utilized to reach NEAs. Qiao, Cui, and Cui [85] present an example of impulsive rendezvous with NEA Ivar with feasible Δv and transfer time values using Earth gravity assist. Chernov [23] presents a design of a kinetic impactor mission that maximizes the miss distance of a post-impact PHA. The author calculates optimal trajectories to these PHAs using gravity-assist schemes and electric propulsion. Chen, Baoyin, and Li [22] propose the novel idea of using spent Lunar spacecraft to visit NEAs, decreasing the amount of fuel required to reach an NEA compared to a spacecraft that departs directly from LEO. This work also uses particle swarm optimization (PSO), which is utilized in this dissertation for some applications.

Authors have also examined varying metrics for optimal missions to NEAs. In the algorithms described here, Δv optimal trajectories are sought. This cost metric is often utilized, but other options presented in the literature are fast trajectories (Conway [27], which gives good motivation for quick missions to PHAs using low-thrust), maximum deflection distance for PHA mitigation (Park, Elder, and Ross

[77], which showcases early work on deflection analysis and timing considerations in PHA deflection; also Chernov [23]), and ability to visit multiple NEAs of interest (Perozzi et. al. [80], which uses resonant flybys to visit NEAs multiple times without rendezvous).

In all, the literature presents a variety of work on how to reach NEAs, what metrics to use for optimality, how to calculate the trajectories, and exactly which NEAs should be visited. This dissertation selects some of the more accessible bodies found in previous studies, and utilizes impulsive rendezvous to reach NEAs with FRTs. Extensions on this work could be made into the low-thrust realm, which is well-researched in the field of NEA intercept and rendezvous.

1.4.7 Optimization routines and their usage

Optimization routines included in this dissertation are of two different types: sequential quadratic programming (SQP) and particle swarm optimization (PSO). SQP is a more traditional method that utilizes gradients of constraints and the cost function with respect to parameters to obtain a feasible solution that minimizes a certain performance index. The third-party packages VF13 [4] and SNOPT [40] are both used to produce the results found in the following chapters. VF13 is publicly available at no charge from the Harwell Subroutine Library archive[2], and includes a simpler interface for constrained and unconstrained optimization problems. SNOPT is a robust, complex, and adaptable software package that includes a host of internal methods to solve difficult or large-scale optimization or feasibility problems. SQP

[2]Accessible at http://www.hsl.rl.ac.uk/. Last accessed 20 March 2014.

methods are ideal for reliably driving equality constraints to their desired values. A detriment of these methods is that gradients of the constraints and cost function with respect to the parameters must always be supplied or computed internally. Gradients may often be very complicated to compute by hand, or it may require a large amount of computation time to numerically estimate them.

In contrast, the PSO method does not require gradients or even an accurate initial guess, but does not reliably present accurate convergence characteristics and does not deal well with inequality constraints. This optimization method belongs to a larger class of heuristic optimization algorithms, which includes other methods such as genetic optimization and simulated annealing. The PSO method was introduced by Kennedy and Eberhart in 1995 [54] as a numerical method to simulate a flock of birds attempting to find food in a cornfield. Each "particle" is aware of its own best location visited, as well as the entire flock's best location. The movement of each particle through the search space depends on relative weighting between these parameters, and does not depend on gradients. PSO was adapted early on in the literature, e.g. by Venter and Sobieszczazanski-Sobieski [110], who proposed a method for introducing constraints to the method, which otherwise is rather incapable of incorporating constraints. PSO has also been applied to spacecraft trajectories. Pontani and Conway [83] explored tuning the weights and constants in the algorithm specifically for problems on the scale of spacecraft trajectories and finding FRTs. Pontani, Ghosh, and Conway [84] applied PSO to other space trajectories, and showed convergence properties for more complex problems. Ghosh and Conway [38] show more performance statistics for the algorithm in spacecraft trajectories.

For SQP algorithms that do require gradients, there are many methods that are in use in the literature to calculate the gradients. In this work, two methods are used: analytical gradients with the first-order state transition matrix (STM) approximation, and complex-step numerical differentiation. Analytical gradients are highly accurate for most applications, but there is a large amount of up-front manual work required to implement the gradients correctly. Ocampo and Munoz [74] provide the STM variational equations to compute expressions for the analytical gradients. This method is used here wherever analytical gradients are implemented, and is described in more detail in a later section. The concept of finite-step numerical gradients is well-known, but using complex steps is a relatively new concept introduced by Martins, Sturdza, and Alonso [65]. Parameters are perturbed by a small complex term to compute the sensitivity of constraints and cost functions with respect to the parameters. This method is implemented to accurately compute gradients where expressions for analytical gradients may be very difficult to obtain. In fact, the method is shown to achieve accuracy similar to analytical gradients for the same evaluation cost as obtaining traditional forward difference gradients. Computational speed may still be affected as a result of a significant increase in number of function evaluations compared to analytical gradient evaluation.

1.4.8 Trajectory design and continuation methods

The final technical chapter of this dissertation focuses on a method to transition space trajectories from simplistic two-body models to more realistic n-body models with actual ephemerides. This methodology is quite useful for developing

robust initial guesses for optimization algorithms, or for constructing planetary or moon tours in an accurate dynamical system. Much of the literature on tour design incorporates only simplistic models, and the challenging step of transitioning to higher fidelity models is often overlooked. Many authors have addressed ballistic patched conics tour design [19, 34, 43, 50, 101, 103], but few have presented systematic algorithms for representing the results in n-body ephemeris models. The transition to a full ephemeris model is often made in one step, and frequently will not converge. Ultimately, a mission must use a fully-integrated trajectory, which accounts for the full ephemeris and full gravitational model (e.g. [67, 115]).

Previous methods have been introduced to address this model fidelity transition problem. These methods include: 1) the application of a "multi-conic method" with differential correction [16, 113] that approximates trajectory legs by considering separate perturbing influences; 2) a multi-step correction process [63] that divides trajectories into nodes and performs differential correction on the node states; 3) a method to differentially correct the hyperbolic excess velocity to meet certain conditions [15] (the "patched-integrated" method); and 4) using a three-body solution directly as a guess for a full ephemeris solution in a multi-body dynamical system [41].

Continuation methods (also known as homotopy methods) have been applied to spacecraft trajectories elsewhere in the literature to move between dynamical models. One example is the problem of finding finite-thrust trajectories from solutions using impulsive maneuver models [17, 82]. Several works incorporate continuation methods to transfer between ephemeris models, moving from low-fidelity three-body

to four-body ephemerides [59], transitioning between ideal patched conics to full ephemeris patched conics [95], and calculating n-body patched conics trajectories from a basic circular coplanar model [94]. Another application of continuation methods is to determine orbit families and solution bifurcations. Continuation methodology has been applied to computing families of orbits about Earth-Moon L_1 [9, 75], finding periodic orbits and optimal spacecraft placements in the Earth-Moon system [24], computing Earth-Moon transfer families and cycler trajectories [21, 116], determining families of optimal multi-burn general orbit transfers [25], and calculating launch vehicle thrust profiles [64].

The work in Chapter 6 of this dissertation presents a novel method of transitioning space trajectories from low to high fidelity dynamics, and expands on the ideas presented in the literature. It is important to note that one method may function better than another for obtaining a fully integrated trajectory, depending on the specific situation; the goal of developing the algorithm presented in this dissertation is to provide a robust method of representing multi-body flyby sequences in realistic dynamics. The motivation for this work developed out of the Lunar flyby algorithms presented in Chapter 5, and some mention of the application of the continuation method to an FRT problem is made in Chapter 6.

Chapter 2

Dynamical Background

Various portions of this dissertation investigate spacecraft and celestial body motion in different coordinate systems and dynamical frameworks. The most simple of all non-trivial celestial mechanics dynamical systems is the point-mass two-body problem, where a secondary body (e.g. the spacecraft) is assumed to be massless and undergoes conic motion about a primary body, which is assumed to act as a point-mass (i.e. no non-uniform mass distribution). In many cases, it is appropriate to study the gravitational effect of another (third) body, or many other bodies, often under certain assumptions. When investigating the resultant motion on a spacecraft that is under the influence of two or more gravitational bodies, there does not exist a known general analytical solution to the spacecraft state as a function of time. A common approximation to the three-body problem (the spacecraft and two gravitating bodies) is the Circular Restricted Three-Body Problem (CRTBP), where the bodies are assumed to be in coplanar circular motion about their common center of mass. In such a case, there exists only one known constant of motion, the Jacobi constant.

Appropriate applications of the three-body problem and CRTBP include investigating spacecraft motion near the Earth and Moon where both bodies are as-

sumed to exert an appreciable influence on the spacecraft, but other bodies (such as the Sun) are assumed to have no effect. Another appropriate regime for these dynamical assumptions is interplanetary space near the Earth, where the Earth and Moon may be assumed to comprise one mass, and the Sun is considered as the third perturbing body.

To increase model fidelity, an arbitrary number of bodies n may be included in the gravitational dynamics. A basic model that incorporates n bodies is one in which all bodies are assumed to follow their own Keplerian orbits about a central body, and the spacecraft is influenced by each orbiting body in addition to the central body. A high fidelity dynamical system includes all bodies that exert any appreciable gravitational effect on the spacecraft, and utilizes their real positions (ephemerides) instead of assuming individual Keplerian motion[1].

Each of these dynamical systems is used at some point in this work, and each is developed in some amount of detail in the following sections. Mission design often begins with basic two- or three- body models, in large part because analytical solutions for spacecraft motion exist in the two-body problem and the dynamics of three-body motion is simplified sufficiently so that optimization and integration algorithms generally do not have numerical trouble with spacecraft trajectories. Simplified dynamical systems are often very close approximations to actual n-body motion,

[1]In reality, the most accurate dynamical system includes not only all point-mass gravitating bodies, but their mass distribution as well, along with non-gravitational forces such as drag and solar radiation pressure. All bodies in this work are assumed to be spherical and of constant density, so that their gravitational influence on the spacecraft is identical to that of a point-mass. Non-gravitational forces are assumed to be zero.

and the assumption to ignore other perturbing bodies or actual ephemeris motion is often justified. However, in many dynamical systems (e.g. Jovian moon tours or distant Earth orbits), trajectories calculated in simplified systems do not acceptably approximate the real dynamics of an n-body trajectory. In such a case, a more complete dynamical system must be utilized for a more accurate representation of the true spacecraft trajectory.

2.1 Two-body dynamics

Two-body celestial dynamics have been studied extensively for centuries, and derivations and background do not need to be repeated here. It is assumed that the reader is familiar with two-body dynamics and Keplerian motion.

Two-body motion in this work represents a body (e.g. a spacecraft), assumed to be massless, that is under the influence of a spherical mass of constant mass distribution (gravitationally equivalent to a point-mass). Denoting the position of the massless body with respect to the gravitating body as $\mathbf{r}$, its second time derivative (acceleration) as $\ddot{\mathbf{r}}$, and its magnitude as r, then the equation of motion under the influence of a gravitating mass m with mass parameter $\mu \equiv Gm$ is given by Eq. (2.1).

$$\ddot{\mathbf{r}} = -\frac{\mu}{r^3}\mathbf{r} \tag{2.1}$$

The equations of motion for the two-body problem admit a closed-form solution, where the spacecraft state may be determined analytically as a function of time. To assume that the spacecraft operates according to the two-body problem is

often a good dynamical assumption. Even when the assumption is not very accurate, it is often still beneficial to perform initial analysis in the two-body framework as an initial guess to extend the model to higher fidelity.

2.2 Circular Restricted Three-Body Problem

Often, a second gravitating body (a "third body") is added to the dynamical framework. When making the assumption that the two gravitating bodies travel in circular orbits about their common center of mass (a good assumption for systems such as the Earth-Moon and Jupiter-Sun, for instance), the problem is referred to as the Circular Restricted Three-Body Problem (CRTBP). In the case of the Earth-Sun system, it is sometimes practical to include the Moon's mass with the Earth's, in which case the three-body system is formed by the spacecraft, the Sun, and the Earth-Moon combined mass.

The CRTBP, described in detail by Szebehely [105], admits just a single constant of motion, and the resulting spacecraft state does not have a known general analytical solution as a function of time. The equations of motion are described by Eq. (2.2). These equations are valid for a rotating reference frame centered at the system's center of mass, with the $\hat{x}$ direction pointing from the primary body to the secondary body. The subscripts $s1$ and $s2$ denote the position vector from the primary and secondary bodies to the spacecraft. The vector $\boldsymbol{\omega}$ refers to the relative rotation rate between the rotating and the inertial reference frames, which is constant due to the assumption of the bodies being in circular orbits about their

common center of mass. The position vector $\mathbf{r}$ is with respect to the common center of mass.

$$\ddot{\mathbf{r}} = -\frac{\mu_1}{r_{s1}^3}\mathbf{r}_{s1} - \frac{\mu_2}{r_{s2}^3}\mathbf{r}_{s2} - 2\boldsymbol{\omega} \times \dot{\mathbf{r}} - \boldsymbol{\omega} \times \boldsymbol{\omega} \times \mathbf{r} \tag{2.2}$$

The equation for $\boldsymbol{\omega}$ is given by Eq. (2.3), where $\hat{\mathbf{k}}$ is the unit vector normal to the common orbital plane of the two gravitating bodies, and a is the distance from the primary to the secondary gravitating body.

$$\boldsymbol{\omega} = \sqrt{\frac{\mu_1 + \mu_2}{a^3}}\,\hat{\mathbf{k}} \tag{2.3}$$

In the CRTBP, the equations of motion must be numerically integrated to find a time history of the spacecraft state. However, it is still a very useful dynamical framework in which to operate. The single known integral of motion, the Jacobi Constant, is useful in determining regions of inaccessibility and categorizing orbital families using an energy-like quantity. This constant often makes the CRTBP framework more informative to operate in than a full ephemeris model. Additionally, the CRTBP includes the complexity of the presence of an additional gravitating body, so the analysis may be more accurate than analysis using the two-body problem. For example, a spacecraft operating in the geostationary Earth orbit region experiences appreciable effects from the Moon's gravity, and a two-body Earth-centered gravitational model is often insufficient for more in-depth orbital analysis.

2.3 Full n-body dynamics

A high fidelity representation of a dynamical system is one that uses actual states of the gravitating bodies, incorporates their actual masses, and assumes that they are of actual size (for purposes of close approaches and flybys). An even more accurate dynamical system would include not only all possible gravitating bodies, but also the acceleration due to all bodies' non-spherical potential fields, and non-gravitational accelerations. For purposes of this work, all bodies are assumed to be spherical and of constant density. This assumption is usually valid; for example, the acceleration along an Earth-to-Venus trajectory is quite unaffected by the J_2 oblateness term of the Earth. An exception to the accuracy of this assumption would be in a case such as spacecraft orbiting about Jupiter while performing flybys of the four Galilean satellites. In such a case, the large J_2 term from Jupiter may play some appreciable role in the acceleration of the spacecraft. However, it is still a secondary consideration behind the point-mass gravitating effects of Jupiter and the Galilean satellites, and the assumption of a spherical Jupiter is still made for the results obtained in this dissertation.

To obtain the equations of motion of a spacecraft with respect to a central body while considering the perturbing effects of other "third" bodies, it is useful to consider the framework shown in Figure 2.1. If the position vector $\mathbf{r}$ is defined with respect to the central body with gravitational parameter μ, then the equations of motion of the spacecraft are given by Eq. (2.4).

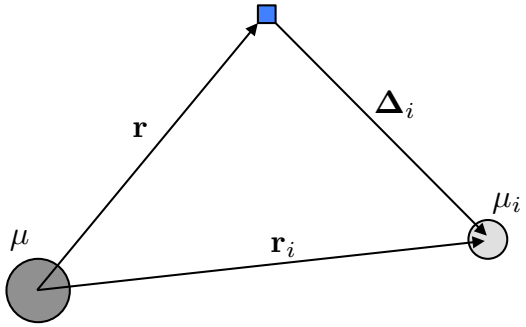

Figure 2.1: Geometry of the n-body problem

$$\ddot{\mathbf{r}} = -\frac{\mu}{r^3}\mathbf{r} + \sum_{i=1}^{n} \mu_i \left[\frac{\boldsymbol{\Delta}_i}{\Delta_i^3} - \frac{\mathbf{r}_i}{r_i^3} \right] \tag{2.4}$$

The equations of motion for the n-body problem do not admit a known closed-form solution in general, and must be numerically integrated to obtain a solution of the state over time.

2.4 Usage of each dynamical system

It is most common to begin analysis of space trajectories in the simple two-body problem. Since a closed-form solution exists in this framework, it is often easier and quicker to determine viable trajectories using this dynamical model, and to use these solutions as initial guesses for higher fidelity dynamical systems. In this dissertation, the two-body problem is used in a variety of fashions. First, the concept of Free Return Trajectories is discussed initially in a two-body Sun-centered framework, which allows fast and methodical calculation of heliocentric trajectories. Secondly, the two-body problem is used for initial guesses in some analyses involving

the CRTBP. This includes parts of algorithms that involve Lambert's problem for initial trajectory construction, since Lambert's problem is defined only in a two-body framework. Finally, Chapter 6 begins in a patched-conics framework, which essentially assumes multiple two-body problems with trajectories that are "patched" together. This two-body patched-conics model is eventually formally continued to the full n-body dynamics.

The CRTBP is utilized when a more accurate representation of a system is desired, especially when the system is primarily dominated by two massive bodies. The Earth-Moon and Earth-Sun systems are two examples of cases when the CRTBP provides a fairly accurate representation of actual dynamics. For example, the Lagrange equilibrium points theoretically exist at stationary locations only in the CRTBP, but spacecraft placed at or near these points in reality experience accelerations very similar to the motion predicted by the CRTBP. This dynamical framework is used to find families of FRTs that emanate from and return to the Earth, and to find FRTs suitable for travel to NEAs. In both of the corresponding chapters, the Earth and the Moon are assumed to be one combined body.

The n-body problem, as mentioned, is a highly accurate point-mass dynamical model, assuming that all bodies that have some appreciable influence on the spacecraft are included in the analysis. In this dissertation, the n-body problem is used to find FRTs that fly by the Moon for NEA rendezvous, and the Sun, Earth, and Moon are all included as separate bodies. While there does exist a restricted four-body problem in the literature, the n-body dynamics with actual ephemerides are used here. In Chapter 6, the n-body dynamics are the final result of the formal con-

Table 2.1: Constants and parameters

Symbol	Description	Value	Units
μ_s	Grav. param. of the Sun [102]	$1.32712440018 \times 10^{11}$	km^3/s^2
μ_e	Grav. param. of the Earth [98, 109]	3.986004415×10^5	km^3/s^2
μ_m	Grav. param. of the Moon [98, 109]	4.902799×10^3	km^3/s^2
μ_J	Grav. param. of Jupiter [56]	1.26686511×10^8	km^3/s^2
r_{es}	Sun-Earth distance (CRTBP) [98, 109]	1.49597870×10^8	km

tinuation of trajectories from the two-body patched-conics framework. Trajectories represented in this model take gravitational forces from any number of bodies into account, and may be considered as fully-integrated trajectories upon convergence.

2.5 Constants and parameter values

Relevant numerical quantities and constants are listed in Table 2.1, and are used throughout the dissertation. The values given here vary slightly in the literature, but reliable values may be found in the references noted in the Table.

Where numerical integration is performed, a variable step Runge-Kutta (RK) integrator is used. In Chapters 3-5, an RK45 integrator is used [46], and in Chapter 6, an in-house RK78 integrator is used. All calculations are performed on a MacBook Pro (2010) running Mac OS 10.6-10.9 (regularly updated) with a 2.53 GHz Intel Core i5 processor and 4 GB of RAM. The code was written primarily in Fortran 90, compiled with the GNU open-source compiler gfortran[2], and figures were generated with Matlab[3].

[2] `https://gcc.gnu.org/wiki/GFortran`. Last accessed 11 August 2014.
[3] `http://www.mathworks.com/products/matlab/`. Last accessed 11 August 2014.

Chapter 3

Earth-Centered Free Return Trajectories

3.1 Chapter introduction

In both the two-body and Circular Restricted Three-Body models containing the Earth and the Sun, there exist a variety of families of trajectories that depart from and return to the Earth without any intermediate deterministic velocity maneuvers. In a three-body sense, with a non-point mass Earth, these trajectories obtain sufficient instantaneous energy with respect to the Earth to escape Earth's immediate sphere of influence, and return near their starting points about the Earth. In the two-body model, trajectories may easily be found that represent half-year, full-year, resonant, and n-year Free Return Trajectories (FRTs), where n is not an integer or half-integer. The trajectories found in a two-body sense may be compared to those found in a restricted three-body model, which are found by considering both the gravity of the Earth and the Sun. This chapter presents a description and categorization of Earth-centered FRTs in both a two-body and three-body sense.

These types of FRTs have many applications that are of interest in modern astrodynamics. In the Earth-Moon rotating frame, these types of orbits were utilized in the Apollo program to circumnavigate the moon on a trajectory that returned the spacecraft to an atmospheric re-entry corridor as a risk mitigation scheme [71]. They

continue to be researched today for future lunar landing missions with similar risk mitigation benefits [51, 53, 79]. Other modern uses for free-return orbits in various forms include missions to near-Earth asteroids and cyclers between multiple solar system bodies for cargo ferrying or crew exploration [58, 69, 78, 92, 93, 107].

A classification system is presented in this chapter that categorizes FRTs in the Earth-Sun rotating frame that begin and end near the Earth (or at the Earth, in the two-body Heliocentric model) with no intermediate velocity adjustments, while achieving two-body escape energy with respect to the Earth. The majority of the work in this chapter was presented at the 2013 AAS/AIAA Space Flight Mechanics Meeting in Lihue, HI [13].

3.2 Two-body Free Returns

Consider first a two-body model, in which the Earth is considered to be a massless point orbiting a massive Sun. Let us further simplify the assumptions by stating that the Earth is in a circular orbit around the Sun. In this ideal scenario, simple trajectories may be calculated that depart from the Earth and return to it after orbiting the Sun. There exist half-revolution, single-revolution, resonant, and n-revolution free-return trajectories, where n may be any real number greater than one. The concept of two-body FRTs is not novel; many authors have investigated the topics discussed in this section [47, 78, 90–93, 114]. These FRTs deserve some discussion, however, and are included here to show FRTs in their most basic form.

3.2.1 Half-revolution FRTs

First, consider the half-revolution FRTs. These trajectories return to Earth after exactly half a year, so in the ideal model, they return to the Earth exactly on the opposite side of the Sun from which they depart. The trivial solution to this problem (and to any simplistic FRT) is the trajectory of the Earth itself. However, an infinite number of other trajectories also exist. The time of flight is constrained to be exactly half a year (exactly the same as the time that it takes the Earth to reach the return point). This flight time constrains the semimajor axis to be the same as that of the Earth. However, the plane of the orbit is unconstrained, and represents a single degree of freedom by which we may obtain an infinite number of trajectories.

Figure 3.1(a) depicts a number of these half-revolution FRTs in a Heliocentric inertial frame. All trajectories begin at the Earth and end at the Earth a half year after they depart, but the plane of the orbits varies between trajectories. In this manner, the locus of these trajectories represents a sphere with radius equal to Earth's orbital radius and the Sun at its center. Figure 3.1(b) shows these trajectories in an Earth-centered rotating frame, which is a common depiction of FRTs. This representation will be used later in the three-body problem, and it is useful to compare the results from the two- and three-body solutions in the same frame.

3.2.2 Single-revolution FRTs

Next, consider FRTs that return to Earth exactly one year after they depart. If the return point is a single 2π revolution from the start point, the two points are identical in inertial space. Therefore, FRTs in this family make a single revolution

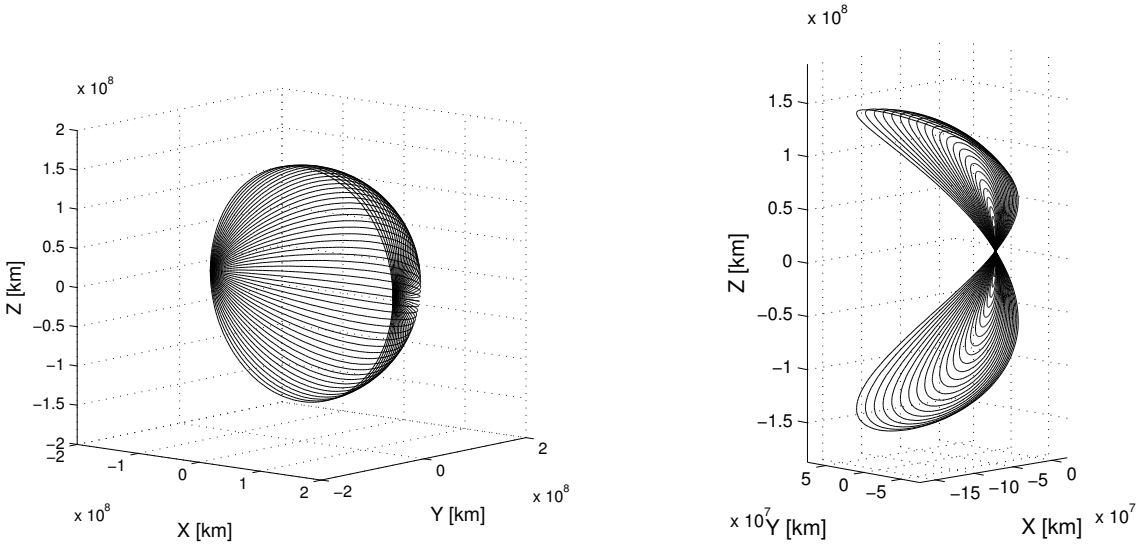

(a) Sun-centered inertial frame

(b) Earth-centered rotating frame

Figure 3.1: Half-revolution transfers

about the Sun, and have a period of exactly one year. The period constrains the semimajor axis to be equal to that of the Earth. Constraining the semimajor axis constrains the magnitude of the departure (and arrival) velocity in a two-body sense, as shown in Eq. (3.1), where a is the semimajor axis, E is the two-body energy, and v is the spacecraft speed.

$$\begin{aligned} a_{sc} &= a_{earth} \\ E_{sc} &= \frac{v_{sc}^2}{2} - \frac{\mu_{sun}}{r_{earth}} = -\frac{\mu_{sun}}{2a_{sc}} \\ E_{earth} &= \frac{v_{earth}^2}{2} - \frac{\mu_{sun}}{r_{earth}} = -\frac{\mu_{sun}}{2a_{earth}} \\ \Rightarrow E_{sc} &= E_{earth} \Rightarrow v_{sc} = v_{earth} \end{aligned} \tag{3.1}$$

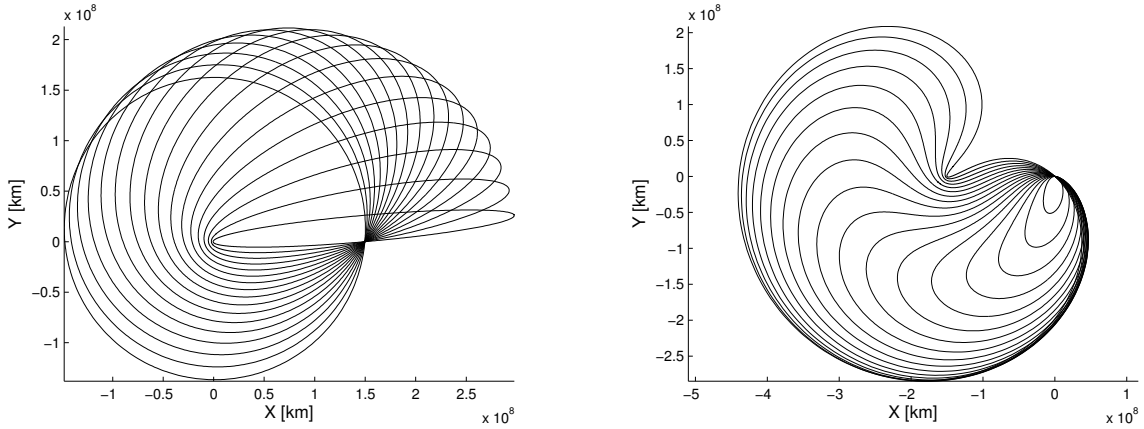

(a) Sun-centered inertial frame (b) Earth-centered rotating frame

Figure 3.2: Single-revolution planar transfers

Even though the scalar velocity magnitude is constrained, the direction of the departure velocity vector is free, and there are therefore two degrees of freedom in the 3D single-revolution FRT problem. If the single-revolution FRTs are constrained to the orbital plane of the Earth, only one degree of freedom exists. Figure 3.2(a) shows this family of planar FRTs in a Heliocentric inertial frame. Figure 3.2(b) depicts the same trajectories in an Earth-centered rotating frame.

The planar constraint may be relaxed, and any initial inclination for the single-revolution FRTs may be selected. Figure 3.3(a) shows the FRTs with a Heliocentric inclination angle of ± 20 degrees, and Figure 3.3(b) shows the same trajectories in an Earth-centered rotating frame.

Near the limiting case of a polar Heliocentric orbit, the FRTs approach the above-plane and below-plane half-revolution FRTs. Figure 3.4(a) depicts the single-

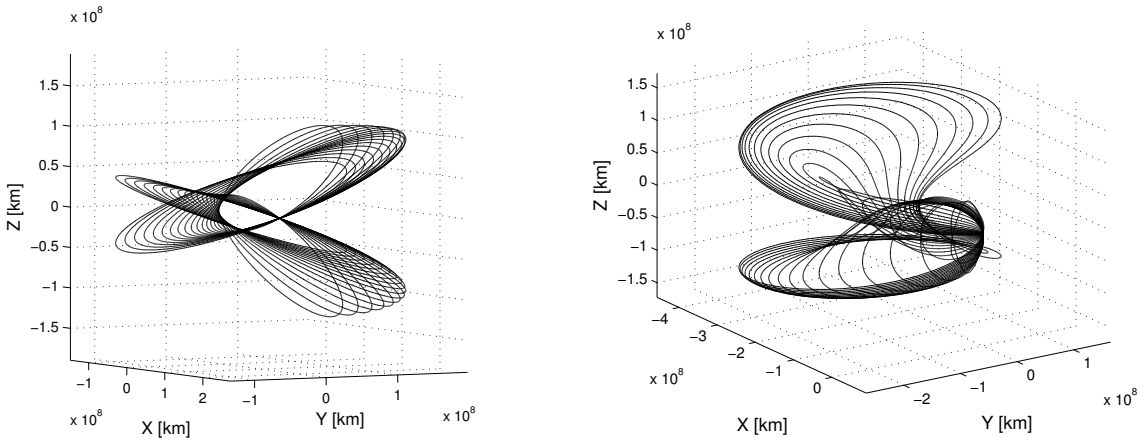

(a) Sun-centered inertial frame

(b) Earth-centered rotating frame

Figure 3.3: Single-revolution transfers, ±20 degree inclination

revolution FRT family for an inclination of ±80 degrees, and Figure 3.4(b) shows the same trajectories in an Earth-centered rotating frame.

3.2.3 Resonant FRTs

FRTs may also be resonant, where the spacecraft and the Earth both complete a different integer number of revolutions and meet again at the inertial departure point. These trajectories are a generalization of the single-revolution FRTs, which may be described as 1:1 (one-to-one) resonant transfers.

In general, a resonant FRT may be n:m (n-to-m), where n is the integer number of revolutions that the spacecraft makes about the Sun, and m is the integer number of revolutions that the Earth makes about the Sun. For example, a 2:1 resonance would involve the spacecraft completing two revolutions about the Sun in

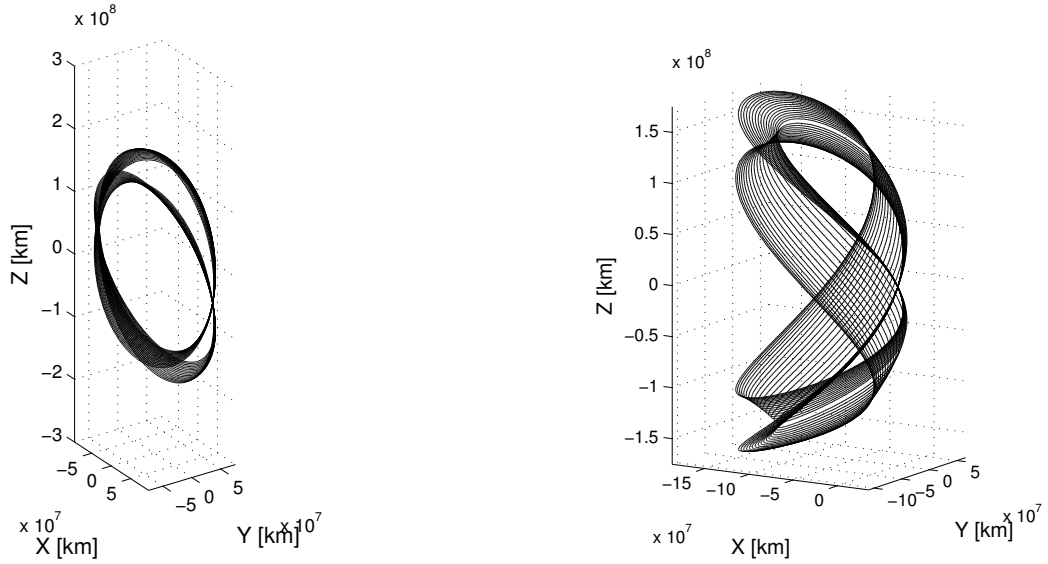

(a) Sun-centered inertial frame

(b) Earth-centered rotating frame

Figure 3.4: Single-revolution transfers, ±80 degree inclination

a single Earth year. It is therefore apparent that the spacecraft's orbital period must be half that of the Earth's, in this case.

For a general n:m resonant FRT, the period of the spacecraft is given by Eq. (3.2).

$$T_s = \left(\frac{m}{n}\right) T_{earth} \tag{3.2}$$

In our two-body simplistic model, the period of the spacecraft may be used to find its heliocentric speed at Earth departure. In Eq. (3.3), a is the semimajor axis, E is the two-body orbital energy, and v is the heliocentric speed.

$$
\begin{aligned}
a_{sc} &= a_{earth}\left(\frac{m}{n}\right)^{2/3} \\
E_{sc} &= -\frac{\mu_{sun}}{2a_{sc}} = \frac{v_{sc}^2}{2} - \frac{\mu_{sun}}{r_{earth}} \\
&\Rightarrow \frac{v_{sc}^2}{2} - \frac{\mu_{sun}}{r_{earth}} = -\frac{\mu_{sun}}{2a_{earth}\left(\frac{m}{n}\right)^{2/3}} \\
&\Rightarrow v_{sc} = \sqrt{\frac{\mu_{sun}\left(2 - \left(\frac{n}{m}\right)^{2/3}\right)}{a_{earth}}}
\end{aligned} \tag{3.3}
$$

For the specific single-revolution 1:1 resonance case, it can be seen from Eq. (3.3) that the spacecraft will have the same heliocentric speed as Earth upon Earth departure. Many varieties of general n:m resonant FRTs may be constructed; for purposes of illustration, two values each of n and m are chosen, and both a planar case and out-of-plane case are presented. Figure 3.5 gives a 2:1 resonant case, constrained to the ecliptic plane. Figure 3.5 is a 2:1 resonant case with a +40 degree heliocentric inclination. Figure 3.7 gives a 3:2 resonant case, constrained to the ecliptic plane. Figure 3.7 is a 3:2 resonant case with a +40 degree heliocentric inclination. Many more resonant trajectories exist, both in terms of n and m combinations and within the resonant families shown in these figures.

3.2.4 n-revolution FRTs

Finally, free returns may be considered that return to Earth at an inertial heliocentric position different from the departure point. A multi-revolution Lambert problem solver may be employed (see Section 4.2.1) to determine trajectory solutions between Earth at its heliocentric departure and arrival states. Because these

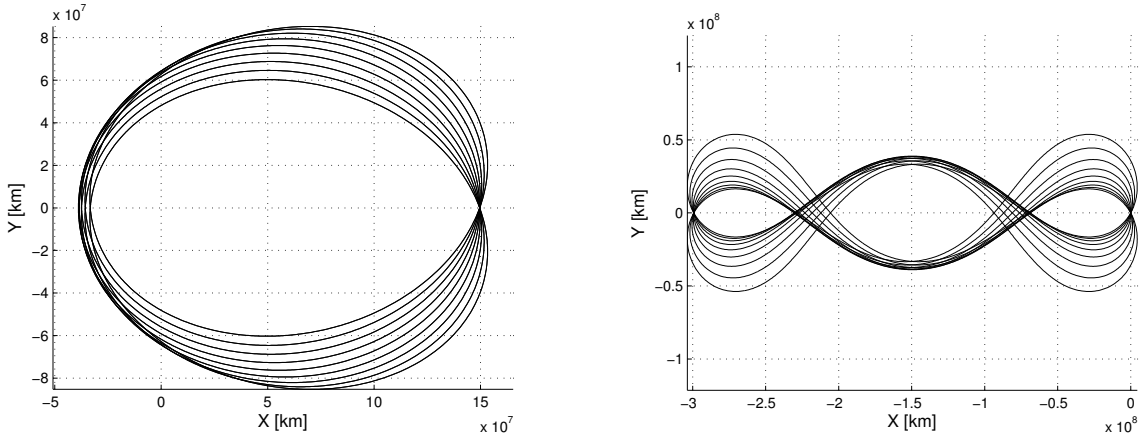

(a) Sun-centered inertial frame (b) Earth-centered rotating frame

Figure 3.5: 2:1 resonant planar transfers

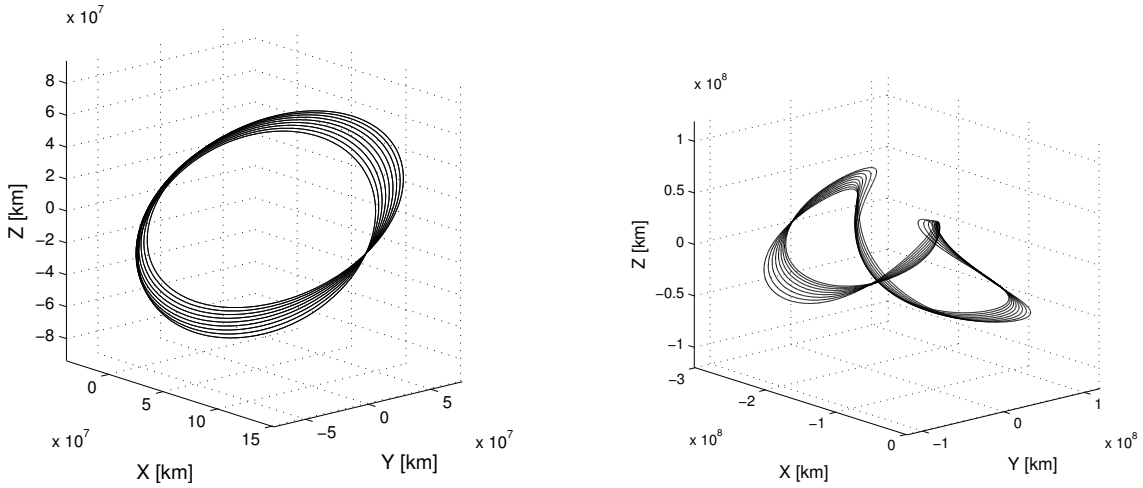

(a) Sun-centered inertial frame (b) Earth-centered rotating frame

Figure 3.6: 2:1 resonant transfers, +40 degree inclination

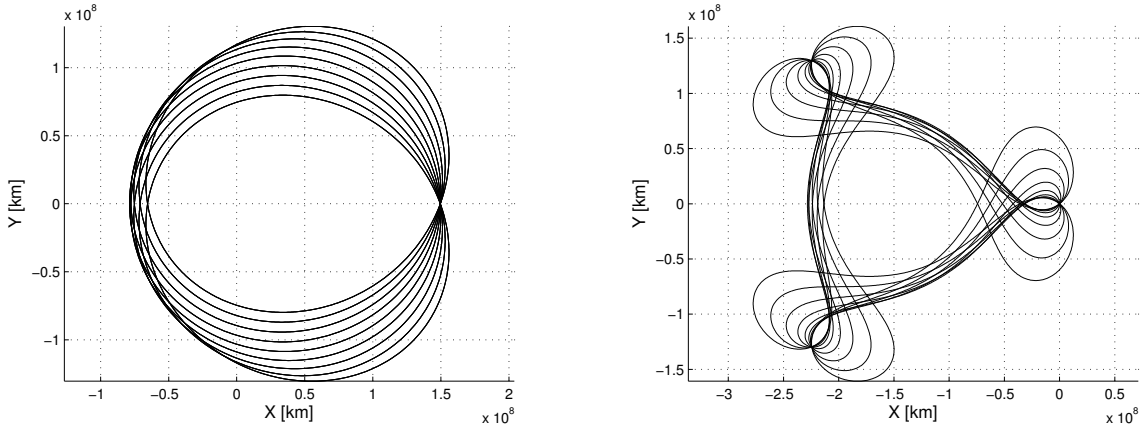

(a) Sun-centered inertial frame (b) Earth-centered rotating frame

Figure 3.7: 3:2 resonant planar transfers

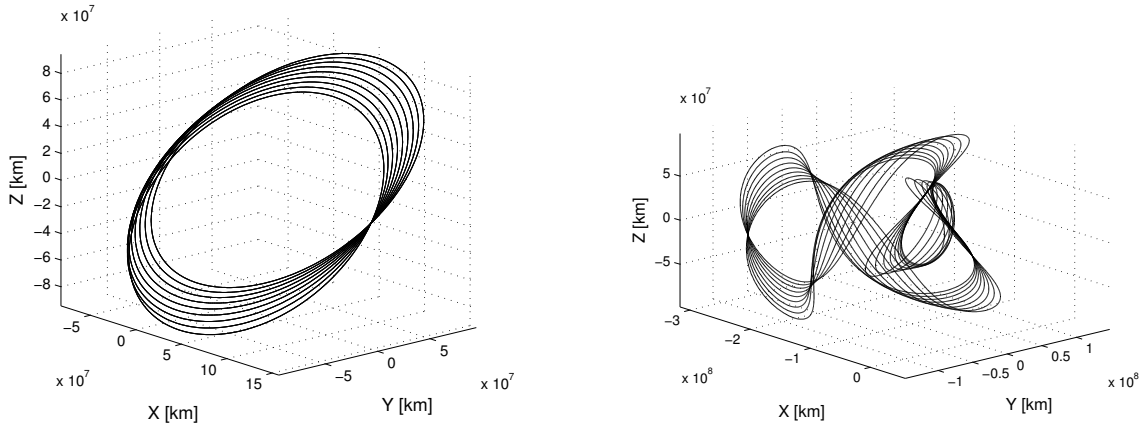

(a) Sun-centered inertial frame (b) Earth-centered rotating frame

Figure 3.8: 3:2 resonant transfers, +40 degree inclination

trajectories must intersect Earth's orbit at two points and must also include the Sun as a focus, the orbital plane is constrained to be the same as Earth's orbital plane, and out-of-plane solutions do not exist for transfers that are not a multiple of $\pi/2$.

For a multi-revolution Lambert problem with a specified time of flight, multiple solutions exist, and the direction of travel, number of revolutions, and a choice of short/long period must be specified. Figure 3.9 shows a variety of n-revolution Lambert-targeted trajectories in a Heliocentric inertial frame, varying the flight time from 380 to 500 days with a short period orbit (the long period orbit corresponds to Earth's orbit in this case). Figure 3.10 shows the same trajectories in an Earth-centered rotating frame. Figures 3.11 and 3.12 show long-period orbits, varying flight time from 520 to 700 days (the short period orbit corresponds to Earth's orbit in this case). Figures 3.13 and 3.14 show trajectories with both short- and long-way solutions that make two complete revolutions about the Sun.

3.2.5 Achievable two-body Free Returns

The previous subsections detail types of possible two-body FRTs. In reality, many FRTs are not achievable because of physical constraints. For example, an FRT may exist where the spacecraft is in a planar retrograde orbit about the Sun, but because of the very large v_∞ required to leave Earth in this case, it is not physically realizable.

By limiting the v_∞ value at Earth departure to be within certain bounds, we may obtain a set of more physically realistic two-body FRTs. To be consistent with future sections in this chapter, the two-body equivalent of Earth periapsis speed at

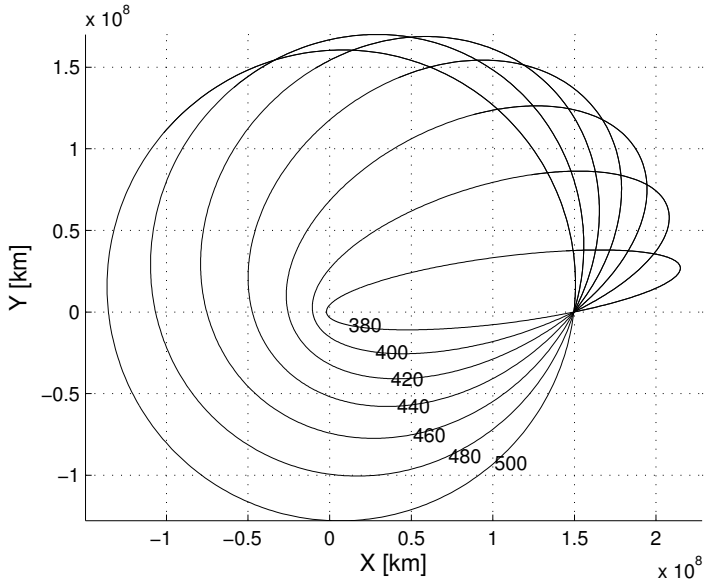

Figure 3.9: Multi-revolution transfers, 380 to 500 days, Sun-centered inertial frame

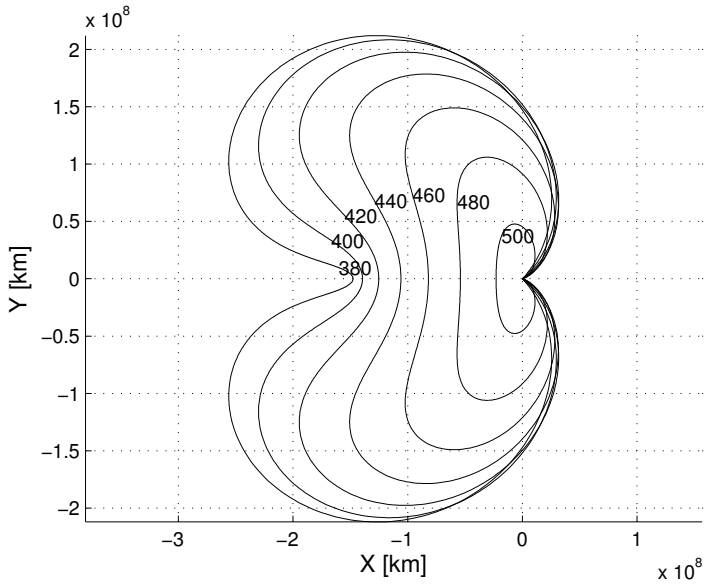

Figure 3.10: Multi-revolution transfers, 380 to 500 days, Earth-centered rotating frame

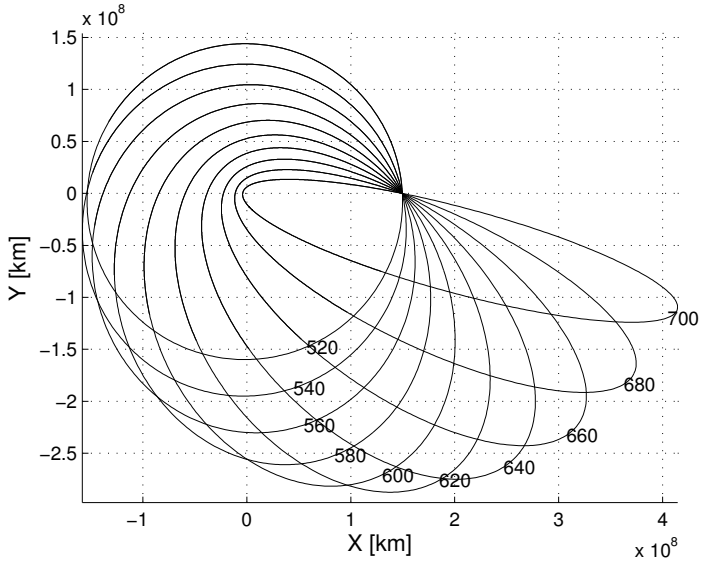

Figure 3.11: Transfers with over one full rotation, 520 to 700 days, Sun-centered inertial frame

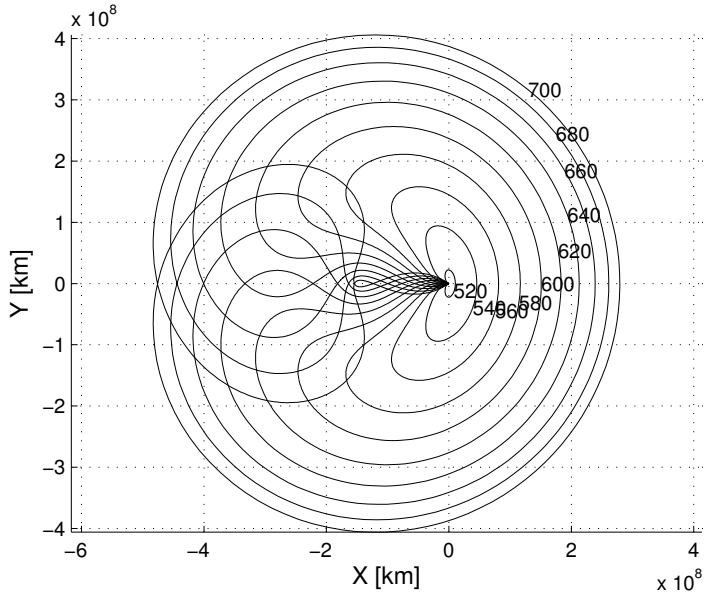

Figure 3.12: Transfers with over one full rotation, 520 to 700 days, Earth-centered rotating frame

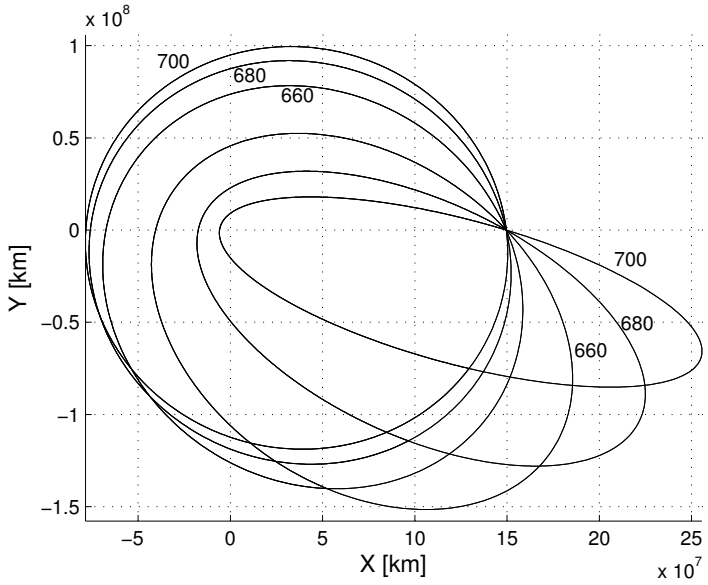

Figure 3.13: Transfers with over two full rotations, 660 to 700 days, Sun-centered inertial frame

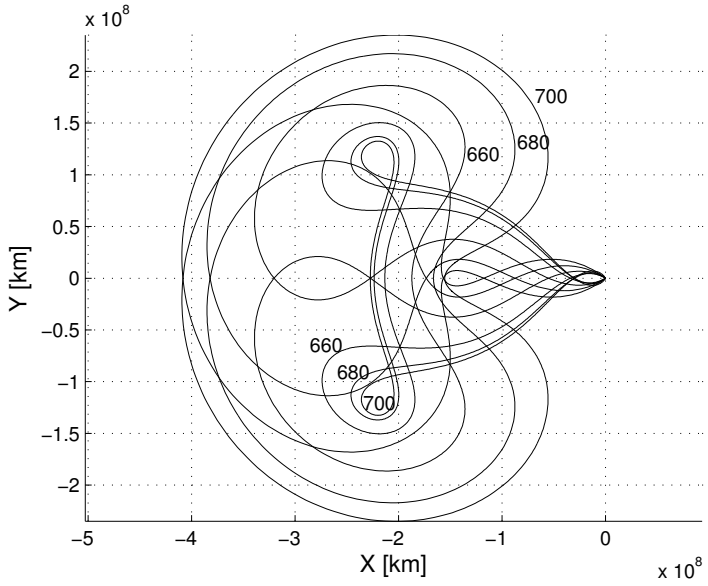

Figure 3.14: Transfers with over two full rotations, 660 to 700 days, Earth-centered rotating frame

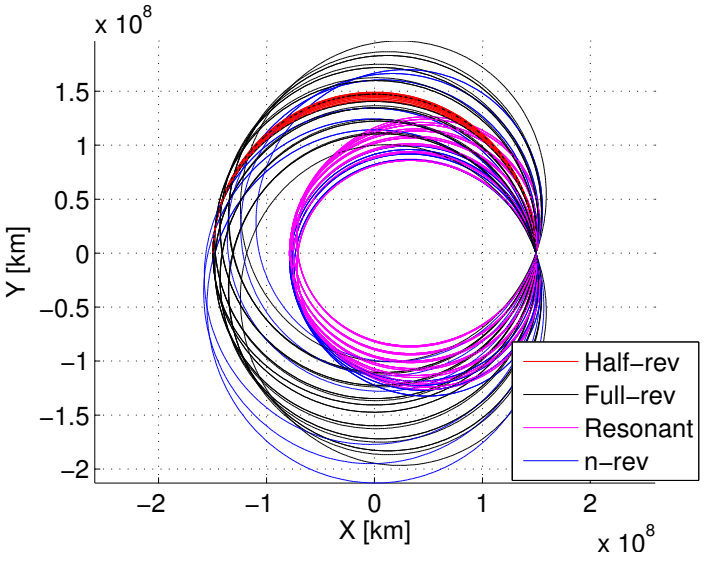

Figure 3.15: Types of feasible two-body FRTs, Sun-centered inertial frame

400 km altitude is limited to be between 11.0 and 15.0 km/s, which corresponds to a v_∞ range of 1.840 to 10.363 km/s. If this filter is applied to the types of FRTs already described, we obtain the set of trajectories in the Figures 3.15 to 3.18. Figure 3.15 shows the trajectories in an xy-plane projection in a Sun-centered inertial frame. Figure 3.16 shows the same trajectories in an Earth-centered inertial frame. Oblique views of both figures are given in Figures 3.17 and 3.18.

3.3 Three-Body Free Returns

The next goal of this chapter is to find and classify families of FRTs in the three-body Earth-Sun system, independent of any target body or mission objectives. The trajectories found in the three-body model may be compared to those found in the two-body model. Since a general closed-form analytical expression for

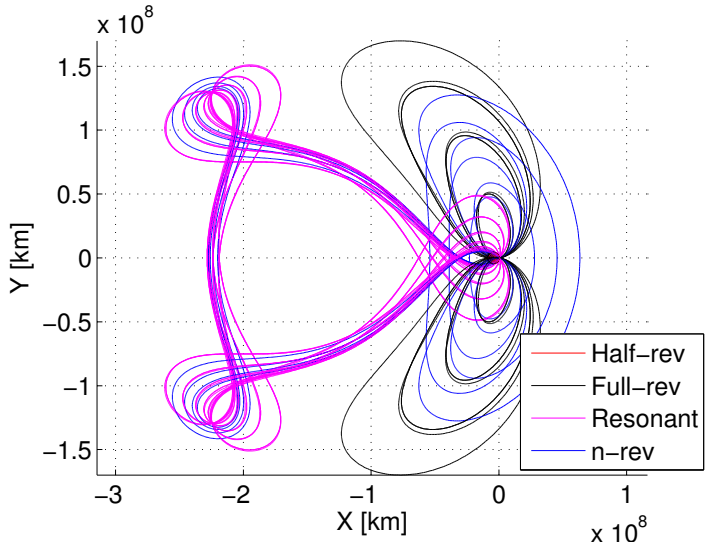

Figure 3.16: Types of feasible two-body FRTs, Earth-centered inertial frame

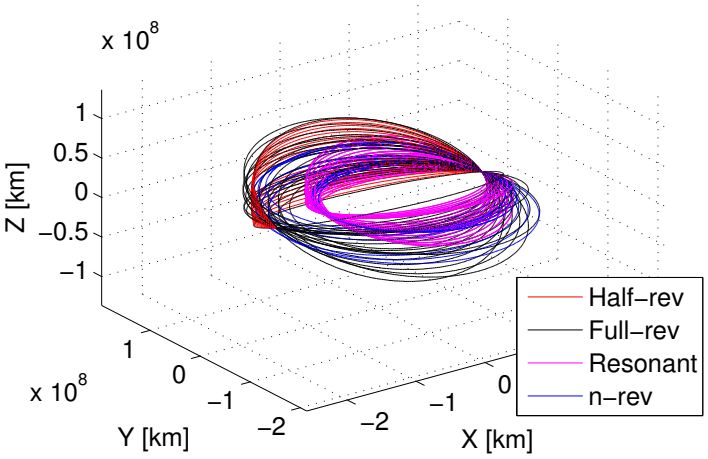

Figure 3.17: Types of feasible two-body FRTs, Sun-centered inertial frame, oblique view

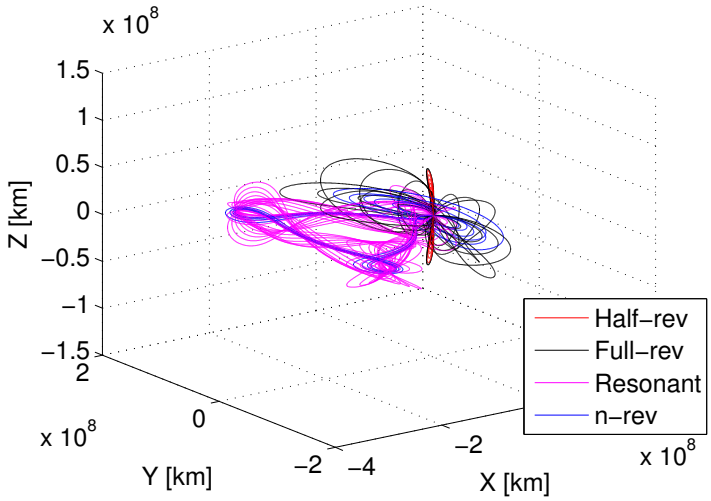

Figure 3.18: Types of feasible two-body FRTs, Earth-centered inertial frame, oblique view

a trajectory under the influence of two gravitating bodies does not exist, FRTs in a three-body model must be found using a numerical approach. In this section, it is desired simply to find a large number of FRTs in the three-body model, and later to classify them and compare them with their counterparts from the two-body model. The task of finding three-body FRTs is separated into two parts: numerical search, which is automated computationally, and manual classification. Numerical search is itself divided into parts: finding an initial guess, performing an initial feasible solution finder using Particle Swarm Optimization (PSO), and performing the final feasible solution finder using a standard sequential quadratic programming (SQP) optimization algorithm.

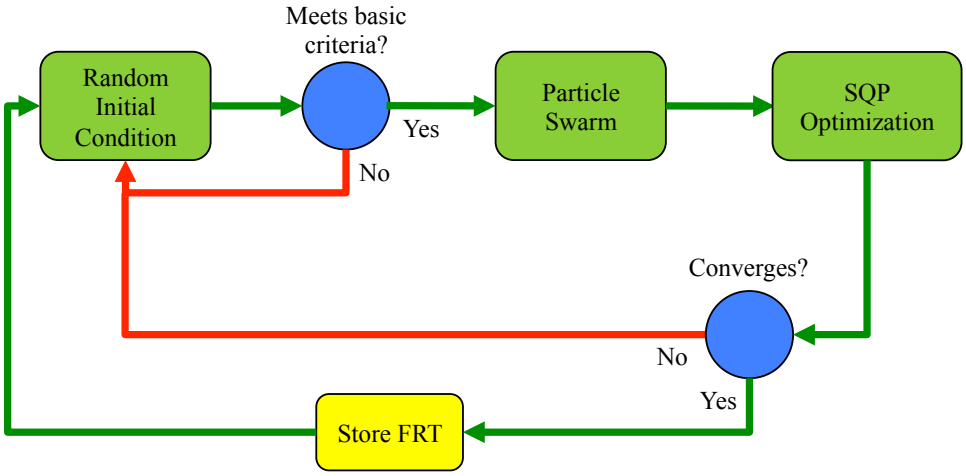

Figure 3.19: Flowchart for numerical search technique.

3.3.1 Numerical search

The numerical search technique consists of defining a search space for several quantities related to the trajectory, repeatedly selecting an initial guess at random from the defined space, and attempting to converge an FRT from the initial guess using a constrained numerical optimization routine with zero cost function. If the routine does not converge within a defined small number of iterations, then the initial guess is abandoned and a new one is selected at random. This approach is feasible because the goal is simply to find a large number of FRTs, not to formulate an algorithm that converges all given initial conditions. The search technique is summarized in the flowchart in Figure 3.19.

The search space is parameterized into two separate orbit segments. This method facilitates quicker and more accurate convergence, since the final states of large and lengthy trajectories are very sensitive to small changes in the initial condi-

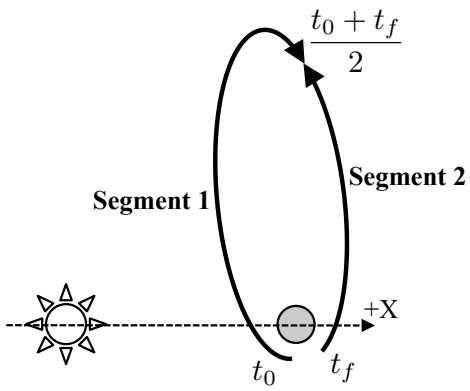

Figure 3.20: Trajectory segments, forming a continuous Free Return Trajectory upon convergence.

tion. Dividing the full trajectory into two segments is more numerically amenable, and leads to more accurate results.

The first segment begins near the Earth and is propagated forward in time for half of the total time of flight. The second segment *ends* near the Earth, and is propagated backward in time for half of the total time of flight. Upon convergence, the two trajectories meet at a midpoint with the same position and velocity state, thus creating a smooth trajectory from beginning to end. Figure 3.20 shows the two separate segments and corresponding times.

The first segment begins at time $t_0 = 0$. Its initial position is defined to be at a distance $r_0 = 6778$ km, which corresponds to an altitude of 400 km. This value is chosen to be consistent with other studies in later chapters. The angles ϕ_0 (latitude out of the orbital plane) and λ_0 (longitude counterclockwise from the +x axis) complete the parameterization of the initial position, and are free to be adjusted by the optimization algorithm. The three elements of the initial velocity

vector are defined by v_0 (scalar speed), α_0 (velocity right ascension), and δ_0 (velocity declination). The trajectory is propagated numerically in time from t_0 to the half of the total time, or $(t_0 + t_f)/2$.

In a similar manner, the second segment ends at time t_f, which is a free parameter. The trajectory is propagated backward in time to $(t_0 + t_f)/2$, where it meets the first segment upon convergence. The final position magnitude of the second segment is chosen as $r_f = 7000$ km, and the quantities ϕ_f, λ_f, v_f, α_f, and δ_f are all defined similarly to their counterparts in the first segment.

A constraint is applied to force the flight path angle (FPA) of the inbound and outbound trajectories to be zero. This condition approximates a realistic departure and return scenario, where the spacecraft leaves from a circular low-Earth orbit and returns near a re-entry interface condition. The FPA constraint eliminates one unknown quantity from each velocity state, which is arbitrarily chosen to be δ. The FPA is defined to be zero when $\mathbf{r} \cdot \mathbf{v} = 0$ in the rotating frame. This constraint leads to δ being defined by Eq. (3.4).

$$\delta = \tan^{-1}\left(\frac{-\cos(\lambda)\cos(\alpha) - \sin(\lambda)\sin(\alpha)}{\tan(\phi)}\right) \tag{3.4}$$

In summary, the parameter vector for optimization is given in Eq. (3.5), and the initial and final states are defined in Eq. (3.6).

Table 3.1: Representative search space for the free state elements.

State	Min	Max
ϕ	0 deg	360 deg
λ	0 deg	360 deg
v	11.0 km/s	15.0 km/s
α	0 deg	360 deg
t_f	30 days	750 days

$$\mathbf{x}_p = \begin{bmatrix} \phi_0 \\ \lambda_0 \\ v_0 \\ \alpha_0 \\ \phi_f \\ \lambda_f \\ v_f \\ \alpha_f \\ t_f \end{bmatrix}_{9\times 1} \tag{3.5}$$

$$\mathbf{r}_0 = r_0 \begin{bmatrix} \cos(\lambda_0)\cos(\phi_0) \\ \sin(\lambda_0)\cos(\phi_0) \\ \sin(\phi_0) \end{bmatrix} \quad \mathbf{r}_f = r_f \begin{bmatrix} \cos(\lambda_f)\cos(\phi_f) \\ \sin(\lambda_f)\cos(\phi_f) \\ \sin(\phi_f) \end{bmatrix}$$

$$\mathbf{v}_0 = v_0 \begin{bmatrix} \cos(\alpha_0)\cos(\delta_0) \\ \sin(\alpha_0)\cos(\delta_0) \\ \sin(\delta_0) \end{bmatrix} \quad \mathbf{v}_f = v_f \begin{bmatrix} \cos(\alpha_f)\cos(\delta_f) \\ \sin(\alpha_f)\cos(\delta_f) \\ \sin(\delta_f) \end{bmatrix} \tag{3.6}$$

3.3.1.1 Initial condition

Each parameter in the state vector has a defined search space size by which to determine the initial conditions. The search space size may be varied for different executions of the algorithm, and a representative example is given in Table 3.1.

At each iteration, a random value for each state is chosen from the specified state space according to a uniform distribution. Using Eqs. (3.4) and (3.6), these values yield an initial condition for the optimization subroutine. If the initial condition does not meet certain initial requirements of patch point position and velocity discrepancies after initial numerical propagation, the guess is discarded and a new one is chosen. The discrepancy cutoff values may vary between different executions of the algorithm, but typical values require that the magnitude of the position difference is no more than 1×10^7 - 2×10^7 km and the magnitude of the velocity difference is no more than 10 km/s. These broad cutoffs are applied so that the initial guess delivered to the Particle Swarm Optimization algorithm is already reasonably in the vicinity of a feasible trajectory.

3.3.1.2 Particle Swarm Optimization

The initial condition undergoes a small number of iterations in a Particle Swarm Optimization (PSO) algorithm. PSO algorithms are used throughout the literature; they were first introduced by Kennedy and Eberhart [54], and have been utilized in engineering applications by several authors, including Pontani and Conway, who showed the algorithm's utility in converging several types of feasible space trajectories [83]. In short summary, the algorithm relies on the performance of several "particles," which represent states in a specified state-space. For constrained optimization, the "particles" determine their best individual and overall states as calculated with a penalty function, and move through the state space based on a

combination of their own and the group's overall "best" visited states and their current "inertia."

In this application, a specified number of particles are randomly generated around the randomly selected initial condition. The performance of each particle is determined by a penalty function, which represents the goal of matching the position and velocity of the initial and final trajectory segments. For this algorithm, the penalty function is given in Eq. (3.7). This amounts to a weighted sum of the position and velocity differences after the integration; a converged trajectory has a penalty function value of $J = 0$. The subscripts represent the state after integration at the patch time t_m for the first (1) and second (2) segment of the trajectory. Note the choice of weighting coefficient for the cost function. In this manner, a discrepancy of 1 km and 1 m/s will have the same penalty function value as a discrepancy of 100 km and 0.1 m/s.

$$J = 10^{-4} \left| \mathbf{r}_2 - \mathbf{r}_1 \right| + 10^2 \left| \mathbf{v}_2 - \mathbf{v}_1 \right| \tag{3.7}$$

Every particle's state is evaluated according to Eq. (3.7). The particles then "move" (their states are updated) according to the method described by Ref. [54]; this update consists of the state ($\mathbf{x}$) at iteration $i + 1$ being updated from iteration i according to Eq. (3.8)

$$\mathbf{x}_{i+1} = \mathbf{x}_i + \mathbf{w}_{i+1} \tag{3.8}$$

Where:

$$\mathbf{w}_{i+1} = c_I \mathbf{w}_i + c_C(\mathbf{p}_{best} - \mathbf{x}_i) + c_S(\mathbf{g}_{best} - \mathbf{x}_i) \tag{3.9}$$

$$c_I = \frac{1 + R_1}{2}, \quad c_C = 1.49445 R_2, \quad c_S = 1.49445 R_3 \tag{3.10}$$

In the above equations, R_i is a random number selected from $[0, 1]$, $\mathbf{p}_{best}$ is the best state ever visited by the particle, and $\mathbf{g}_{best}$ is the best state ever visited by any particle. The initial state update $\mathbf{w}_0$ is chosen as a small quantity in a random state direction to give the particles a small initial inertia. The coefficient values (c_I, c_C, and c_S) are the same as those used in Ref. [83], since the goal of both algorithms is on the scale of large spacecraft trajectories. In other applications, these numbers may be tuned to provide different convergence criteria.

Initially, this classification algorithm involved only a sequential quadratic programming (SQP) routine for numerical optimization. It was found that by adding a small number of PSO iterations before the SQP algorithm, the convergence success rate increased. Essentially, the PSO "improves" the initial condition to one that is more amenable to the SQP algorithm. To investigate the effect of the PSO on the initial guess, the number of particles and iteration steps are varied to determine the reduction in the cost function according to Eq. (3.7). The cost function is evaluated for each random initial guess that meets the cutoff criteria, and then evaluated for the "best" (lowest cost) solution that the PSO produces. The reduction of the cost function for varying numbers of particles and iterations is shown in Table 3.2, using 2000 random initial guesses and cutoff criteria of 1.5×10^7 km and 10 km/s.

Table 3.2: Average cost function reduction using particle swarm optimization

		Iterations	
		5	10
Particles	5	32.3%	42.5%
	40	71.3%	80.3%
	50	75.4%	74.8%
	100	80.3%	77.6%

In summary, the initial conditions pass through a small number of iterations of a PSO, which improves the initial condition to a set of parameters that are closer to satisfying the conditions for a continuous FRT. After the specified number of iterations of the PSO, the "best" particle result is selected according to the lowest value provided by the penalty function. The resulting "best" state is then delivered to the SQP optimization algorithm for final convergence and constraint matching.

3.3.1.3 Sequential Quadratic Programming optimization.

The "best" result from the PSO algorithm undergoes a more classical SQP optimization procedure. Since the goal is simply to find a large number of FRTs to be classified, there is no traditional cost function associated with the optimization, as there is no specified quantity to be minimized. Rather, constraints are applied so that the converged solution represents a valid, continuous FRT in the state space. Equality (**c**) and inequality (**d**) constraints are given in Eq. (3.11).

$$\mathbf{c} = \begin{bmatrix} \mathbf{r}_{m,2} - \mathbf{r}_{m,1} \\ \mathbf{v}_{m,2} - \mathbf{v}_{m,1} \end{bmatrix}_{6\times 1} = \mathbf{0} \qquad \mathbf{d} = \begin{bmatrix} T_{max} - t_f \\ t_f - T_{min} \\ v_0 - v_{min} \\ v_f - v_{min} \\ v_{max} - v_0 \\ v_{max} - v_f \end{bmatrix}_{6\times 1} \geq \mathbf{0} \tag{3.11}$$

The equality constraints require that the integrated states of the first and second trajectory segments are equal at the patch time. The inequality constraints constrain the flight time to be within specified bounds (T_{max} and T_{min}), and constrain the inbound and outbound speed to be within specified values (v_{max} and v_{min}). Upon convergence of a valid trajectory, the constraints are satisfied to within a user-specified tolerance.

The optimization procedure utilizes the gradients of the constraints with respect to the elements of the parameter vector; that is, $\partial\mathbf{c}/\partial\mathbf{x}_p$ and $\partial\mathbf{d}/\partial\mathbf{x}_p$ must be supplied. These gradients, often known as "analytical" gradients, have been calculated and are supplied in Appendix A. Although calculation of analytical gradients is often tedious, their implementation and calculation is much faster computationally when executing the algorithm, whereas an alternative such as finite differencing may be too computationally intensive and less accurate.

Analytical gradients require computation of the state transition matrix (STM) between two states. The STM is a first-order approximation of the propagations of state variations over time, and may be computed numerically by integration using Eq. (3.12), where the initial condition $\mathbf{I}$ is the identity matrix. A full description and

treatment of the STM is given in Battin [7], and elsewhere.

$$\dot{\mathbf{\Phi}} = \frac{\partial f(\mathbf{x})}{\partial \mathbf{x}} \mathbf{\Phi} \ , \qquad \mathbf{x} = \begin{bmatrix} \mathbf{r} \\ \mathbf{v} \end{bmatrix} \ , \quad f(\mathbf{x}) = \begin{bmatrix} \mathbf{v} \\ \ddot{\mathbf{r}} \end{bmatrix} \ , \quad \mathbf{\Phi}(0,0) = \mathbf{I} \tag{3.12}$$

A full Jacobian of the first partial derivatives of each constraint with respect to each input parameter is computed at each iteration, as are the gradients of the cost function with respect to each input parameter. To compute the gradients analytically, Eq. (3.13) is used to relate the differentials of the state at any time t_{i+1} to any other time t_i. This result is shown and derived in detail by Ocampo and Munoz [74].

$$d\mathbf{x}_{i+1}^{+} = \mathbf{\Phi}(t_{i+1}, t_i) \left[d\mathbf{x}_i^{-} + d\Delta\mathbf{x}_i - \dot{\mathbf{x}}_i^{+} dt_i \right] + \dot{\mathbf{x}}_{i+1}^{-} dt_{i+1} + d\Delta\mathbf{x}_{i+1} \tag{3.13}$$

Therefore, given the state and the STM between any two times, the full Jacobian matrix of first order partial derivatives may be obtained for the optimization routine. The expressions for this application are given in Appendix A.

In summary, the state from the PSO algorithm undergoes SQP optimization so that the final result is one smooth FRT, beginning and ending near the Earth. The result is not unique, since there is no cost function to be minimized, so the process may be repeated indefinitely to find many more FRTs. If the SQP algorithm does not converge on a valid FRT in the specified number of iterations for whatever reason, the optimization process is abandoned and another initial condition is selected.

3.3.2 Manual classification

Upon convergence of a large number of valid FRTs, each solution may be classified as one of several different types. Classification is accomplished by finding

other FRTs in the same "family", and categorizing them based on common characteristics. For each FRT, a similar optimization convergence procedure is used with the converged solution as an initial condition, but the total trajectory time is varied incrementally to find orbits that satisfy slightly shorter and longer periods. The result is a family of orbits, which is visually analyzed for prominent characteristics.

First, elements of the converged parameter vector are used to form a new parameter vector, eliminating the time parameter. The new parameter vector is given in Eq. (3.14).

$$\mathbf{x}_p = \begin{bmatrix} \phi_0 \\ \lambda_0 \\ v_0 \\ \alpha_0 \\ \phi_f \\ \lambda_f \\ v_f \\ \alpha_f \end{bmatrix}_{8\times 1} \tag{3.14}$$

At each iteration, the total trajectory time is altered in increments of one day, beginning with the original converged time of flight. This new total time is fixed, so the optimization algorithm alters the other parameters to form a new continuous FRT. The new equality and inequality constraints for the SQP algorithm are given in Eq. (3.15).

$$\mathbf{c} = \begin{bmatrix} \mathbf{r}_{m,2} - \mathbf{r}_{m,1} \\ \mathbf{v}_{m,2} - \mathbf{v}_{m,1} \end{bmatrix}_{6\times 1} = \mathbf{0}, \qquad \mathbf{d} = \begin{bmatrix} v_0 - v_{min} \\ v_f - v_{min} \\ v_{max} - v_0 \\ v_{max} - v_f \end{bmatrix}_{4\times 1} \geq \mathbf{0} \tag{3.15}$$

After iterating this procedure for many total trajectory time solutions, all solutions are visualized in the same figure so that a "family type" may be determined according to prominent characteristics, such as shape, direction, and time of flight. Results and a sample procedure are shown next.

3.4 Classification results

Upon execution of the classification algorithm, hundreds of FRTs are found and classified by family. The results shown were obtained by applying several different search spaces, and are presented without reference to any specific target body; that is, these results exist independent of destination. The cutoffs in the algorithm for initial position and velocity magnitude discrepancies were selected to be 1.5×10^7 km and 10 km/s, respectively. Trajectories meeting these criteria were refined using the PSO algorithm, and those meeting the constraints after application of the SQP optimization algorithm were retained. The specific SQP algorithm used in these results is `VF13` [4], operating in Fortran.

The trajectories converged using these criteria vary in flight time from half-revolution to two-revolution, and all trajectories are shown together in an Earth-centered rotating frame in Figures 3.21 and 3.22. A full view is shown in Figure 3.21 (top and oblique), and a view zoomed in on the Earth is shown in Figure 3.22 (top and oblique). Note that in the oblique views, the Sun is to the bottom left, and the highly out-of-plane half-revolution trajectories "curve toward" the Sun.

These FRTs resemble very closely the theoretical two-body results shown in Figures 3.16 and 3.18. The majority of trajectories found represent the highly

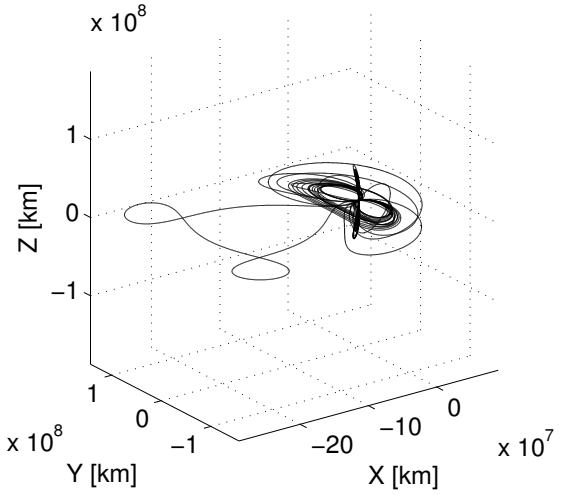

(a) Oblique view

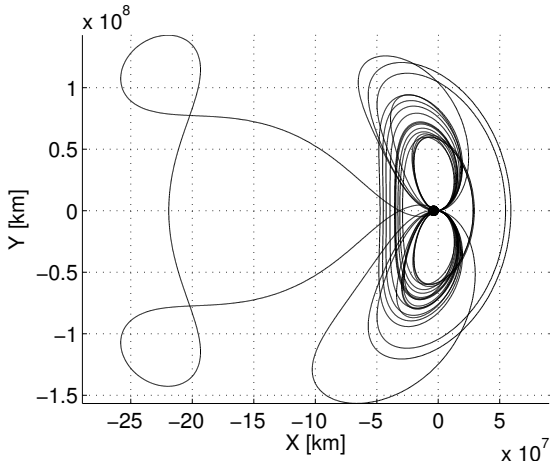

(b) Top view

Figure 3.21: FRTs in an Earth-centered rotating frame

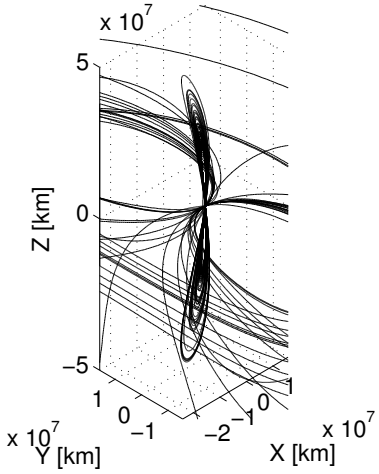

(a) Oblique view

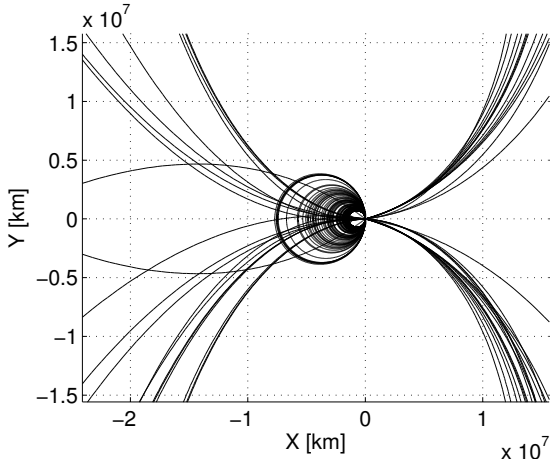

(b) Top view

Figure 3.22: FRTs in an Earth-centered rotating frame, zoomed on Earth

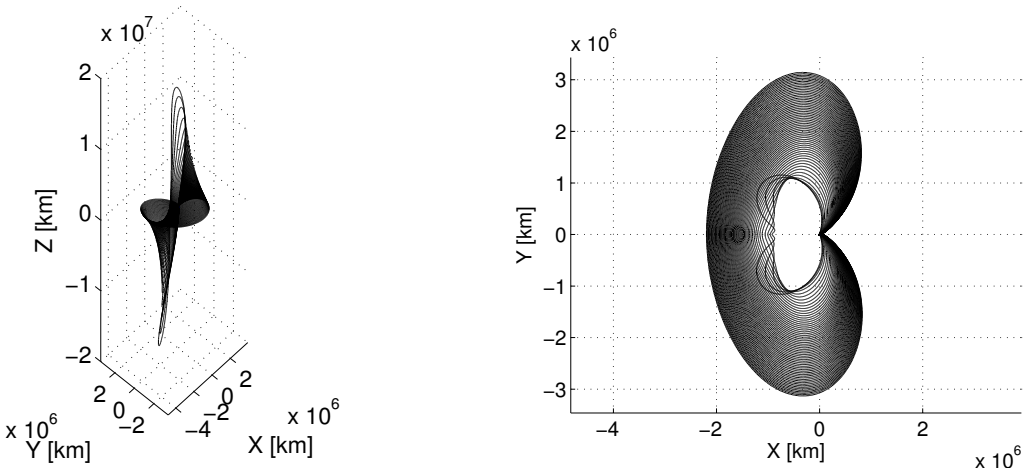

(a) Oblique view

(b) Top view

Figure 3.23: An example of a Type II$^-$ FRT family

out-of-plane trajectories that extend primarily in the ± z direction from the ecliptic plane. These orbits are closely related to two-body half-revolution return trajectories shown in Figure 3.1. In the ideal Sun-centered inertial frame, these orbits are nearly circular and slightly inclined to the ecliptic plane. Due to the gravitational effects of the Earth, these orbits are not exactly half-revolution phasing orbits, but are very closely related.

To classify an FRT, each one is individually selected, and then a family is formed by varying the overall time of flight and re-converging the trajectory according to the algorithm described in Section 3.3.2. An example of a resulting family is shown in Figure 3.23, with an oblique view given in subfigure (a) and a top view (looking in the -z direction) shown in subfigure (b). This particular family exhibits a "kidney bean" shape, which is symmetric about the x axis.

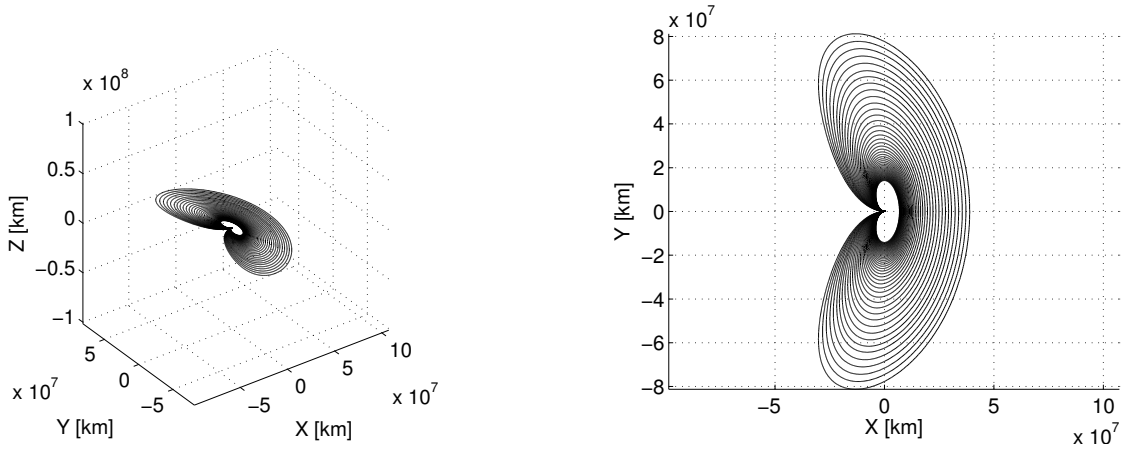

(a) Oblique view

(b) Top view

Figure 3.24: An example of a type III$^+$ FRT family

An example of a planar "kidney bean" family is shown in Figure 3.24, with an oblique view given in subfigure (a) and a top view (looking in the -z direction) shown in subfigure (b).

An example of a planar "cloverleaf" family is shown in Figure 3.25, with an oblique view given in subfigure (a) and a top view (looking in the -z direction) shown in subfigure (b). This trajectory is a clear example of the analogous two-body trajectories in Figure 3.14.

Each of the trajectories is used as a "seed" to generate a family of trajectories using this method. Upon completion, it is apparent that there are six unique trajectory types that appear, separating these trajectory families into more precise categories than simply "near-plane" and "out-of-plane." The categories with accompanying descriptions of the family characteristics are given in Table 3.3. A majority

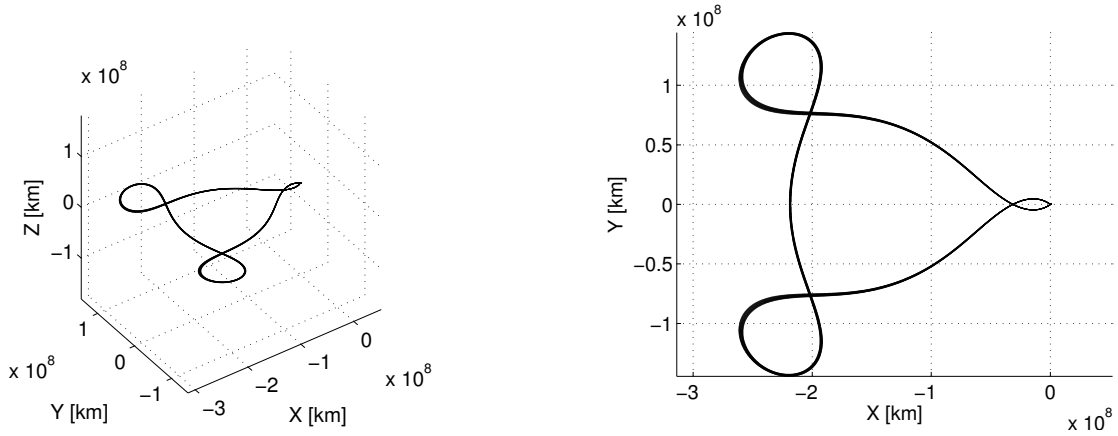

(a) Oblique view.

(b) Top view.

Figure 3.25: An example of a type VI$^+$ FRT family

of converged FRTs using this method are either Type I$^-$ or I$^+$. Examples of each type of trajectory are shown in Figure 3.26.

Comparing the CRTBP results with the two-body results shows that Type I trajectories are analogous to half-revolution orbits (Figure 3.1), Types II, III, and IV are different variations on full-revolution orbits (Figure 3.2), and Type VI corresponds to multi-revolution resonant orbits (Figure 3.14). The distribution of converged total times of flight is shown in Figure 3.27; the vast majority of trajectories converged represent the half-year trajectories (Type I). Other converged solutions fall on half-integer year durations, but the n-revolution Lambert FRTs do not exhibit half-integer year flight times.

To show that these FRTs are not simply closed orbits around the Earth, the two-body energy with respect to the Earth is shown in Figure 3.28. The two-body energy E is calculated using Eq. (3.16), where ${}^I v_s$ represents the spacecraft's instan-

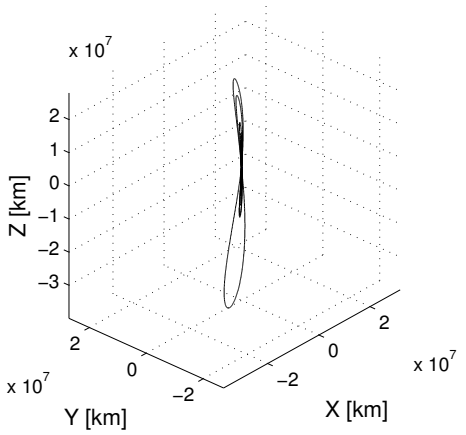

(a) Type I^- and I^+.

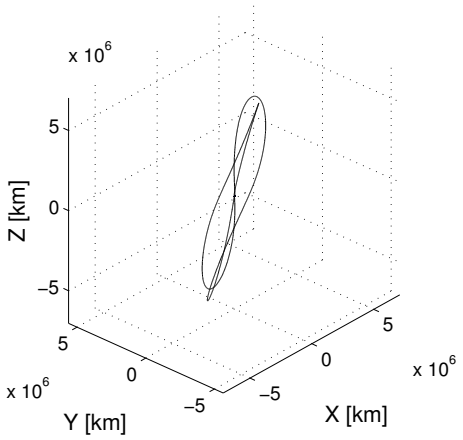

(b) Type II^- and II^+.

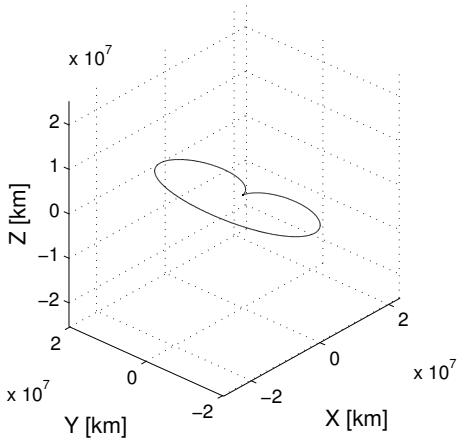

(c) Type III^-.

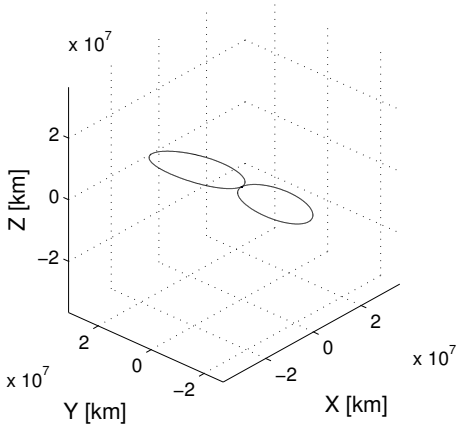

(d) Type IV^- and IV^+.

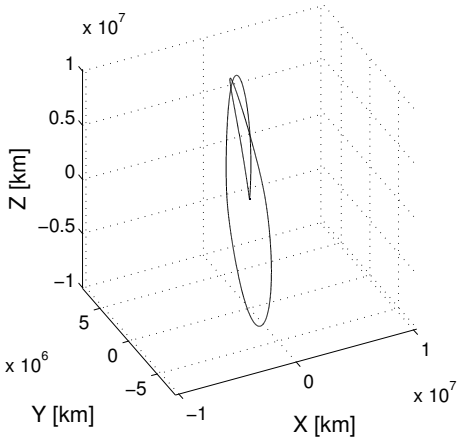

(e) Type V^+.

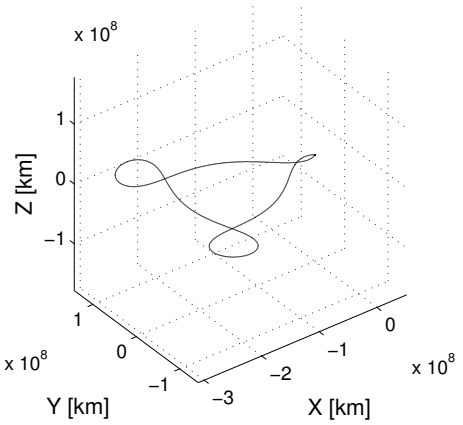

(f) Type VI^+.

Figure 3.26: Example trajectories of each family type.

Table 3.3: FRT family classifications

Family	Description
I^-	Below ecliptic plane, large -z component (half rev)
I^+	Above ecliptic plane, large +z component (half rev)
II^-	"Kidney," out-of-plane, initial -y direction (single rev)
II^+	"Kidney," out-of-plane, initial +y direction (single rev)
III^-	"Kidney," in-plane, initial -y direction (single rev)
III^+	"Kidney," in-plane, initial +y direction (single rev)
IV^-	Large "oval," in-plane, initial -y direction (single rev)
IV^+	Large "oval," in-plane, initial +y direction (single rev)
V^-	"Spiral," out-of-plane, initial -y direction (>1 rev)
V^+	"Spiral," out-of-plane, initial +y direction (>1 rev)
VI^-	"Cloverleaf," initial -y direction (>2 rev)
VI^+	"Cloverleaf," initial +y direction (>2 rev)

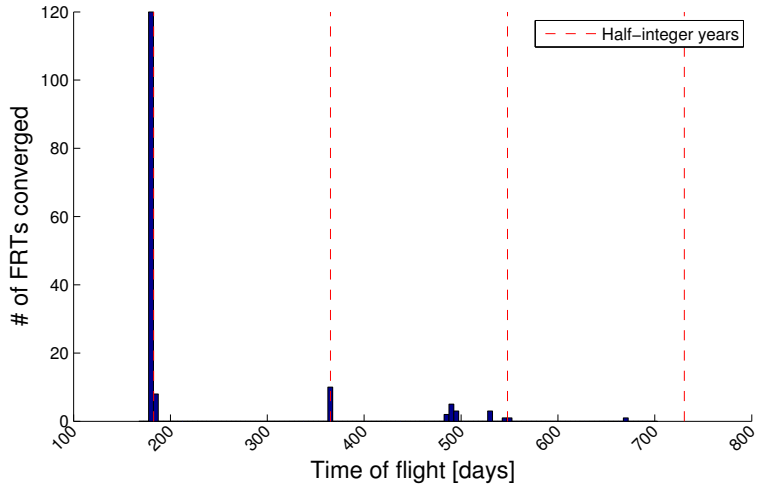

Figure 3.27: Histogram of converged times of flight for Earth-centered FRTs

taneous inertial speed with respect to Earth, and r_s is the instantaneous distance from the spacecraft to the Earth. Note that energy is conserved in a two-body gravitational model, but varies with time in the three-body system due to the Sun's influence.

$$E = \frac{\left({}^{I}v_s\right)^2}{2} - \frac{\mu}{r_s} \tag{3.16}$$

Upon Earth departure, every FRT has positive energy with respect to Earth, indicating a hyperbolic escape orbit. Most FRTs eventually attain negative energy, indicating that the osculating two-body orbit at that time would be closed. However, due to the dynamics of the CRTBP, the FRTs once again attain positive energy upon approach and return to Earth. The Type VI trajectory attains a very high specific energy with respect to the Earth, and Figure 3.29 shows the Earth-centered specific energy zoomed in on the other trajectories.

3.5 Chapter conclusion

In both the two-body and restricted three-body models, there exist a variety of distant free-return trajectories that begin and end near the Earth with no intermediate velocity adjustments. While the two-body trajectories may be easily generated analytically, the three-body trajectories must be found numerically. In this chapter, an algorithm is presented to find and manually classify free-return trajectories in the circular restricted three-body model. These trajectories may be classified into different families, grouped according to common shape, direction, and time of

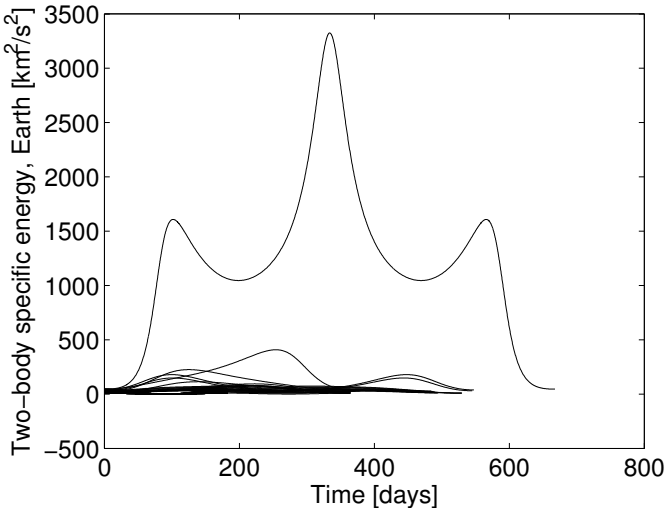

Figure 3.28: Instantaneous two-body energy with respect to the Earth

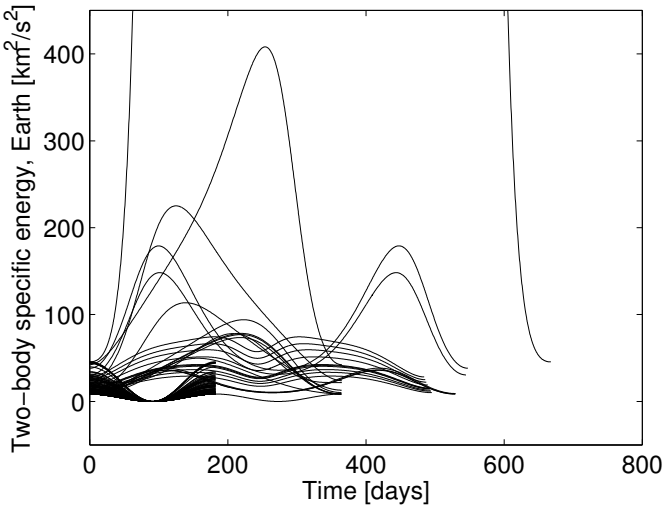

Figure 3.29: Instantaneous two-body energy with respect to the Earth, zoomed

flight. Many trajectories are immediately comparable to their two-body counterparts, though all trajectories are shown to experience some deviation from the ideal two-body model due to the presence of Earth's gravity. Most trajectories found are Type I, corresponding to half-revolution FRTs. Other types are found and classified. The result of this chapter is a "library" of FRTs in the three-body model (see digital supplemental material for a text file of initial conditions for hundreds of these FRTs. Information about this text file is given in Appendix G). This orbit library is a key component in the next chapter, where trajectories are utilized as mission segments in paths to Near-Earth Asteroids.

Chapter 4

Utilizing Free Return Trajectories to Reach Near-Earth Asteroids

4.1 Chapter introduction

This chapter describes the application of an Earth-centered Free Return Trajectory (FRT) to the problem of asteroid rendezvous. Optimal asteroid rendezvous with impulsive maneuvers has long been a subject of interest in the astrodynamical community; the pertinent literature is discussed in Chapter 1.

As a specific destination, Near-Earth Asteroids (NEAs) have attracted much attention in recent decades for purposes of mining, colonization, and exploration, as detailed in Section 1.4.1. Especially in the past decade, manned missions to asteroids have become a salient topic in spaceflight, as we are now aware of the real threat of a catastrophic asteroid impact on Earth. NEAs are specifically being pursued as targets of manned missions for purposes of mining, deep-space survival testing, and impact threat mitigation. It is crucial to determine optimal trajectories to reach these bodies so that propellant mass and/or flight time may be minimized. While velocity- and fuel-optimal trajectories have been investigated, NEA missions that take astronaut safety into account via trajectory design have received little treatment previously in the literature.

When proposing manned missions into space, risk mitigation and crew safety are important considerations as mission design factors. Simply optimizing a trajectory for fuel or time is insufficient to mitigate risks to astronaut safety. Gil-Fernandez, et al. [39] performed work on emergency trajectory analysis for quick Earth-return in case of an anomaly, and argued that conventional optimization methods for robotic missions must be augmented for a crewed mission. For instance, if a catastrophic engine failure occurs during transfer to a target body, there is little chance of vehicle recovery or crew rescue without an appropriately designed trajectory, and saving fuel is no longer the critical concern.

To partially mitigate the crew safety risk during the Apollo program, trajectory designers utilized FRTs, which return to their point of origin with no propulsive maneuvers. With a simple velocity adjustment in low Earth orbit, the Apollo spacecraft embarked upon an FRT or hybrid FRT for a significant portion of their journey. Another velocity adjustment could be performed to depart from the FRT for lunar orbit insertion or lunar landing. However, if an anomaly occurred before departing the FRT, the spacecraft could have bypassed the lunar velocity maneuver, and, with no extra maneuvers, would return to Earth for atmospheric re-entry.

The same concept may be applied to rendezvous with NEAs. By utilizing Earth-centered FRTs, a spacecraft may begin its voyage to an NEA on a trajectory that returns near its point of origin close to the Earth, such as those described in the previous chapter. Previous missions that used similar trajectory types to perform sample collection missions for cometary flybys are summarized well by Farquhar [36]. For manned missions, if an anomaly occurs en route to the NEA (e.g. a main engine

failure or loss of propellant), the crew may remain on the FRT and return to Earth without applying any velocity maneuver. However, if the mission proceeds nominally, the spacecraft may optimally depart from the FRT to rendezvous with the NEA, stay for a period of time, and optimally return to the Earth along a different trajectory.

Presented in this chapter is a method for determining Δv-optimal trajectories utilizing FRTs in the CRTBP to rendezvous with an NEA. Trajectories in classified families from the previous chapter are searched to determine viable trajectories to visit various NEAs using an FRT for risk mitigation. Searching is accomplished using a Lambert targeting algorithm to calculate transfer orbits between the FRTs and a target NEA, instead of simply targeting orbits that directly connect Earth to the asteroid. Similar methods have been used to calculate FRTs between other solar system bodies by using gravitational assist maneuvers [114]. This procedure provides an excellent initial guess in the CRTBP, and an optimization algorithm is applied to the result to obtain a continuous trajectory. Five example trajectories are presented: one for each of the five lowest Δv targets as determined by an accessibility study conducted by NASA's Planetary Science Division [2]. These same asteroids are studied here with the same departure and arrival scenario to provide a comparison between the FRT algorithm and the accessibility study.

A manned rendezvous mission with these bodies would facilitate sample return and dynamical characterization, and could provide a testbed for potential future deflection attempts. The same algorithm presented here is applicable to rendezvous missions with a wide variety of NEAs; the cases presented here simply serve to demonstrate representative results. As a whole, the algorithms presented in this

chapter may be used to explore the families of FRTs around a central body, to automatically select a single trajectory to be used as a segment in a mission to a certain target body, and to converge the initial guess into a fully continuous trajectory. This technique is useful for mission design involving human voyages to NEAs, where an FRT provides a valuable abort option to mitigate mission risk that a direct transfer does not provide. The work in this chapter is based on a peer-reviewed journal publication in the Journal of Guidance, Control, and Dynamics [14] and the conference proceeding from the previous chapter [13].

4.2 Initial guess method

Because FRTs are useful for visiting NEAs, it is of interest to define an algorithm to determine a viable FRT to visit a specific NEA over a specified time span. It is useful to develop a method to autonomously determine initial conditions for a full optimization routine incorporating FRTs to reach NEAs. This section describes an approach using Lambert's problem to search the families of FRTs produced in the previous chapter to determine a suitable initial condition for a full numerical optimization routine.

4.2.1 Lambert's problem

Lambert's problem is ubiquitous throughout the literature, and has been well-described by innumerable sources. Battin succinctly quotes Lambert's original theorem as, "the orbital transfer time depends only upon the semimajor axis, the sum of the distances of the initial and final points of the arc from the center of force, and

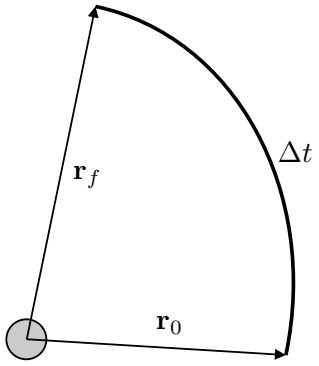

Figure 4.1: Geometry of single-revolution Lambert's problem

the length of the chord joining these points." [7] The theory can be extended to state that a unique single-revolution orbit in the two-body problem may be determined simply by knowing two position vectors, the time of flight between them, and the direction of travel. Additionally, if the orbit is known, then the position and velocity at any time are also known. A simple diagram of the inputs to Lambert's problem is shown in Figure 4.1.

Lambert's theorem and its extensions are used here to determine orbits in a two-body Sun-centered frame that depart from an FRT and rendezvous with an asteroid of choice. By calculating a large number of Lambert trajectories departing from the FRTs, it can be determined which trajectory represents the lowest Δv to rendezvous with the target asteroid. By extracting this "best" Lambert orbit with its associated "best" FRT, an initial guess is generated for a full optimization routine. Using a Sun-centered Lambert algorithm is a valid approximation here, because the transfer orbits depart the FRTs and rendezvous with the asteroid relatively far from Earth, reducing Earth's gravitational effects on the CRTBP dynamical solution.

A large number of numerical routines exist to perform Lambert's method on a specified problem. For purposes of this chapter, the method of universal variables is used, which is described in-depth by Vallado [109].

4.2.2 Sorting with the Lambert algorithm

The next step involves successively calculating trajectories between each FRT and a specified asteroid at a specified date. An enumerated procedure is given in Algorithm 1.

Algorithm 1 Procedure to determine trajectories between FRTs and NEAs

```
1: Begin with full set of FRTs converged using the classification algorithm (see
   Chapter 3)
2: Specify the range of acceptable arrival dates at a specific NEA
3: Discretize the asteroid's orbit into a finite number of states over the range of
   acceptable dates
4: Select times of flight, either randomly or systematically from a list
5: for Each FRT in full set do
6:    Discretize FRT into finite number of states
7:    for Each point on the FRT do
8:       for Each point on the NEA orbit do
9:          for Each distinct time of flight do
10:            Determine the 1-rev orbit between the two points given by the solution
               to Lambert's problem
11:            Determine the total two-impulse Δv required
12:            if Total Δv is lower than current best then
13:               Store the total Δv, relevant times, and FRT chosen
14:            end if
15:         end for
16:      end for
17:   end for
18: end for
```

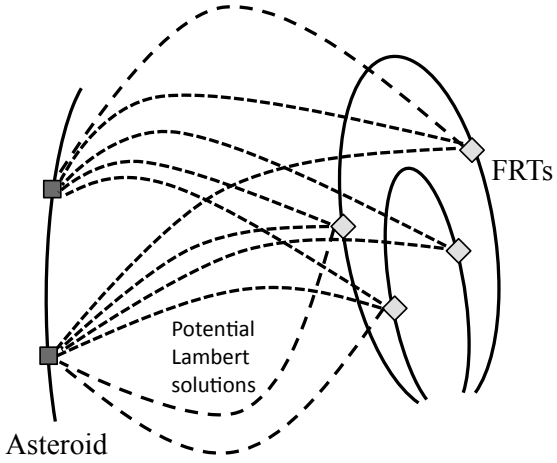

Figure 4.2: Lambert trajectory segments

Figure 4.2 demonstrates an array of possible solutions by discretizing the orbits and investigating multiple FRTs, each of which is ranked according to the total change in velocity required to reach the target. Note that trajectories with different periods can exist between the same pair of points, yielding different possible solutions.

Consider defining one target asteroid and discretizing its orbit into n specified points. Consider then obtaining m FRTs from the classification algorithm. If each FRT is discretized into p points, and t different possible transfer times are used, then the number of Lambert orbits from this algorithm will be $n \times m \times p \times t$. The transfer trajectory with the lowest cost is simply stored and overwritten by successively "better" values. The result of this algorithm is that the procedure autonomously determines:

- Which FRT provides the best low-cost initial guess

- An appropriate time to leave the FRT
- An appropriate time to arrive at the target NEA

These quantities may be provided as initial conditions to an optimization algorithm to fully converge a feasible trajectory to rendezvous with the asteroid in a higher-order dynamical system, which is described in subsequent sections. Since the Lambert trajectory is found using a two-body dynamical system, its implementation will not be exactly correct in the CRTBP or any other higher order systems, and a numerical correction scheme (e.g. differential correction or optimization) will be necessary to completely converge the full trajectory. However, this method is a good first order approximation, since the Lambert trajectories are relatively far from Earth, and are therefore influenced mostly by the Sun's gravity, which is accounted for in the two-body model.

4.2.3 Trajectory segments

The trajectory of the spacecraft to the asteroid is separated into several segments to aid in convergence of the optimization routine. The segments are constructed as follows:

1. The first segment leaves an Earth parking orbit at t_0 forward in time to a single impulsive maneuver to depart the FRT at t_c.
2. The second segment proceeds from the impulsive maneuver at t_c forward in time to the asteroid rendezvous at t_a.

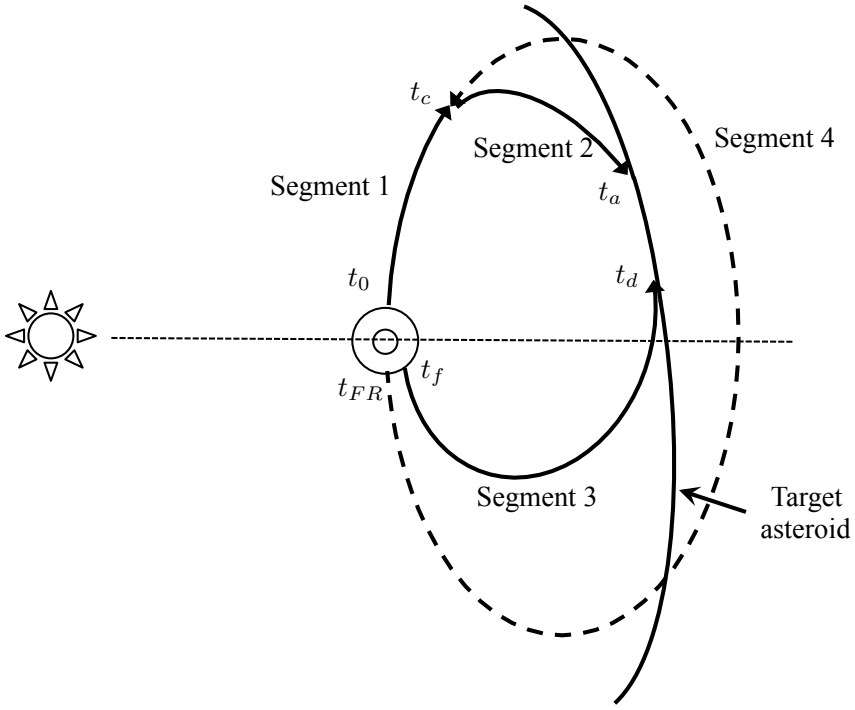

Figure 4.3: Diagram of separate trajectory segments in the optimization routine

3. The third segment consists of Earth re-entry at t_f backward in time to the asteroid departure at t_d.

4. The fourth segment propagates from Earth re-entry at t_{FR} backward in time to the impulsive maneuver at t_c, completing the FRT.

A visual representation of the separate segments is shown in Figure 4.3.

The segments are required to match boundary conditions and constraints, which are detailed in Section 4.5.1. Separating the full trajectory into several individual segments is beneficial for convergence due to long mission durations, and these segments are used to connect event nodes together sequentially in time. Small vari-

ations in an initial condition when integrating over long time intervals create large variations in the final state, which are not conducive to parameter optimization with long integration times.

4.3 NEA destinations

The NEAs selected for rendezvous in this chapter are chosen because of the relative ease of their accessibility as determined by the NHATS study [2]. The NEAs chosen are listed by NHATS as the five with the lowest round-trip Δv in a two-body Lambert targeting sense[1]. The NEA destinations along with their osculating orbital elements at epoch are listed in Table B.1 in Appendix B. The state of each asteroid at any given time is calculated by propagating the asteroid state from an initial epoch using Eq. (2.2).

The inertially referenced data in Table B.1 are converted to position and velocity using a standard algorithm in an inertial frame. The position and velocity are then transformed into an Earth-centered rotating frame. The state is numerically propagated from the initial epoch to some time t to determine the asteroid state at any given time. This method does present inaccuracies, since a long integration interval with simplified dynamics increases the model error over time. However, this method produces a good approximation of the actual system, and the converged parameters from this model may be used as a good initial guess in a more refined

[1]The NHATS survey calculates a two-body, patched conic Δv based on a maneuver to depart from a 400 km altitude Earth parking orbit, a Δv to rendezvous with the NEA, and a Δv to depart the NEA after a minimum stay time.

dynamical system. Additionally, propagating the asteroid in the same dynamical system as the spacecraft avoids numerical inconsistencies and potential problems for the optimizer (see Section 6.4 for more discussion on ephemeris matching). It is important to remember, however, that the substance of this chapter is not to refine dynamical models or propagate orbital elements, but to introduce the concept and calculation of optimal FRTs to NEAs using a reasonable dynamical model.

4.4 Examples of initial guesses

The problem considered is to find a suitable initial guess for rendezvous with each NEA by utilizing an FRT found among the FRTs described in the previous chapter. Each of the FRTs is discretized into 30 states consisting of position and velocity at an instantaneous time. These 30 states are separated equally in time over the full orbital period of each FRT.

For these example cases, the arrival at each asteroid is constrained to be between January 1, 2020 and January 1, 2040, and the Lambert transfer times are specified to be 20, 50, 80, 100, or 150 days in length. The asteroid states are discretized in 60 day intervals in the timespan, propagated in the CRTBP from epoch conditions given by the NHATS study [2]. The epoch states are given in Table B.1.

Between each discretized spacecraft state and each discretized asteroid state, the Lambert targeting routine is performed as described in Section 4.2. Once each calculation has been performed, the "best" trajectory is automatically selected according to the total Δv required to perform the transfer. For the specified constraints, the resultant initial conditions are shown in Figure 4.4 in the Earth-centered rotating

frame. Recall that the Lambert targeting algorithm operates in a two-body model, so the transfer trajectory does not meet the asteroid in the CRTBP until the parameters are fully optimized and meet continuity constraints.

A summary of the relevant dates is given in Table B.2 in Appendix B.

4.5 Optimization in the CRTBP

This section describes the method to converge the initial guesses in the CRTBP. While the FRTs in the initial guess were found in the CRTBP, the transfer arcs between the FRTs and the NEAs were found using a Lambert targeting method, which operates in a two-body heliocentric model. An optimization package is applied to the full initial guess to obtain a trajectory set that is continuous, satisfies constraints, and represents a local minimum in terms of Δv. The full parameters and constraints are described next.

4.5.1 Parameters and constraints

The optimization of the system is accomplished via constrained parameter optimization. The algorithm iterates on a set of input parameters to minimize a scalar cost function while satisfying equality and inequality constraints. For the CRTBP dynamical system, the parameters and constraints are given by Eq. (4.2). The free parameters here represent optimization of an FRT to a given asteroid with a rendezvous segment and return trajectory for a nominal mission. All departure and arrival times are free to be varied by the optimizer, as are the velocity impulses and components of the departure and arrival states. The inequality constraints

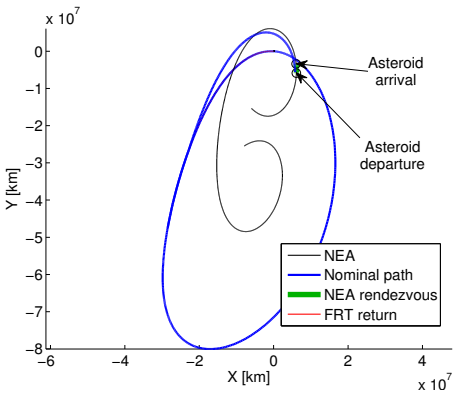

(a) 2000 SG344

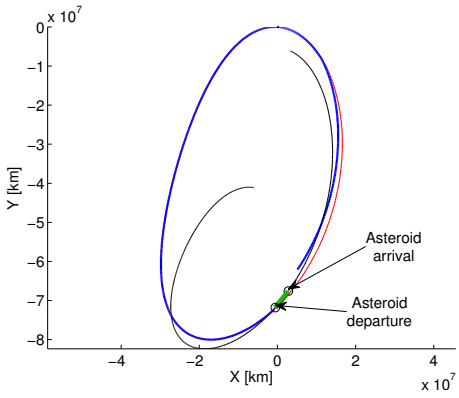

(b) 2006 BZ147

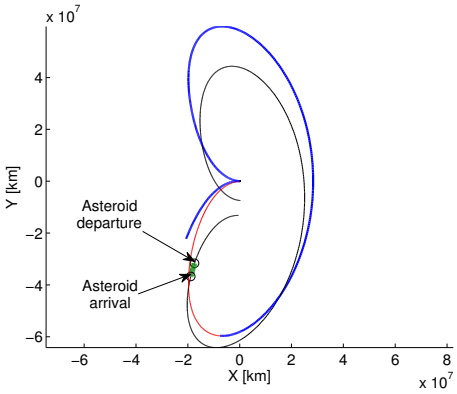

(c) 2009 HC

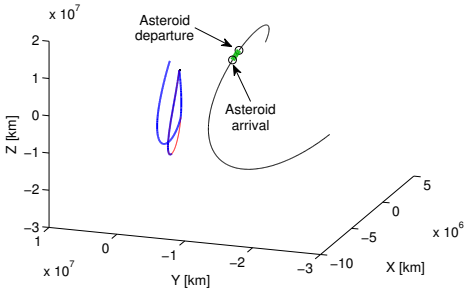

(d) 2001 FR85 (unequal axes)

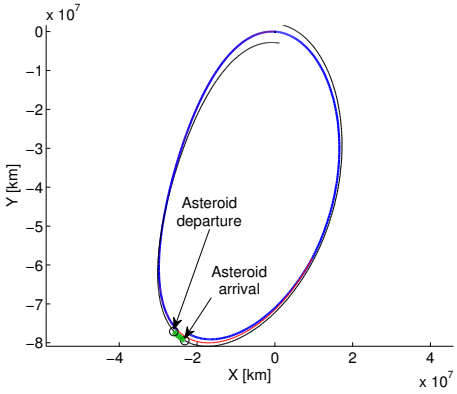

(e) 2012 UV136

Figure 4.4: Initial guesses to depart Earth for rendezvous with accessible NEAs

represent forward time for events in the mission, as well as minimum/maximum time duration and flight path angle constraints. The spacecraft must stay on the FRT for a minimum time of 14 days after Earth departure, and must stay in rendezvous with the asteroid for a minimum time of 10 days. In addition, the FRT must return to Earth within 600 days (to allow for up to 1.5-revolution FRTs), but the nominal asteroid mission does not have a maximum time constraint. These minimum/maximum times are used as examples, and may be altered to suit a particular mission design. The equality constraints ensure that the spacecraft performs rendezvous with the asteroid and that it is on an FRT for the first portion of its trajectory. It is also required for the departure trajectory to have a zero flight path angle (γ) with respect to Earth, assuming that the spacecraft departs from a circular low-Earth orbit, and that the arrival trajectories have a flight path angle that corresponds to a re-entry corridor. Flight path angle is defined numerically in Eq. (4.1), where $\mathbf{h}$ is the angular momentum vector, defined as $\mathbf{h} = \mathbf{r} \times \mathbf{v}$.

$$\cos(\gamma) = \frac{|\mathbf{h}|}{|\mathbf{r}||\mathbf{v}|} \tag{4.1}$$

The spacecraft is initially defined to be in a circular low-Earth orbit with a radius of 6778 km, which corresponds to an altitude of 400 km to be consistent with the NHATS study. An impulse is applied such that the resulting trajectory has $\gamma = 0$ deg. Upon return, both on the nominal trajectory and the FRT, the spacecraft state is defined by a re-entry corridor. At a return radius of 7000 km, the flight path angle must be $\gamma = -5$ deg. Because of the re-entry scenario, no impulse is applied upon Earth return.

It is important to note that the flight path angle constraints do not encompass every mission scenario, nor do they necessarily correspond to any particular mission. They simply reflect the type of constraint that could be applied when constructing an FRT to an NEA. The specific values should be changed for varying mission applications and requirements.

$$\mathbf{x}_p = \begin{bmatrix} t_0 \\ t_c \\ t_a \\ t_d \\ t_{FR} \\ t_f \\ \phi_0 \\ \phi_{FR} \\ \phi_f \\ \lambda_0 \\ \lambda_{FR} \\ \lambda_f \\ \mathbf{v}_0 \\ \Delta\mathbf{v}_c \\ \mathbf{v}_{FR} \\ \mathbf{v}_f \end{bmatrix}_{24\times 1}$$

$$\mathbf{d} = \begin{bmatrix} t_0 \\ t_a - t_c \\ t_{FR} - t_c \\ t_f - t_d \\ (t_c - t_0) - t_{FR,min} \\ (t_d - t_a) - t_{stay,min} \\ t_{FR,max} - (t_{FR} - t_0) \\ -\mathbf{r}(t_{FR}) \cdot \mathbf{v}(t_{FR}) \\ -\mathbf{r}(t_f) \cdot \mathbf{v}(t_f) \end{bmatrix}_{9\times 1} \geq \mathbf{0} \qquad \mathbf{c} = \begin{bmatrix} \mathbf{r}^{FWD}(t_c) - \mathbf{r}^{BWD}(t_c) \\ \mathbf{v}^{FWD-}(t_c) - \mathbf{v}^{BWD}(t_c) \\ \mathbf{r}(t_a) - \mathbf{r}_a(t_a) \\ \mathbf{r}(t_d) - \mathbf{r}_a(t_d) \\ \cos(\gamma_0) - \cos(0^\circ) \\ \cos(\gamma_{FR}) - \cos(\gamma_{entry}) \\ \cos(\gamma_f) - \cos(\gamma_{entry}) \end{bmatrix}_{15\times 1} = \mathbf{0} \quad (4.2)$$

Note that in Eq. (4.2), the cosine of the flight path angle is used in the equality constraints to facilitate calculation of the analytical gradients (described

in the following subsection). The quadrant ambiguity introduced by the cosine is resolved by the last two inequality constraints. Also note that the angles λ and ϕ in the parameter vector represent angles of right ascension and declination, which are angular components of the position at the specified times measured with respect to the ecliptic plane and Sun-Earth line.

The cost function, given in Eq. (4.3), minimizes the sum of the magnitude of the changes in velocity on the nominal mission path. The initial change in speed (Δv_0) is defined as the difference between the magnitude of the initial velocity vector and the velocity for the initial circular low-Earth parking orbit at 400 km altitude. The change in speed at asteroid arrival (Δv_a) and departure (Δv_d) are defined as the norm of the vector difference of the asteroid velocity vector and the spacecraft velocity vector, which are both calculated in the numerical integration. The change in speed to leave the FRT and approach the asteroid (Δv_c) is the norm of the vector quantity $\Delta \mathbf{v}_c$, which is contained in the parameter vector.

$$J = \Delta v_0 + \Delta v_c + \Delta v_a + \Delta v_d \tag{4.3}$$

To aid in convergence of the optimization routine, the parameters, constraints, and cost function are initially scaled to values on the order of unity. After the optimization has converged, the quantities are scaled inversely to obtain the actual (unitized) optimal values. Scaling is performed so that a single scalar convergence tolerance may be applied to the constraints and cost function; the scaling process amounts to a mapping between a normalized unit system and actual unitized parameters and constraints.

4.5.2 Gradients

Gradients of the constraints and cost function with respect to the parameters must be provided to the numerical optimization routine. The method here utilizes "analytical" gradients, which are computed manually and implemented into the algorithm. Calculation of analytical gradients is described in detail in Section 3.3.1.3. The full expression for each necessary partial derivative is given in Appendix C, which includes full analytical gradients of the cost function and constraints with respect to the optimization parameters.

4.6 Optimized results

The initial conditions presented in Section 4.4 are optimized and converged here. The converged trajectories are presented in graphical form, and relevant numerical results are given. All results are produced using the SQP routine `VF13` [4] in Fortran. In all figures in the rotating frame, the Earth is located at the origin, with the Sun located at 1 AU in the $-x$ direction. The spacecraft departs from Earth on an FRT, and departs from the FRT to approach the asteroid. If the spacecraft were to continue on the FRT, it would return to Earth. For the nominal mission path, the spacecraft performs rendezvous with the asteroid, and returns to Earth after a brief stay at the asteroid.

The reader should note that the results presented here represent locally optimal solutions; that is, the solution is one of potentially many feasible solutions that may also be considered locally optimal. These results are representative of the types of optimal trajectories that may be found for NEA rendezvous using FRTs,

and should not necessarily be seen as the globally optimal solutions. With that stated, the algorithm up to this point has been designed to deliver an initial guess that represents a low Δv nominal mission, and the Lambert trajectory search described in Section 4.2.1 serves as an approximation to a global minimum search for the FRT-to-NEA segment of the nominal mission.

4.6.1 2000 SG344

Converged results for rendezvous with 2000 SG344 are given in Table 4.1. The spacecraft departs Earth on 2027 April 05. If an abort is necessary, the FRT returns the spacecraft to Earth on 2028 March 29. With no abort scenario, the spacecraft performs a maneuver on 2027 October 11. Nine months later, asteroid arrival occurs on 2028 July 19. The spacecraft stays at the asteroid for longer than the required ten day period, and departs on 2028 August 26. In the nominal mission, Earth return occurs on 2029 January 27, approximately 21 months after launch and five months after asteroid departure.

Figure 4.5 shows the converged trajectory in the Earth-centered rotating frame. Figure 4.6 shows the trajectory in the heliocentric inertial frame, where the asteroid and the Earth are omitted in the latter for clarity. The distance of both the spacecraft and the asteroid from Earth over the mission timeline is shown in Figure 4.7.

The Δv for the nominal mission is quite feasible, at 4.431 km/s. The largest maneuver is 3.351 km/s to depart the parking orbit at Earth.

Table 4.1: Converged results for 2000 SG344 rendezvous

Parameter	Optimal value
t_0 (JD)	2461500.7729 (2027 April 05)
t_c (JD)	2461690.2731 (2027 October 11)
t_a (JD)	2461971.6370 (2028 July 19)
t_d (JD)	2462010.1192 (2028 August 26)
t_{FR} (JD)	2461860.4917 (2028 March 29)
t_f (JD)	2462163.8541 (2029 January 27)
Δv_0 (km/s)	3.351
Δv_c (km/s)	0.258
Δv_a (km/s)	0.143
Δv_d (km/s)	0.679
J (total Δv) (km/s)	**4.431**

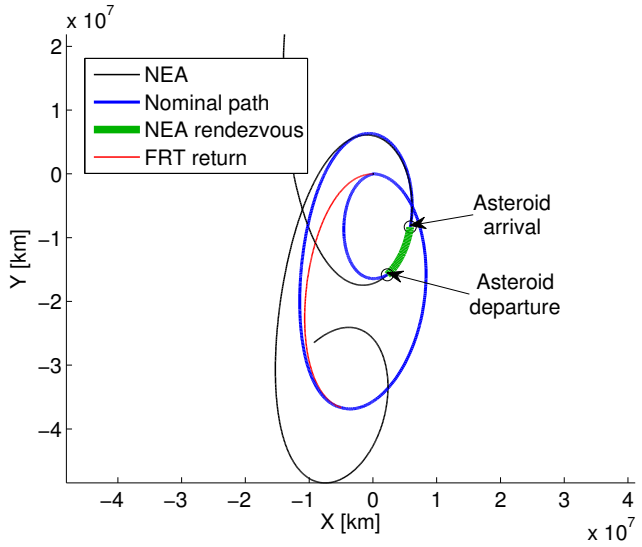

Figure 4.5: Converged rendezvous, 2000 SG344, Earth-centered rotating

4.6.2 2006 BZ147

Converged results for rendezvous with 2006 BZ147 are given in Table 4.2. The spacecraft departs Earth on 2037 August 02. If an abort is necessary, the FRT

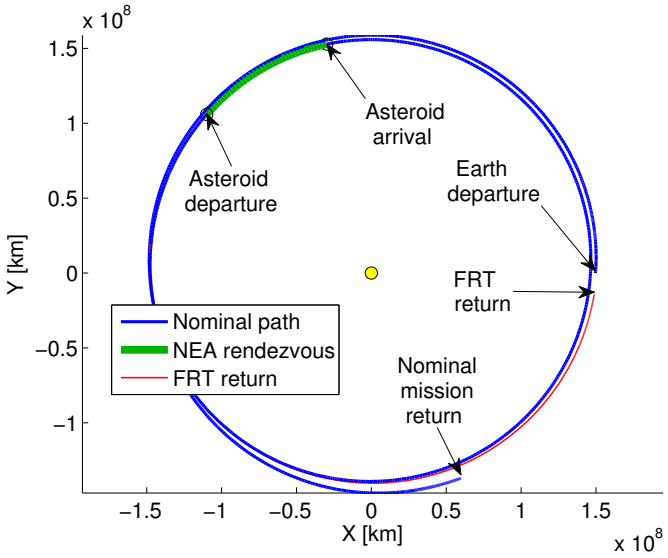

Figure 4.6: Converged rendezvous, 2000 SG344, Sun-centered inertial

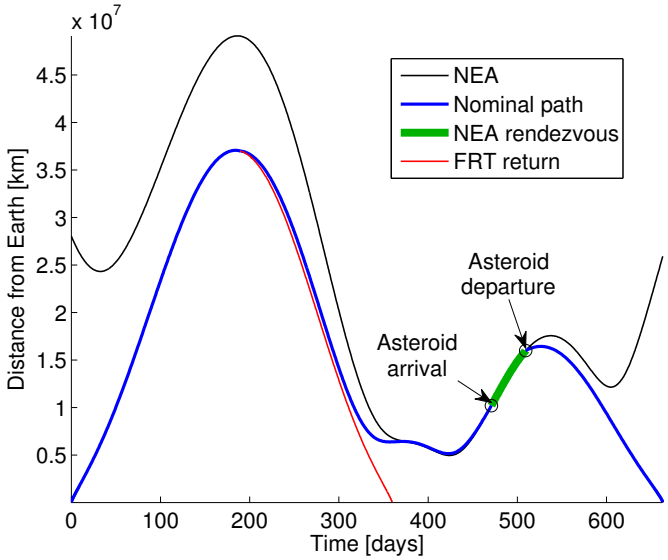

Figure 4.7: Distance from Earth, 2000 SG344

Table 4.2: Converged results for 2006 BZ147 rendezvous

Parameter	Optimal value
t_0 (JD)	2465273.0383 (2037 August 02)
t_c (JD)	2465297.2973 (2037 August 26)
t_a (JD)	2465419.3866 (2037 December 26)
t_d (JD)	2465429.3866 (2038 January 05)
t_{FR} (JD)	2465636.6333 (2038 August 01)
t_f (JD)	2465670.4966 (2038 September 03)
Δv_0 (km/s)	3.617
Δv_c (km/s)	0.595
Δv_a (km/s)	0.195
Δv_d (km/s)	0.608
J **(total** Δv**) (km/s)**	**5.016**

returns the spacecraft to Earth on 2038 August 01. With no abort scenario, the spacecraft performs a maneuver on 2037 August 26. Four months later, asteroid arrival occurs on 2037 December 26. The spacecraft stays at the asteroid for the required ten day period, and departs on 2038 January 05. In the nominal mission, Earth return occurs on 2038 September 03, approximately 13 months after launch and eight months after asteroid departure.

Figure 4.8 shows the converged trajectory in the Earth-centered rotating frame. Figure 4.9 shows the trajectory in the heliocentric inertial frame, where the asteroid and the Earth are omitted in the latter for clarity. The distance of both the spacecraft and the asteroid from Earth over the mission timeline is shown in Figure 4.10.

The Δv for the nominal mission is feasible, at 5.016 km/s. The largest maneuver is 3.617 km/s to depart the parking orbit at Earth.

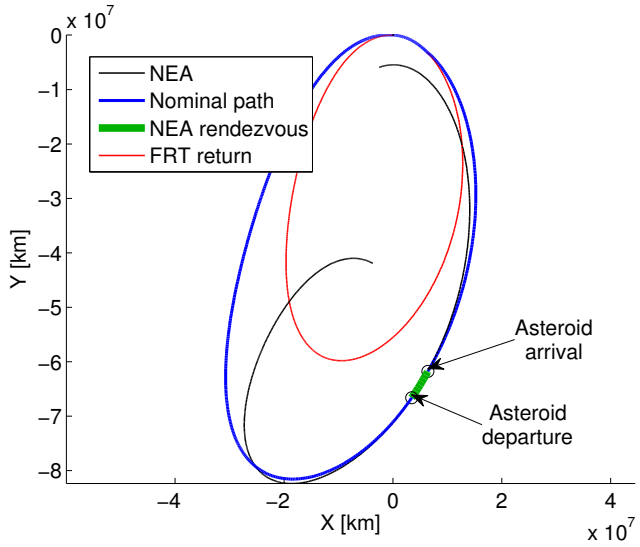

Figure 4.8: Converged rendezvous, 2006 BZ147, Earth-centered rotating

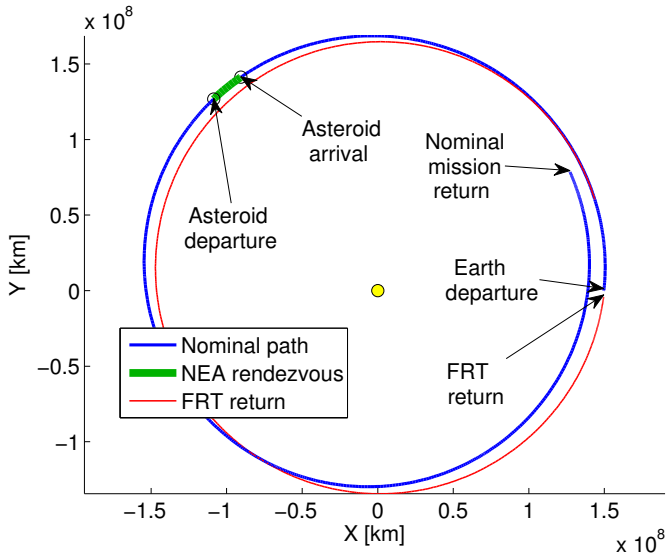

Figure 4.9: Converged rendezvous, 2006 BZ147, Sun-centered inertial

4.6.3 2009 HC

Converged results for rendezvous with 2009 HC are given in Table 4.3. The spacecraft departs Earth on 2025 October 22. If an abort is necessary, the FRT

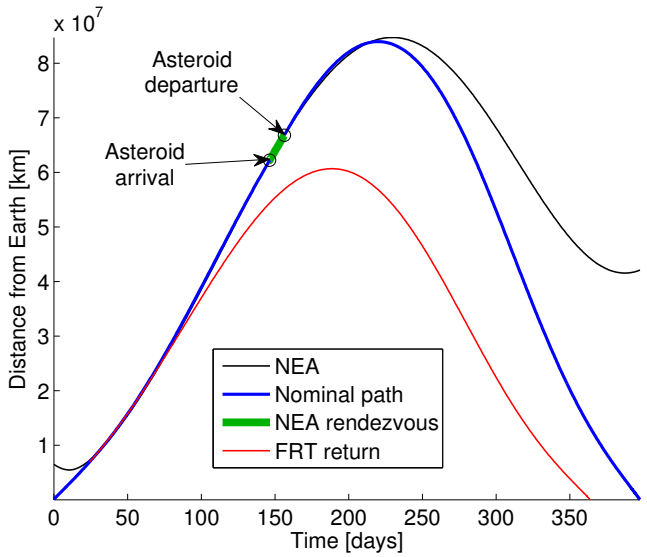

Figure 4.10: Distance from Earth, 2006 BZ147

returns the spacecraft to Earth on 2027 April 05. With no abort scenario, the trajectory actually intersects the orbit of the NEA, and the spacecraft performs a maneuver to both exit the FRT and rendezvous with the NEA on 2026 November 07. The spacecraft stays at the asteroid for the required ten day period, and departs on 2026 November 17. In the nominal mission, Earth return occurs on 2027 April 14, approximately 18 months after launch and five months after asteroid departure.

Figure 4.11 shows the converged trajectory in the Earth-centered rotating frame. Figure 4.12 shows the trajectory in the heliocentric inertial frame, where the asteroid and the Earth are omitted in the latter for clarity. The distance of both the spacecraft and the asteroid from Earth over the mission timeline is shown in Figure 4.13.

Table 4.3: Converged results for 2009 HC rendezvous

Parameter	Optimal value
t_0 (JD)	2460970.6370 (2025 October 22)
t_c (JD)	2461352.1554 (2026 November 07)
t_a (JD)	2461352.1554 (2026 November 07)
t_d (JD)	2461362.1554 (2026 November 17)
t_{FR} (JD)	2461501.4257 (2027 April 05)
t_f (JD)	2461509.8735 (2027 April 14)
Δv_0 (km/s)	4.069
Δv_c (km/s)	2.106
Δv_a (km/s)	1.321
Δv_d (km/s)	0.523
J **(total** Δv**) (km/s)**	**6.699**

The Δv for the nominal mission is 6.699 km/s. The largest maneuver is 4.069 km/s to depart the parking orbit at Earth.

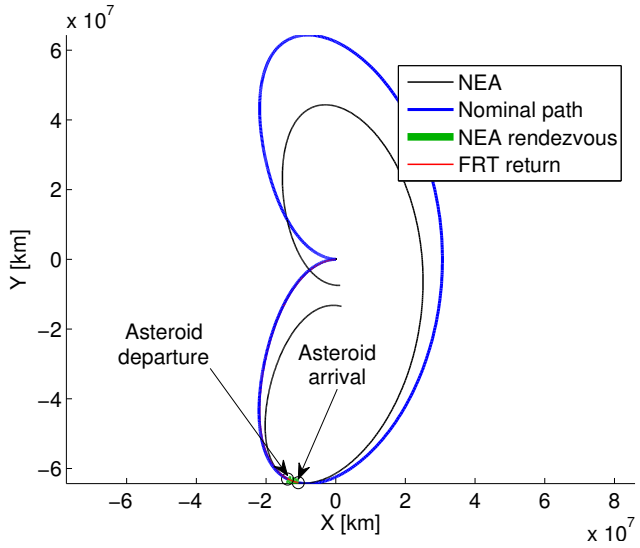

Figure 4.11: Converged rendezvous, 2009 HC, Earth-centered rotating

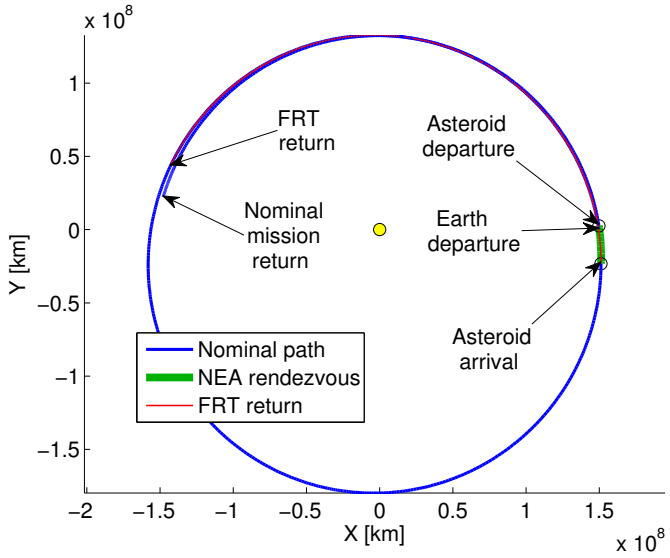

Figure 4.12: Converged rendezvous, 2009 HC, Sun-centered inertial

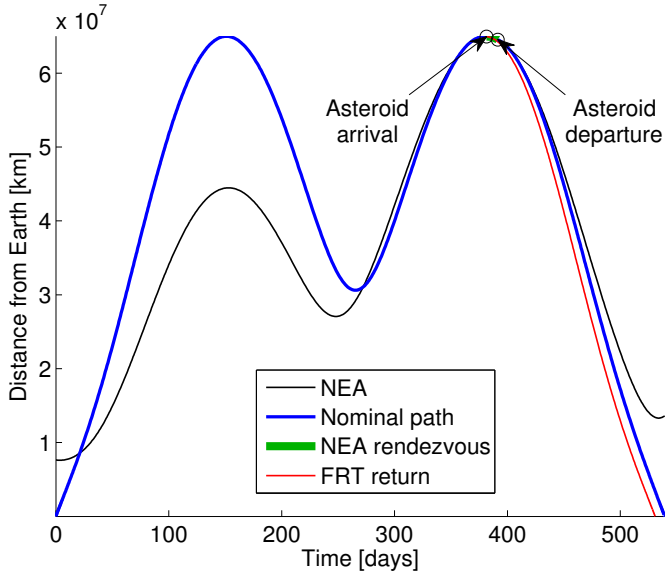

Figure 4.13: Distance from Earth, 2009 HC

Table 4.4: Converged results for 2001 FR85 rendezvous

Parameter	Optimal value
t_0 (JD)	2465695.2503 (2038 September 28)
t_c (JD)	2465709.2503 (2038 October 12)
t_a (JD)	2465865.2250 (2039 March 17)
t_d (JD)	2465875.2250 (2039 March 27)
t_{FR} (JD)	2465874.4034 (2039 March 26)
t_f (JD)	2466233.6383 (2040 March 20)
Δv_0 (km/s)	3.427
Δv_c (km/s)	0.548
Δv_a (km/s)	1.429
Δv_d (km/s)	1.554
J **(total** Δv**) (km/s)**	**6.958**

4.6.4 2001 FR85

Converged results for rendezvous with 2001 FR85 are given in Table 4.4. The spacecraft departs Earth on 2038 September 28. If an abort is necessary, the FRT returns the spacecraft to Earth on 2039 March 26. With no abort scenario, the spacecraft performs a maneuver on 2038 October 12. Five months later, asteroid arrival occurs on 2039 March 17. The spacecraft stays at the asteroid for the required ten day period, and departs on 2039 March 27. In the nominal mission, Earth return occurs on 2040 March 20, approximately two years after launch and one year after asteroid departure.

Figure 4.14 shows the converged trajectory in the Earth-centered rotating frame. Figure 4.15 shows the trajectory in the heliocentric inertial frame, where the asteroid and the Earth are omitted in the latter for clarity. The distance of both the

spacecraft and the asteroid from Earth over the mission timeline is shown in Figure 4.16.

The Δv for the nominal mission is 6.958 km/s. The largest maneuver is 3.427 km/s to depart the parking orbit at Earth.

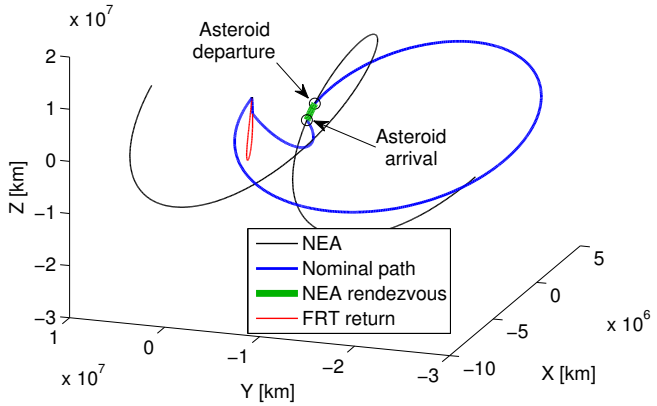

Figure 4.14: Converged rendezvous, 2001 FR85, Earth-centered rotating, unequal axes

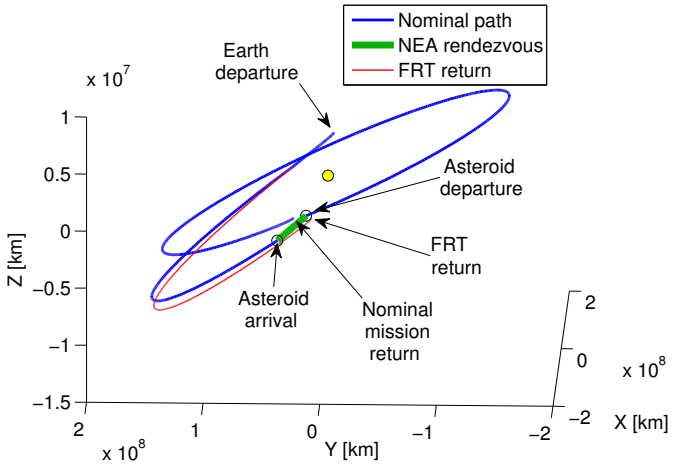

Figure 4.15: Converged rendezvous, 2001 FR85, Sun-centered inertial

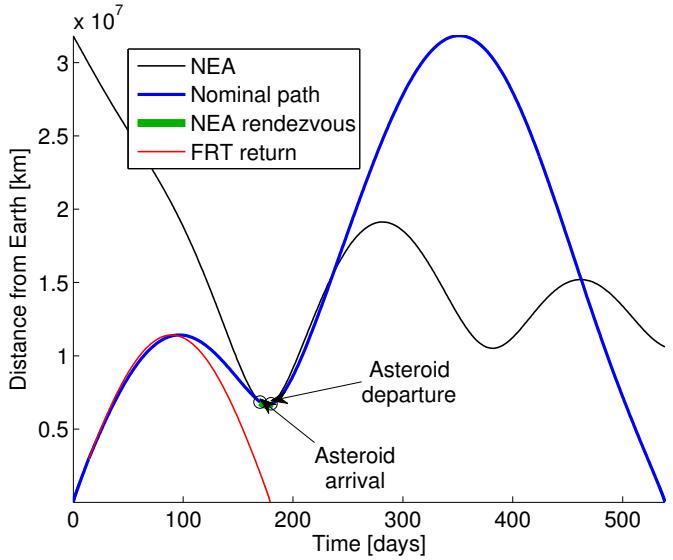

Figure 4.16: Distance from Earth, 2001 FR85

4.6.5 2012 UV136

Converged results for rendezvous with 2012 UV136 are given in Table 4.5. The spacecraft departs Earth on 2021 May 07. If an abort is necessary, the FRT returns

Table 4.5: Converged results for 2012 UV136 rendezvous

Parameter	Optimal value
t_0 (JD)	2459342.1328 (2021 May 07)
t_c (JD)	2459356.1328 (2021 May 21)
t_a (JD)	2459486.3134 (2021 September 28)
t_d (JD)	2459496.3134 (2021 October 08)
t_{FR} (JD)	2459706.2477 (2022 May 06)
t_f (JD)	2459713.0475 (2022 May 13)
Δv_0 (km/s)	3.760
Δv_c (km/s)	0.681
Δv_a (km/s)	0.655
Δv_d (km/s)	0.488
J **(total** Δv**) (km/s)**	**5.584**

the spacecraft to Earth on 2022 May 06. With no abort scenario, the spacecraft performs a maneuver on 2021 May 21, at the minimum of the two-week constraint. Four months later, asteroid arrival occurs on 2021 September 28. The spacecraft stays at the asteroid for the required ten day period, and departs on 2021 October 08. In the nominal mission, Earth return occurs on 2022 May 13, approximately one year after launch and seven months after asteroid departure.

Figure 4.17 shows the converged trajectory in the Earth-centered rotating frame. Figure 4.18 shows the trajectory in the heliocentric inertial frame, where the asteroid and the Earth are omitted in the latter for clarity. The distance of both the spacecraft and the asteroid from Earth over the mission timeline is shown in Figure 4.19.

The Δv for the nominal mission is feasible, at 5.584 km/s. The largest maneuver is 3.760 km/s to depart the parking orbit at Earth.

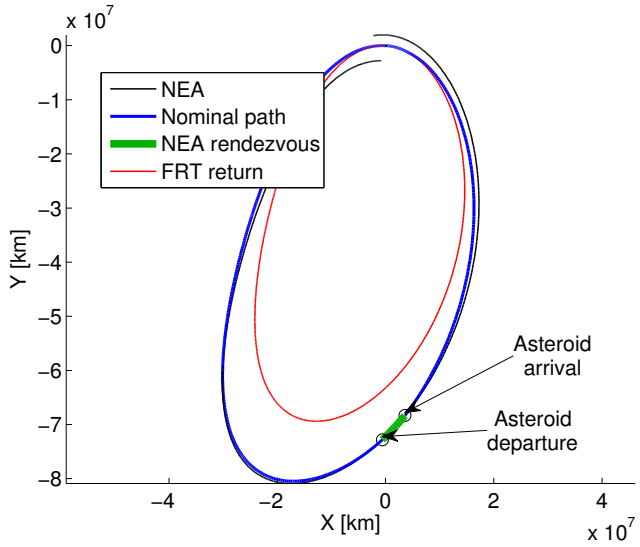

Figure 4.17: Converged rendezvous, 2012 UV136, Earth-centered rotating

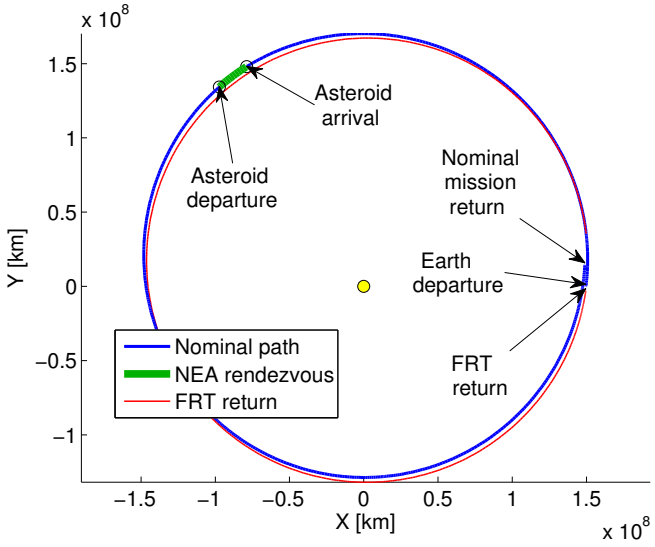

Figure 4.18: Converged rendezvous, 2012 UV136, Sun-centered inertial

4.7 Discussion

The results presented in the previous section exhibit the type of trajectories that may be found by incorporating FRTs into asteroid mission design. The Δv

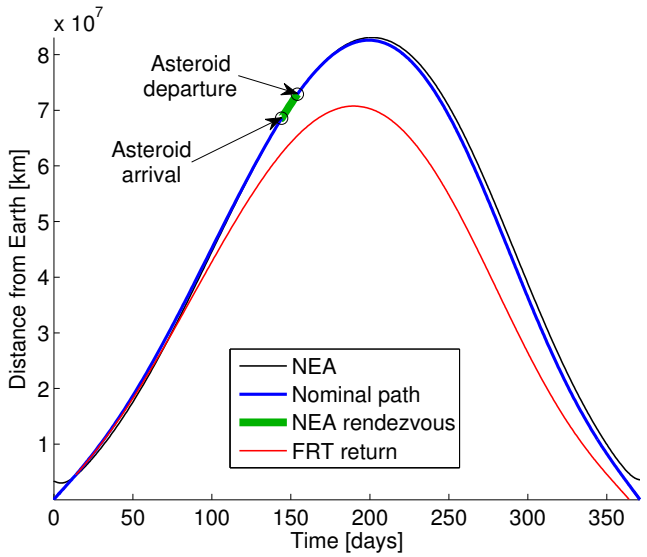

Figure 4.19: Distance from Earth, 2012 UV136

Table 4.6: Summary of round-trip mission parameters using FRTs

	Δv (km/s)	T (days)	Launch date
2000 SG344	4.431	663.1	2027 Apr 05
2006 BZ147	5.016	397.5	2037 Aug 02
2009 HC	6.699	539.2	2025 Oct 22
2001 FR85	6.958	538.4	2038 Sep 28
2012 UV136	5.584	370.9	2021 May 07

values for the rendezvous examples are achievable. A comparison with the Δv values found in the NHATS study provides context for the values achieved with this method. Tables 4.6 summarizes the best-case low Δv value found using an FRT, and Table 4.7 shows the same values found by the idealized NHATS study.

In some cases, the converged values for FRT rendezvous are 1-2 km/s greater than the NHATS-achieved value. This extra cost may be offset qualitatively by considering that the safety of an FRT is implemented in the mission design. However,

Table 4.7: Summary of round-trip mission parameters from NHATS

	Δv (km/s)	T (days)	Launch date
2000 SG344	3.556	354	2028 Apr 22
2006 BZ147	4.184	354	2035 Feb 21
2009 HC	4.504	354	2026 Apr 25
2001 FR85	4.557	354	2039 Oct 06
2012 UV136	5.054	354	2020 May 18

it must also be remembered that the FRT solutions represent local optima, and other solutions can and do exist. Other solutions with different parameters and constraints may yield results that are closer to the idealized Lambert solutions obtained in the NHATS study.

In all example solutions, the largest Δv magnitude occurs when leaving the initial parking orbit. In actual implementation, this impulse could be provided by a booster engine from the launch vehicle, and the spacecraft itself would not be required to provide the fuel for the velocity change. If this impulse is not performed by the spacecraft, the spacecraft itself would need to provide far less Δv authority (as low as 1.080 km/s for the mission to 2000 SG344).

The computed reentry speed of the spacecraft at 200 km altitude for the example missions is given in Table 4.8 for both the FRT return and the nominal mission return. For comparison, the Hayabusa mission visited near-Earth asteroid 25143 Itokawa, and returned on a similar hyperbolic trajectory for Earth reentry. The return capsule had a reentry speed of 12.1 km/s at 200 km altitude, with a relatively steep flight path angle of -12 degrees [100, 117]. As another comparison, the Apollo 4 spacecraft, intended to simulate reentry from a lunar return trajectory,

Table 4.8: Re-entry speed at 200 km altitude

	FRT return (km/s)	Nominal mission (km/s)
2000 SG344	11.2	11.2
2006 BZ147	11.8	11.5
2009 HC	12.0	11.9
2001 FR85	11.2	11.3
2012 UV136	11.9	11.6

had a speed of 11.1 km/s at an altitude of 122 km and a flight path angle of -7 degrees [45].

In the algorithm presented here, it may be desirable to add one or more Δv maneuvers to the optimization cost function to decrease the relative reentry speed for the nominal mission, and thereby decrease thermal and structural stresses to the reentry capsule. This is dependent on heat shield requirements for the specific mission profile desired. However, by comparison with historical missions, the reentry velocities given by the algorithm are within the capabilities of current heat shield technology.

Some mention must be made of the overall mission duration. Although this study is intended to examine the results of orbital dynamics, an actual mission would have to contend with other complications from a long duration manned deep space mission. These difficulties include consumables supply, psychological effects on the crew, and harmful radiation exposure. Much more in-depth study in several disciplines is required to determine what the maximum flight time should be for this type of mission. This determination may be coupled to factors such as advances in

shielding technology to prevent harmful radiation, or improved knowledge of long-term close human confinement.

4.8 Chapter conclusion

Because of the increased attention in the past decade to sending a manned mission to an NEA, it is important to investigate trajectories to these bodies that are not only optimal in a fuel or time sense, but also incorporate aspects of human safety. In this chapter, an algorithm is introduced to systematically search pre-computed FRTs and apply a Lambert targeting routine to automatically generate an initial guess for a full mission to visit an NEA. Subsequently, an optimization algorithm is used to calculate Δv-optimal trajectories to NEAs that incorporate segments that will return a spacecraft to the Earth with no fuel penalty in the case of a catastrophic anomaly, such as an engine failure or total fuel loss. Once on an Earth-return trajectory, the spacecraft may optimally depart after a minimum amount of time to eventually rendezvous with the NEA. After a specified minimum stay time, the spacecraft departs the asteroid and returns to the Earth in a Δv-optimal manner. These missions consist of segments which depart from Earth on an FRT, depart from the trajectory to travel to and rendezvous with the asteroid, and return to Earth on the FRT if no maneuver is applied. This initial guess is delivered to an optimization algorithm to converge a full round-trip nominal mission that satisfies constraints.

Five example missions are presented here, each corresponding to one of the most accessible targets found in the NHATS study. The cost of the missions is

reasonable in terms of total Δv (ranging from 4.4 to 7.0 km/s). This method of calculating optimal trajectories in the CRTBP provides an initial estimate of the Δv penalty for this type of mission, which can be used for further mission planning and model refinement.

The next chapter investigates a method to save on Δv penalty by using a Lunar flyby to enter into the FRT. Although this method introduces risk by performing a gravity flyby soon after launch from Earth, the resulting Δv of the missions is shown to be comparable to the Lambert results from the NHATS study.

Chapter 5

Using the Moon with Free Return Trajectories

5.1 Chapter introduction

The concept of using Free Return Trajectories (FRTs) to travel to Near-Earth Asteroids (NEAs) as a method of risk mitigation was discussed in the previous chapter. Two further aspects of using an FRT to visit an NEA are described in this chapter. First, and most notably, is the use of a Lunar flyby to lower the overall mission Δv cost. Lunar flybys have been used in previous missions [32, 33, 37, 73] and proposed missions or studies [22, 31, 44, 49] to achieve various destinations and mission objectives (note specifically Dunham [31], which gives a trajectory design for a Lunar mapping and NEA flyby mission). By performing a flyby of the Moon on the Earth departure leg, the NEA rendezvous mission shown here achieves a lower cost than would be attainable by simply departing Earth with no flyby. Similar work has been previously presented in Ref. [44] by Hernandez and Barbee, showing how a Lunar flyby may be used to improve fuel cost on a round-trip trajectory to an NEA, but before the work presented here, Lunar flybys had not been previously used to place a spacecraft into an FRT for NEA rendezvous.

Secondly, the current work utilizes full ephemerides for the relevant bodies, and incorporates gravitational forces from the Earth, Moon, and Sun in all phases of

the mission. In the previous chapter, the Circular Restricted Three-Body Problem (CRTBP) was used, assuming that the Earth and Moon constituted a point-mass in a circular orbit around the Sun-Earth barycenter. With the improvement in dynamical model fidelity, the results presented here are more accurate than those previously discussed.

This chapter is organized as follows: The Model section briefly discusses the framework for the problem, but the reader should refer to Chapter 2 for detailed explanation of the equations of motion. The Methods section appears second, and is divided into three subsections. First, the Parameters and constraints subsection introduces the free parameters and related constraints for the problem. Second, the Initial guess subsection details the algorithm developed to provide an initial trajectory guess to the optimization algorithm. Finally, the Optimization subsection provides a description of the high-level algorithm for determining the Δv-optimal trajectory to the selected NEA. The Results section presents an optimal trajectory to asteroid 2000 SG344, as an example of the solutions that may be found by utilizing Lunar flybys to enter into an FRT. The Discussion section provides context for the results, comparing the numerical quantities to results from previous chapters and the NHATS study [2].

The majority of the work in this chapter was presented at the 2013 Astrodynamics Specialist Conference in Hilton Head, SC [12]. The formulation, calculation, and results were obtained in collaboration with Sonia Hernandez, a fellow graduate student in the aerospace program at UT-Austin.

5.2 Model

The problem as posed is to obtain a feasible round-trip trajectory to a target NEA that satisfies the following characteristics:

1. Incorporates a flyby of the Moon to reach the NEA
2. Incorporates an FRT after the Lunar flyby
3. Is locally optimal in a Δv cost sense for the nominal mission path
4. Includes a rendezvous with the NEA for a specified minimum time and returns to Earth on the nominal mission path

The dynamics of the system include the point-mass gravitational influences of the Earth, Moon, and Sun at all times on the trajectory. Eq. (2.4) in Chapter 2 gives the full form of the equations of motion.

Since optimal rendezvous with the target NEA is desired on the nominal mission path, parameters associated with departing the FRT and rendezvousing with the asteroid are incorporated into the optimization scheme. Nominally, the spacecraft departs the FRT, performs a rendezvous with the asteroid for a finite amount of time, and departs for Earth return. The mission scheme is shown in illustrative form in Figure 5.1. Note that the Sun's gravity is part of the system dynamics, even though it is not shown in the figure. Maneuver $\Delta\mathbf{v}_0$ is performed to begin the mission. If an abort is necessary, the spacecraft naturally returns to Earth after Lunar flyby. Nominally, $\Delta\mathbf{v}_c$ is performed to travel to the NEA. Maneuver $\Delta\mathbf{v}_a$ completes the rendezvous, and $\Delta\mathbf{v}_d$ initiates the departure for return to Earth.

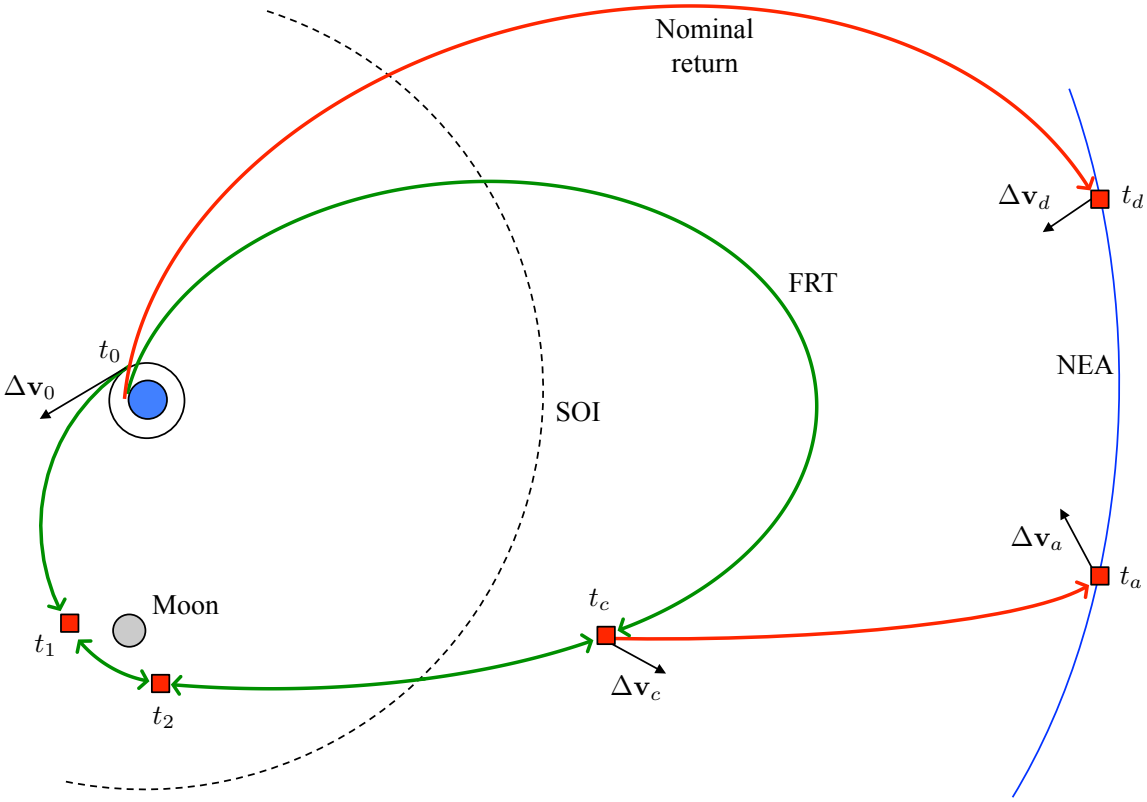

Figure 5.1: Conceptual diagram of Lunar flyby and Δv maneuvers

Also shown in Figure 5.1 are the patch points (red squares), which are described in more detail the Section 5.3. The direction of the arrows indicates direction of integration; e.g., the state at Earth return is integrated backward in time to the patch point at t_c. These patch points are used for optimizing the trajectory using a multiple shooting method. Regardless of integration direction, the converged trajectories are all continuous and smooth in a forward-propagated direction.

The previous chapter focused on the CRTBP to calculate FRTs. In this chapter, the dynamical model uses the full ephemerides for the Earth, the Moon,

and the Sun. This gives a higher fidelity model, even while ignoring minor effects such as asteroid gravity, non-spherical gravitational terms, and non-gravitational forces.

The data for the ephemerides comes from JPL's SPICE toolkit, using the DE421 planetary ephemerides[1].

5.3 Methods

The methods used to construct the problem formulation and develop an initial guess are discussed in this section.

5.3.1 Parameters and constraints

To find an optimal solution, an initial guess algorithm is used to generate a reasonable set of parameters for the optimization algorithm iteration. The optimizer operates on this set of parameters to satisfy equality and inequality constraints while minimizing a performance index. The relevant parameters ($\mathbf{x}_p$), inequality constraints ($\mathbf{d}$), and equality constraints ($\mathbf{c}$) are given in Eq. (5.1). Each vector is initially scaled to values on the order of unity, which is helpful for optimizer convergence.

[1]Data available from JPL at http://naif.jpl.nasa.gov/pub/naif/generic_kernels/spk/planets/. Last accessed 12 August 2014.

$$\mathbf{x}_p = \begin{bmatrix} t_0 \\ t_m \\ t_{SOI} \\ t_c \\ t_a \\ t_d \\ t_{FR} \\ t_f \\ i_0 \\ \Omega_0 \\ \nu_0 \\ \phi_{SOI} \\ \phi_{FR} \\ \phi_f \\ \lambda_{SOI} \\ \lambda_{FR} \\ \lambda_f \\ \mathbf{r}_m \\ \Delta v_0 \\ \mathbf{v}_m \\ \mathbf{v}_{SOI} \\ \Delta \mathbf{v}_c \\ \mathbf{v}_{FR} \\ \mathbf{v}_f \end{bmatrix}_{36\times 1} \qquad \mathbf{d} = \begin{bmatrix} t_0 \\ (t_m - t_0) - 0.5 \text{ days} \\ (t_{SOI} - t_m) - 0.5 \text{ days} \\ t_a - t_c \\ t_{FR} - t_c \\ t_f - t_d \\ (t_c - t_{SOI}) - t_{FR,min} \\ (t_d - t_a) - t_{stay,min} \\ t_{FR,max} - (t_{FR} - t_0) \\ |\mathbf{r}_m| - r_{flyby,min} \\ v_{return,max} - |\mathbf{v}_{FR}| \\ v_{return,max} - |\mathbf{v}_f| \end{bmatrix}_{12\times 1} \geq \mathbf{0}$$

$$\mathbf{c} = \begin{bmatrix} \mathbf{r}(t_1)^+ - \mathbf{r}(t_1)^- \\ \mathbf{r}(t_2)^+ - \mathbf{r}(t_2)^- \\ \mathbf{r}(t_c)^+ - \mathbf{r}(t_c)^- \\ \mathbf{r}_{sc}(t_a) - \mathbf{r}_a(t_a) \\ \mathbf{r}_{sc}(t_d) - \mathbf{r}_a(t_d) \\ \mathbf{v}(t_1)^+ - \mathbf{v}(t_1)^- \\ \mathbf{v}(t_2)^+ - \mathbf{v}(t_2)^- \\ \mathbf{v}(t_c)^+ - \mathbf{v}(t_c)^- \end{bmatrix}_{24\times 1} = \mathbf{0} \tag{5.1}$$

Earth departure occurs at time t_0 from a circular orbit at a specified altitude of 400 km described by the orbital elements i_0 (inclination), Ω_0 (right ascension), and ν_0 (true anomaly from ascending node). A maneuver $\Delta\mathbf{v}_0$ with magnitude Δv_0 is applied in the along-track orbit direction to begin traveling toward the Moon. The trajectory continues to the first patch point at time t_1, which is half a day prior to Lunar flyby. Lunar close approach, or perilune, occurs at time t_m, with position $\mathbf{r}_m$ and velocity $\mathbf{v}_m$ relative to the moon. The time from Earth to perilune and perilune

to the Moon's SOI must be at least half a day. This perilune state continues to the second patch point at time t_2, which is half a day after t_m.

A sphere of influence (SOI) is defined at a distance suitably far away from the Earth-Moon system where the gravitational effects of the Sun begin to dominate those of the Earth-Moon. There are various ways of computing different definitions of the SOI's radius. For purposes of this work, the radius is selected to be 5×10^5 km from Earth's center. The exact definition of a "sphere of influence" is unimportant to the discussion; a suitably far distance for an intermediate state is all that is necessary.

The state associated with SOI passage occurs at time t_{SOI}, with velocity $\mathbf{v}_{SOI}$ and spherical angle components ϕ_{SOI} and λ_{SOI}. This state continues to the third patch point at time t_c, and the spacecraft is required to be on this segment for a certain minimum time $t_{FR,min}$. This time t_c is also the departure time for the nominal mission approach toward the NEA. An impulse $\Delta\mathbf{v}_c$ is applied, and rendezvous occurs at time t_a. The spacecraft must stay with the asteroid for a minimum time $t_{stay,min}$, and departs at time t_d.

Finally, two states are defined at Earth return: one for the FRT, and one for nominal mission return. These consist of the times (t_{FR} and t_f, respectively), latitude/longitude (ϕ_{FR}, λ_{FR} and ϕ_f, λ_f, respectively), and velocities ($\mathbf{v}_{FR}$ and $\mathbf{v}_f$, respectively).

Equality constraints at patch points are denoted as being either before (–) or after (+) the patch point. These patch points are schematically shown as red squares in Figure 5.1.

5.3.2 Initial guess

The optimization algorithm requires a suitable initial guess upon which to operate. This approach uses concepts from two-body orbital mechanics, Lambert targeting, and patched conics to arrive at an appropriate initial guess. A high-level sequence of the initial guess routine is as follows:

1. Target Lunar flyby to enter into FRT
2. Determine favorable NEA rendezvous time
3. Calculate Earth-return leg from NEA

5.3.2.1 Target Lunar flyby

The first segment is the Lunar flyby into the FRT. As discussed in Chapter 3, one family of FRTs consists of resonant single-period orbits that have the same period as the return body. In this case, a Sun-centered two-body orbit beginning at the Earth with a two-body period of one year will return near the Earth in a full dynamical system in approximately one year. In a patched conic sense, this behavior may be approximated by targeting a specific heliocentric departure speed from the Earth-Moon system. In the two-body model, if the spacecraft departing from Earth's position has the same speed as Earth, it will return to the same position after one year, as shown in Eq. (3.1). Therefore, the initial guess algorithm targets a heliocentric spacecraft speed at SOI equal to Earth's heliocentric speed. Because this is an initial guess routine, the exact heliocentric speed of the Earth-Moon barycenter does not need to be used, as the goal of the routine is to find a solution that is suitable

for the optimizer. Although other types of FRTs may be used, the single-year FRTs offer the shortest time of flight with a trajectory close to the ecliptic plane, where many NEAs orbit. A half-year FRT is typically too far above or below the ecliptic plane, and n-revolution FRTs offer less risk reduction to manned missions since their times of flight are often prohibitively long. Because of these reasons, an FRT with a period of approximately one year is assumed in this chapter.

The algorithm first calculates a two-body Earth-centered Lambert-targeted trajectory from low-Earth orbit to the Moon. With the arrival conditions at the Moon, a patched conic approach is taken to determine the post-flyby conditions corresponding to a choice of certain free parameters (described in detail below). The post-flyby state is propagated using Kepler's equation to the SOI, where the heliocentric speed is determined. The free parameters at Lunar flyby are adjusted so that this speed corresponds to an FRT with a return period of one year. The algorithm used to determine the post-flyby conditions and Moon-centric close approach state is described in detail in Appendix D.

For the targeting routine, six free parameters ($\mathbf{p}$) are varied to target the single constraint (c) of heliocentric speed at SOI. Departure latitude and longitude around the Earth (ϕ_0, λ_0), time of flight to the Moon (TOF), Moon-centric latitude and longitude (ϕ_m, λ_m), and initial epoch (t_0) are all varied. These quantities are consolidated in Eq. (5.2). Figure 5.2 gives a graphical representation of the free parameters and the constraint locations.

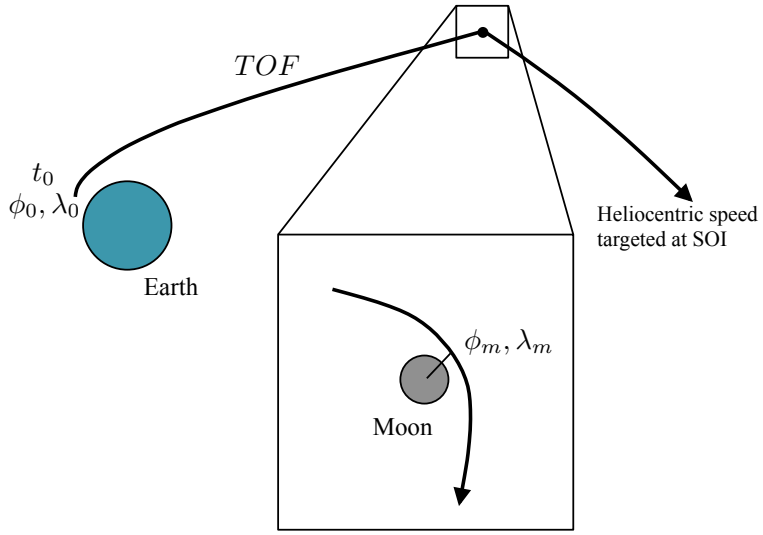

Figure 5.2: Conceptual diagram of target parameters for Lunar flyby

$$\mathbf{p} = \begin{bmatrix} \phi_0 \\ \lambda_0 \\ TOF \\ \phi_m \\ \lambda_m \\ t_0 \end{bmatrix}_{6\times 1} \qquad c = |\mathbf{v}_{SOI}| - |\mathbf{v}_{Earth}| = 0 \tag{5.2}$$

The initial guess up to this point includes Earth departure, Lunar flyby, and an approximation of the FRT path to return to Earth. After the Earth departure and Lunar flyby states have been calculated, the solution represents an initial guess to all segments of the full system except those involving asteroid rendezvous and departure.

In an effort to develop a more robust initial guess routine for the Lunar flyby segment of the trajectory, a continuation/homotopy method was developed for general planetary and Lunar flyby problems. The work that resulted from this method

is presented in Chapter 6, and is applied to problems of interplanetary and inter-moon transfers in a full dynamical model with actual body masses and ephemerides. Future work will involve applying the continuation method to constructing an initial guess for the Lunar flyby problem; the method presented here is one of many possible approaches for constructing an initial guess for this specific problem.

5.3.2.2 NEA rendezvous

To obtain an initial guess for asteroid rendezvous, it is important to choose a reference epoch that contains reasonable relative positioning of the asteroid and Earth around the Sun. To find times of favorable geometries, the results from the NHATS study [2] are utilized. By selecting a specific target NEA, a viable rendezvous epoch may be obtained by searching for a time period with a low relative total Δv to rendezvous with the body in a heliocentric two-body sense. This epoch represents a time with favorable geometries for Earth-to-NEA missions.

A method to calculate the parameters for FRT departure for NEA rendezvous is discussed in Section 4.2, and the FRT departure time (t_c) and departure maneuver ($\Delta \mathbf{v}_c$) values may be estimated from this procedure for initial guess purposes.

5.3.2.3 Earth return leg

Once a reasonable rendezvous and departure time are found, the final portion of the initial guess algorithm uses a heliocentric Lambert-targeting scheme and a differential correction method to calculate the return to Earth. The Lambert targeter calculates the velocities necessary to travel from the NEA to a massless Earth in a

Sun-centered two-body system. The state obtained from this step is then numerically propagated in a full gravitational model (including the Moon and Earth) from the NEA back to Earth. Since the two-body parameters are propagated in a full model, the trajectory will not reach the desired re-entry constraints at Earth. To correct this error, a differential correction scheme is initiated whereby the x-component of the NEA departure velocity is varied to target a scalar perigee value of 7000 km. This targeting is accomplished using a state transition matrix (STM)-based Newton-Raphson differential correction algorithm.

A Newton-Raphson algorithm seeks to find the zero of a function by utilizing its first derivative calculated at the current non-zero location of the function. By iteratively changing the free parameter, the algorithm finds the zero of a specified scalar function f. The parameter is updated from iterate i to $i+1$ using Eq. (5.3), where x is the free parameter and df/dx is the first derivative of the function with respect to the free parameter.

$$x_{i+1} = x_i - \left[\frac{df}{dx}\right]^{-1} f \tag{5.3}$$

The free parameter of the correction algorithm is the x-component of velocity at asteroid departure, and the function to be zeroed is $f = (|\mathbf{r}_{earth}| - 7000\ km)$. The first derivative of this function with respect to the first component of velocity at the asteroid is related through the STM following Eq. (5.4), where the STM is denoted by $\mathbf{\Phi}$. The subscript indicates the first three rows (1:3) and the fourth column of the matrix, corresponding to the x-component of velocity at the asteroid.

$$\frac{df}{dx} = \frac{d}{dv_i}\left(|\mathbf{r}_{earth}|\right) = \frac{\mathbf{r}_{earth}^{\top}}{|\mathbf{r}_{earth}|}\mathbf{\Phi}_{1:3,4} \tag{5.4}$$

After several iterations of the Newton-Raphson iteration scheme, the error in radius at Earth return decreases to the order of tens of kilometers. At this point, the state at Earth return is used for the corresponding states and times in the end-to-end optimization scheme.

5.3.3 Optimization

The optimization of the parameters from the initial guess algorithm is performed using a sequential quadratic programming algorithm VF13 in Fortran from the Harwell Subroutine Library [4]. This prepackaged algorithm operates on a set of parameters to satisfy a set of inequality and equality constraints. For this specific problem, these quantities are given in Eq. (5.1). The routine also minimizes a scalar cost function J, which is the sum of all the deterministic velocity maneuvers. The cost function is given in Eq (5.5), where Δv_a is the magnitude of the velocity difference of the spacecraft and asteroid upon asteroid arrival, Δv_d is the magnitude of the velocity differences upon departure, and Δv_c is the magnitude of the FRT departure maneuver $\Delta \mathbf{v}_c$.

$$J = \Delta v_0 + \Delta v_c + \Delta v_a + \Delta v_d \tag{5.5}$$

In order, the terms represent the magnitude of the initial impulse to leave Earth (included in the parameter vector), the magnitude of the impulse to leave the

FRT (included in the parameter vector), the magnitude of the difference between the NEA's velocity and the spacecraft velocity at rendezvous, and the magnitude of the difference between the spacecraft's velocity and the NEA's velocity at departure. In all, there are four impulsive maneuvers which comprise the cost function.

The optimization routine requires the gradients of the cost function and constraints with respect to the parameters of the system. All gradients have been calculated analytically, which lead to fast and accurate computation. Note that these "analytical" gradients are dependent on numerically propagating the state transition matrix along with the state of the spacecraft on the trajectory.

To compute the gradients, Eq. (3.13) and Eq. (3.12) are used to relate the differentials of the state $\mathbf{x}$ at any time t_{i+1} to any other time t_i. Given the state and the STM between any two times, the full Jacobian matrix of first order partial derivatives may be obtained for the optimization routine. The accuracy of the Jacobian is limited primarily to the accuracy of the numerical solution of the differential equation given in Eq. (3.12). The full form of the gradients for the cost function and all constraints are found in Appendix E.

Upon convergence, the trajectory is 1) feasible, in that it satisfies all constraints, and 2) locally optimal, in that the cost function is at a local minimum at the converged set of parameters. Of course, there may exist other optima and an overall global optimum. Converging on these other solutions depends on the choice of initial guess and various optimizer settings.

Table 5.1: Optimizer parameters for VF13

Parameter	Value
Cost function convergence tolerance	1.0×10^{-4}
Eq. constraint scaling ($\mathbf{r}$)	1.0×10^{-3}
Eq. constraint scaling ($\mathbf{v}$)	1.0×10^{0}
Ineq. constraint scaling (t_0)	1.0×10^{-6}
Ineq. constraint scaling ($\lvert\mathbf{r}_m\rvert$)	1.0×10^{-4}
Ineq. constraint scaling ($\lvert\mathbf{v}_{FR}\rvert$)	1.0×10^{-3}
Ineq. constraint scaling ($\lvert\mathbf{v}_f\rvert$)	1.0×10^{-3}

5.4 Results

An example result is shown here for NEA 2000 SG344. Relevant optimizer parameters are given in Table 5.1 for the VF13 optimizer for Fortran [4]. It should be noted that the parameters are initially scaled to the order of unity. Scaling of parameters and constraints is important for proper convergence of the optimizer; in this specific case, the optimizer converges if the largest position discrepancy is less than 100 meters and the largest velocity discrepancy is less than 0.1 m/s.

The NEA 2000 SG344 is known to be a highly accessible asteroid, because its orbit is very similar to Earth's orbit around the Sun (see Section 4.3 for further discussion on asteroid destination choice). Because its orbit is so similar to the Earth, a rendezvous mission typically requires a relatively small Δv.

Using the initial guess and optimization algorithms described, a locally optimal fully-continuous solution was found with a total Δv cost of 3.878 km/s from LEO to Earth return on the nominal mission path. The initial LEO orbit is at an altitude of 400 km, which is the same initial altitude used in the NHATS study and

Table 5.2: Converged results for 2000 SG344 rendezvous using Lunar flyby

Parameter	Description	Optimal value
t_0 (JD)	Earth departure date	2461861.095 (30 Mar 2028)
t_m (JD)	Moon close approach date	2461864.419 (03 Apr 2028)
t_c (JD)	FRT departure date	2461879.765 (18 Apr 2028)
t_a (JD)	NEA arrival date	2462027.963 (12 Sep 2028)
t_d (JD)	NEA departure date	2462037.963 (22 Sep 2028)
t_{FR} (JD)	FRT Earth-return date	2462207.311 (11 Mar 2029)
t_f (JD)	Nominal Earth-return date	2462217.409 (22 Mar 2029)
$\|h_m\|$ (km)	Perilune altitude	232.490
Δv_0 (km/s)	Earth departure impulse	3.086
Δv_c (km/s)	FRT departure impulse	0.139
Δv_a (km/s)	NEA arrival impulse	0.368
Δv_d (km/s)	NEA departure impulse	0.284
J	**Total Δv cost**	**3.878 km/s**

in the previous chapter, which allows for direct comparison of overall Δv cost and other mission parameters. Table 5.2 contains the relevant data for the converged mission. The relevant inequality constraint parameters are given in Table 5.3. The minimum perilune radius corresponds to an altitude of 100 km above a spherical Moon of radius 1738 km (see Refs. [98, 109] for Moon radius data). The spacecraft returns to a radius of 7000 km from the Earth's center.

Figure 5.3 shows the full converged set of trajectories in the rotating frame centered at the Earth's center of mass. Figure 5.4 shows a close-up of the behavior in the Earth-Moon vicinity. Note that the trajectory performs an unenforced flyby of the Moon upon nominal return (see Figure 5.6(b)). A time history of the spacecraft's distance from Earth is given in Figure 5.5.

Table 5.3: Inequality constraint parameters

Parameter	Description	Value
$t_{FR,min}$	Min. time to stay on FRT before departing	14.0 days
$t_{stay,min}$	Min. time to stay rendezvoused to NEA	10.0 days
$t_{FR,max}$	Max. time from t_0 to t_{FR}	600.0 days
$r_{flyby,min}$	Min. perilune radius	1838.0 km
$v_{return,max}$	Max. speed at Earth return (7000 km)	11.652 km/s

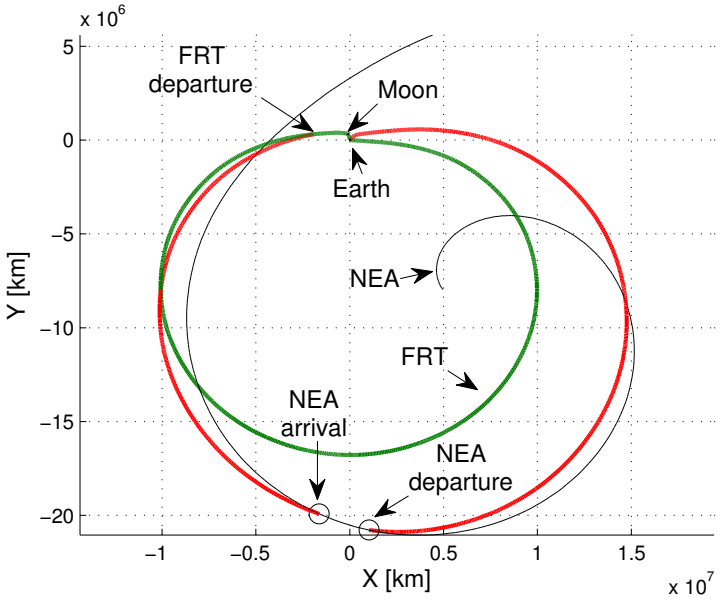

Figure 5.3: Full converged trajectory set to 2000 SG344 in an Earth-centered rotating frame

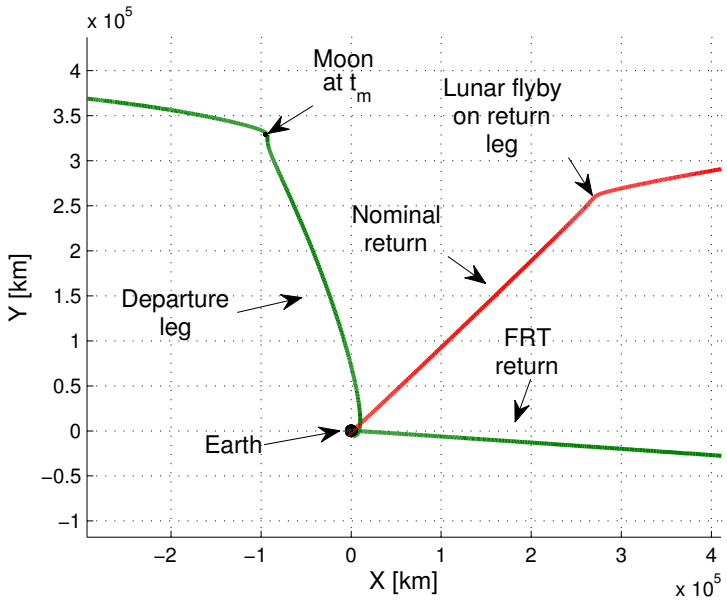

Figure 5.4: Trajectory behavior in the Earth-Moon system

5.5 Discussion

The example trajectory found to rendezvous with NEA 2000 SG344 represents a significant decrease in Δv cost over a solution found with no Lunar flyby in Section 4.6.1. The trajectory found using no Lunar flyby incurred a total cost of 4.431 km/s with the same cost function and no Lunar flyby. The results in this chapter provide a decrease of 553 m/s (12.5%) by utilizing Lunar flybys in a more accurate dynamical system.

Additionally, the risk mitigation factor of using an FRT is preserved, even if some mission risk is added by performing a close flyby of the Moon. Upon departure from the low-Earth parking orbit, the spacecraft follows a ballistic trajectory around the Moon and back to Earth. While small trajectory correction maneuvers would

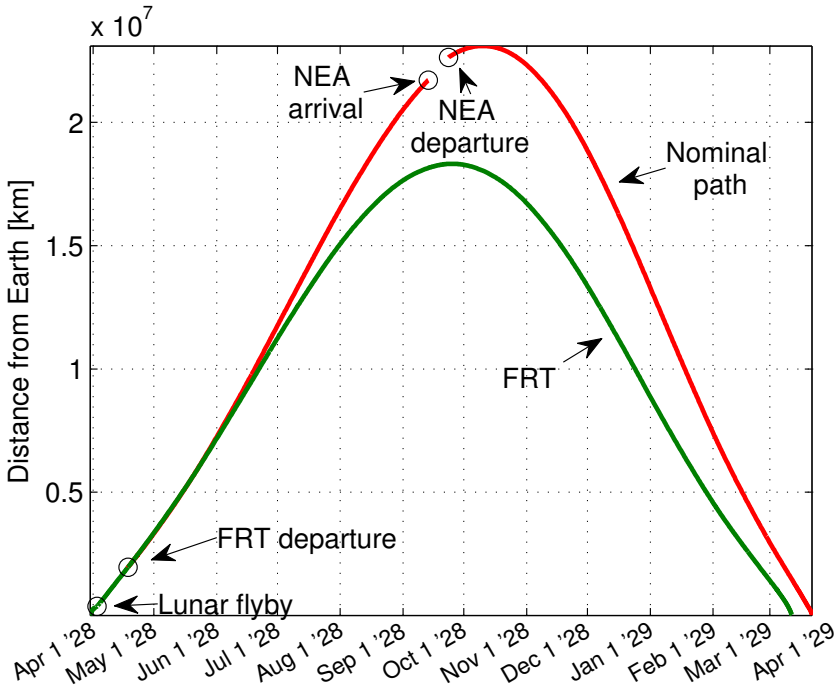

Figure 5.5: Spacecraft distance from Earth for FRT and nominal mission

be necessary on an actual mission to target specific Lunar flyby parameters, the trajectory can be viewed as a ballistic FRT to first order.

As a further point of comparison, the example trajectory may be compared to a round-trip heliocentric two-body trajectory found using the NHATS database [2] (more NHATS results are given in Table 4.6). For 2000 SG344, the study found an overall minimum Δv of 3.556 km/s for a round-trip mission duration of 354 days. The results in this chapter impose an increase of 322 m/s.

It may also be assumed that the initial impulse to depart from low-Earth orbit can come from a launch vehicle's secondary or tertiary motor. Many launch vehicles currently carry the capability to inject a spacecraft on an Earth-departure orbit so that the spacecraft itself is not responsible for carrying the fuel to perform the departure Δv. If this capability is assumed for this example, the spacecraft must only perform a total Δv of 791 m/s, which is quite feasible.

The FRT return and nominal return to Earth satisfy inequality constraints imposed to limit the entry speed into Earth's atmosphere. At a return radius of 7000 km, the spacecraft is constrained to have a speed of no more than 11.652 km/s. In a two-body sense, this corresponds to a speed of 12 km/s at an altitude of 150 km, which represents a common upper limit on Earth re-entry speed. The solution meets the constraint by a comfortable margin, with the FRT return at a speed of 10.710 km/s and the nominal return at a speed of 10.659 km/s, both at 7000 km. The return geometry is shown in Figure 5.6(a), which depicts Earth departure and both return trajectories. Interestingly, the trajectory performs a flyby of the moon on the nominal return leg in addition to the departure leg. The altitude of the return leg

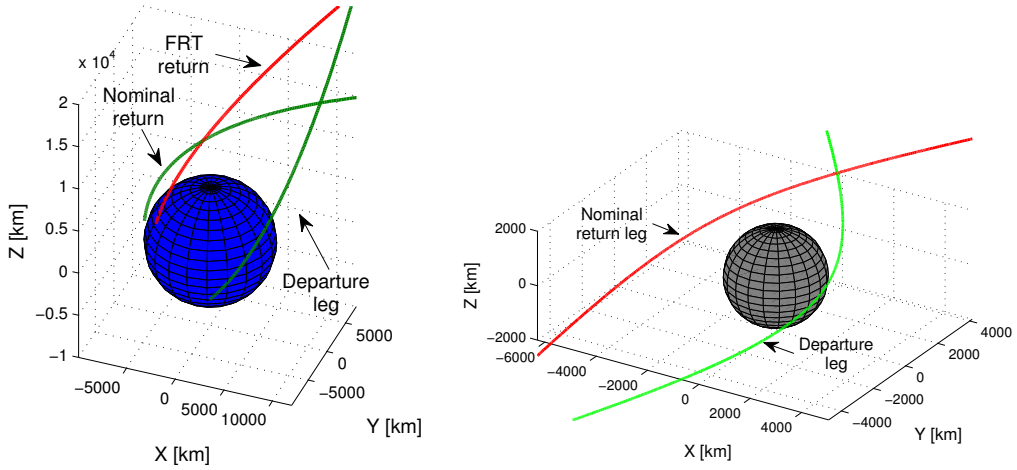

(a) Earth-centric departure and return (J2000 equatorial frame)

(b) Moon-centric flybys

Figure 5.6: Trajectory geometry at Earth and Moon

flyby is 1681.115 km; no inequality constraint monitors the return flyby altitude, since a flyby is not required by the problem structure. Although the observed behavior is not enforced, the return flyby could be utilized to lower the incoming velocity for re-entry on the nominal mission. A Moon-centered figure of the outbound and inbound legs is shown in Figure 5.6(b), depicting the flyby characteristics in a Moon-centered frame.

The converged Lunar flyby geometry on the outbound leg satisfies the inequality constraints imposed. The constraint from Table 5.3 limits the Lunar flyby altitude to 100 km. The final converged trajectory gives a flyby altitude of 232.490 km.

5.6 Chapter conclusion

A method is presented in this chapter to calculate an end-to-end round-trip trajectory to rendezvous with an NEA. This trajectory utilizes FRT capabilities for risk reduction in the event of an abort scenario on a manned spacecraft. To lower Δv cost, the algorithm makes use of a Lunar flyby upon Earth departure to embark upon the FRT. The spacecraft departs the FRT in a Δv-optimal sense, performs rendezvous with the asteroid, and departs from the asteroid to return to Earth. Although a Lunar flyby potentially increases risk due to the navigational challenges introduced to the mission, the Δv savings are appreciable, and the total cost is comparable to the NHATS results. The flyby segment makes the algorithm useful to general interplanetary trajectories that incorporate a Lunar flyby to lower total fuel cost.

An example trajectory is shown with NEA 2000 SG344. The total optimized cost for the mission is 3.878 km/s, which represents an improvement of 12.5% over the result for the same asteroid from Chapter 4. The overall Δv is comparable to the cost of 3.556 km/s found in the NHATS study by using two-body patched conics without free return capabilities. Mission designers must weigh the risk of introducing a Lunar flyby compared to the benefit of lowering the total Δv for this type of mission. The presence of an FRT serves to lower the overall risk of these rendezvous missions in comparison to other simple targeting procedures.

Chapter 6

A Continuation Method to Obtain Full Ephemeris and Full Gravity Model Trajectories

6.1 Chapter introduction

When conducting preliminary mission design, it is common to approximate interplanetary trajectories in low fidelity models that assume simplified system dynamics. Typical assumptions in the preliminary design phase are the patched conics model using two-body dynamics (Section 2.1), or a restricted three-body model (Section 2.2). Trajectories in these reduced models are ideal for rapid searches and fundamental understanding of broad preliminary design spaces. However, simplified models are not sufficient for cases where the model assumptions are invalid, or when a preliminary design moves to a more advanced design stage. For these final design and actual flight stages, a fully-integrated trajectory in the n-body problem (Section 2.3) is needed.

As discussed in Section 1.4.8, most literature on tour design is focused on simplistic models, or missions are designed in higher fidelity models without utilizing the intuitive design space of lower-fidelity problems. The step of transitioning between the two models is often overlooked. Some methods have been introduced

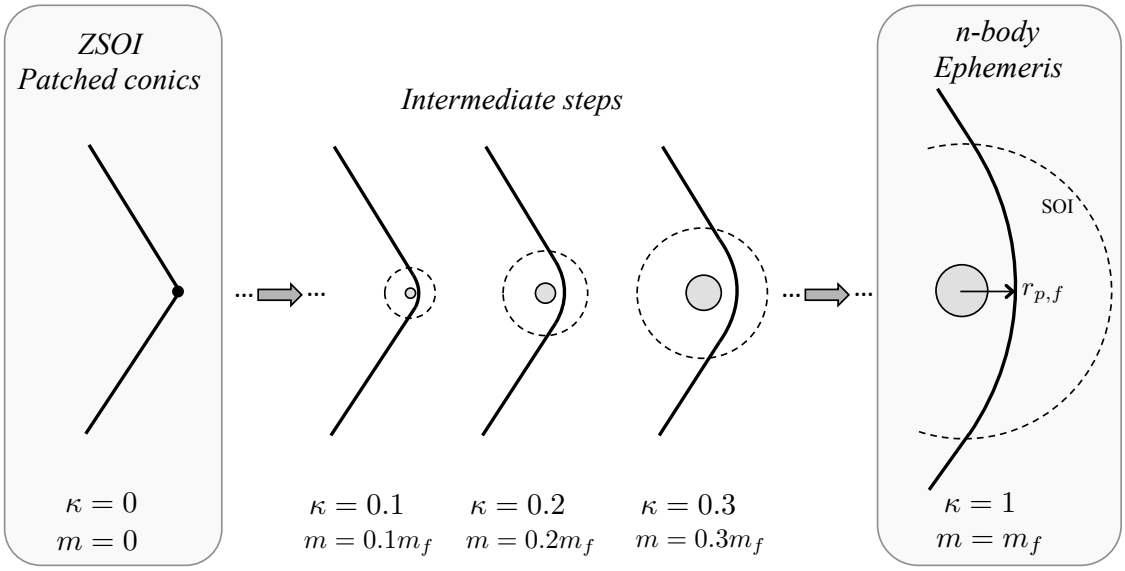

Figure 6.1: Schematic of the continuation method

to address this problem (described in Section 1.4.8), but continuation methods have not yet been applied to this endeavor in the literature.

In this chapter, a method is proposed to take a given low fidelity patched conics trajectory and obtain a ballistic trajectory in an n-body ephemeris with actual body masses. The resultant trajectory is subject to the same constraints as in the simplified problem. The goal is accomplished via continuation on a control parameter $\kappa \in [0, 1]$ that is incremented in steps to represent an increasingly more complex dynamical model. Between each step, the flyby radii, body masses, and sphere of influence sizes are artificially altered such that the turning angles and flyby properties from the previous converged solution are preserved. This preservation is illustrated schematically in Figure 6.1. Additionally, the body ephemerides vary linearly with κ from purely two-body Keplerian ephemerides ($\kappa = 0$) to n-body ephemerides ($\kappa = 1$).

The converged solution at each value of the control parameter is continuous with fully-defined ephemeris states for all bodies, and the transition between ephemerides is smooth. Individual body masses are also tied to the control parameter so that perturbative gravitational effects increase from a two-body to an n-body model. Eventually, at $\kappa = 1$, the driving model coincides with the n-body ephemeris model, and a converged trajectory in this system represents a purely ballistic trajectory that satisfies interior continuity constraints.

As a broad summary of the algorithm in this chapter, there exists an "outer loop," which is comprised of the continuation method and the use of an auxiliary "fake" ephemeris, and an "inner loop," which contains the specific solution method for each step of the continuation. This inner loop may be any solution method to converge feasible or optimal trajectories. In the work performed in this chapter, execution of the inner loop is accomplished by altering the close approach flyby states to satisfy continuity constraints in the common nonlinear programming solver SNOPT [40].

Section 6.3 outlines the overview of the algorithm, and gives a pseudo-algorithm of how to convert a given "zero sphere of influence" (ZSOI) patched conics trajectory into one that is governed by n-body dynamics. The method described in this chapter is applicable to any simplified starting model; the ZSOI model is chosen because it is a common preliminary model for space trajectory designers. The details begin in Section 6.4 by describing the auxiliary Keplerian ephemerides, which is a Keplerian version of the n-body ephemerides for the target bodies. The purpose of the Keplerian ephemerides is to facilitate the definition of a continuous set of "fake"

ephemerides for each intermediate step in the continuation method. The "outer loop" continuation method, which utilizes the feasible solution process at each intermediate step, is developed in Section 6.6. The "inner loop" process of finding a feasible solution using an NLP solver is described in Section 6.7. Two examples are then given: one of an interplanetary Earth-Venus-Venus-Earth-Jupiter ballistic transfer, and one of a seven-encounter tour of three of the Jovian moons. An extension example of patching sequential tours together is given for the seven-encounter Jovian moon tour to extend to a twelve-encounter tour. Finally, some concluding remarks are presented for the chapter. The work presented in this chapter was presented at the Space Flight Mechanics Meeting in Santa Fe, NM [11]; the related paper has been submitted for publication, and is currently under editorial review [10].

6.2 Relation to previous chapters

The contents of this chapter arose out of investigating the Lunar flyby FRT initial guess problem in Section 5.3.2.1. A more robust algorithm with broad applicability was desired to develop the initial trajectory guess for the sensitive Lunar flyby leg. Geometric and patched conic analysis was used to obtain the results in that section, but the topic of a more useful flyby and tour generation algorithm in a full n-body dynamical model developed into the material that is presented here.

The algorithm developed in this chapter is applicable not only to problems like the Lunar flyby FRT, but to any multi-body flyby problem where a basic trajectory model has already been found and a full-ephemeris solution is desired. Especially in tour design and interplanetary transfers, this continuation method may be used to

obtain a fully integrated trajectory from a patched conics trajectory. The interplanetary aspect of this algorithm is applicable to FRT generation for NEA rendezvous, and so is closely related to the methods and results of previous chapters in this dissertation.

6.3 Algorithm Overview

The ultimate goal of the continuation algorithm is to converge a spacecraft trajectory in an n-body dynamical ephemeris (e.g. JPL's SPICE ephemerides[1]), with dynamics governed by bodies of actual mass and size (as opposed to a massless or point-mass assumption). It is assumed that the user has an initial trajectory in a ZSOI model, which can be either in a full ephemeris system or in a simplified ephemeris system.

The "outer loop" of the continuation method operates by conducting a smooth transition between dynamical models and mass assumptions. In this algorithm, parameters of body mass, sphere of influence size, and body ephemerides are varied by the control parameter κ. The goal is to achieve a smooth transition between the starting (simplified) dynamics and the desired final dynamics.

The first step is to create a set of mean Keplerian ephemerides for the desired bodies over the timespan of interest. Next, the initial trajectory (whether it uses "real" ephemerides or some other assumed ephemeris model) is reconverged in the Keplerian ephemerides. These ephemerides closely approximate the final "real"

[1]The SPICE toolkit, data, and documentation may be accessed on-line at: http://naif.jpl.nasa.gov/naif/. Last accessed 12 August 2014.

ephemerides of the bodies, so the transition between these two ZSOI models is accomplished in a relatively simple manner. Finally, with a converged trajectory in the Keplerian ephemerides, the "outer loop" continuation method begins, and the body properties of mass, ephemeris locations, and sphere of influence size are all formally continued until convergence in the final n-body dynamical system is obtained.

These steps are all outlined in Algorithm 2, and described in detail in the subsequent sections.

Algorithm 2 Overview of steps to converge a trajectory in full n-body dynamics

1: **Input:** A desired final ephemeris set
2: **Input:** An initial ZSOI trajectory in some ephemeris model
3: Create a mean Keplerian ephemeris for all bodies over the timespan of interest
4: **if** Initial trajectory ephemerides are not the mean Keplerian ephemerides from Step 3 **then**
5: Perform differential correction on flyby times to converge trajectory using the mean Keplerian ephemerides
6: **end if**
7: Initialize $\kappa_0 < 1$
8: Set a $\Delta\kappa$ appropriate for the problem in question[1]
9: **for** $\kappa = [\kappa_0 : \Delta\kappa : 1]$ **do**
10: Update current guess of flyby states based on κ to preserve flyby parameters
11: Converge trajectory in new dynamics using "inner loop"
12: **end for**
13: **Output:** $\kappa = 1$ converged solution in n-body full ephemeris dynamics

[1]The user may desire $\Delta\kappa$ to change dynamically through the algorithm, and may also desire to use a predictor-corrector step for updating the initial guess.

6.4 The auxiliary ephemerides

The "real" ephemerides represented by an n-body dynamical model are produced in a non-Keplerian framework, and the final resulting spacecraft trajectory is subject to the same dynamical environment. However, if the procedure is to begin with a ZSOI model, the initial guess should be propagated in a corresponding dynamical environment. This dynamical consistency between the forces affecting the spacecraft and the target bodies leads to a smoother targeting or optimization problem, improving robustness and the likelihood of convergence. To achieve such consistency, an auxiliary Keplerian ephemeris is created that is subject to the two-body dynamical assumptions of the ZSOI initial guess trajectory. This Keplerian ephemeris must be chosen to closely approximate the real ephemerides that are governed by the dynamics of the n-body system. Ephemerides at any step in the continuation process are called "fake" ephemerides, and are related to the control parameter κ according to Eq. (6.1), where $\mathbf{x}$ represents the state vector $[\mathbf{r}, \mathbf{v}]^\top$.

$$\mathbf{x}_{fake}(\kappa) = (1 - \kappa)\mathbf{x}_{kepler} + \kappa\mathbf{x}_{real} \tag{6.1}$$

The benefit of this auxiliary ephemeris is clearly seen by examining the trajectory of a spacecraft with respect to a target body. Take, for example, a spacecraft that performs a "backflip" (or half-revolution resonance) trajectory with the Earth, departing Earth at some time and returning half a year later. One may determine the ephemeris state of the Earth in two different ephemeris models: a "real" ephemeris model (e.g. SPICE), and an auxiliary "Keplerian" ephemeris model that is subject

only to heliocentric two-body dynamics. Generating a Keplerian backflip trajectory using boundary conditions of both the real and Keplerian ephemeris models and subtracting the ephemeris position of the Earth with respect to the Sun yields an Earth-centered trajectory in each ephemeris model.

It is expected that a valid backflip trajectory in an Earth-centered inertial frame be smooth, and that it begins and ends at the origin. Only by targeting the Keplerian Earth and performing the origin offset with the Keplerian ephemeris is the expected result realized. Other ephemeris combinations for targeting and offset yield results that do not agree with the expectations. Figure 6.2 shows a grid of trajectories that target the real or Keplerian ephemeris, and perform the origin offset with a real or Keplerian ephemeris. Subfigure (a) is real/real, (b) is real/Keplerian, (c) is Keplerian/real, and (d) is Keplerian/Keplerian.

The wavy nature of subfigure (a) is due to the discrepancy in dynamical models. Because the spacecraft state (propagated in the two-body model) is offset by the real Earth position, the resultant relative position reflects the fact that the real Earth is affected by dynamics that are not taken into account by the Keplerian model. Additionally, the spacecraft does not return to the origin at the final time. Although an origin offset using the Keplerian ephemeris (b) creates a smooth trajectory, the endpoint states of the Earth are still different between the two ephemeris models, and so the spacecraft still does not return to the origin. The real ephemeris offset targeting a Keplerian Earth in (c) suffers from the same problem as in (b): the endpoints are different between the two ephemeris models, and so the spacecraft does not return exactly to the origin. The waviness is also present here as an artifact

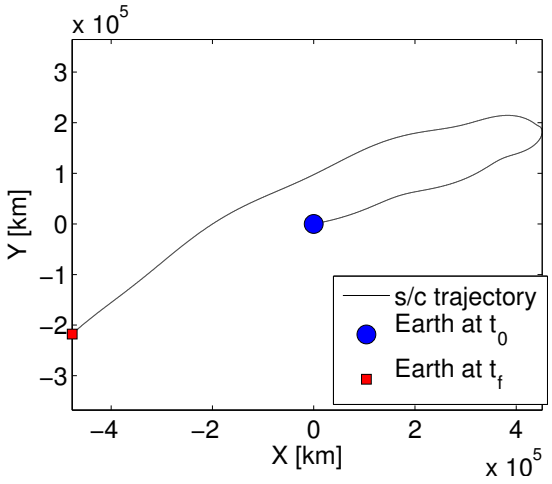

(a) Spacecraft position targeting real Earth ephemerides. Position corrected with real Earth ephemerides

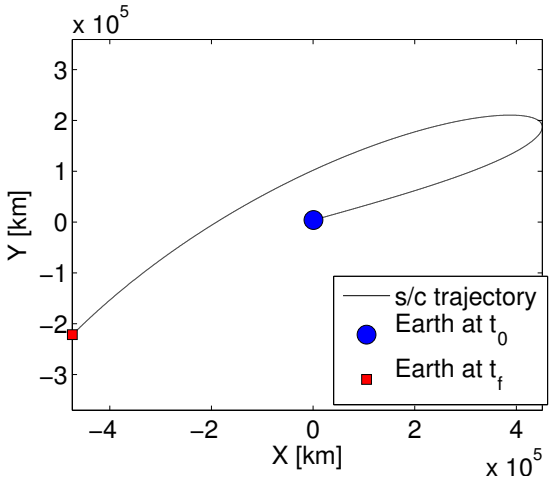

(b) Spacecraft position targeting real Earth ephemerides. Position corrected with Kep. Earth ephemerides

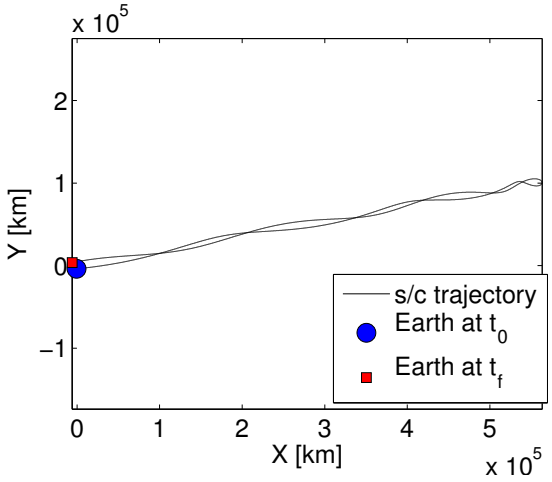

(c) Spacecraft position targeting Kep. Earth ephemerides. Position corrected with real Earth ephemerides

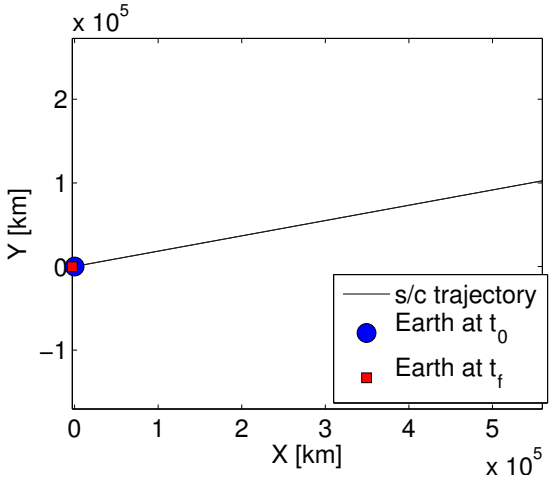

(d) Spacecraft position targeting Kep. Earth ephemerides. Position corrected with Kep. Earth ephemerides

Figure 6.2: Geocentric representation of heliocentric backflip trajectory using Earth positions in different ephemerides for origin offset

of the dynamical model differences between the ephemerides. Only by obtaining the Earth's positions in a Keplerian ephemeris and using that same Keplerian ephemeris to offset the origin to the Earth is the desired result obtained (d). Using only the Keplerian ephemeris yields smooth results, which is desirable for favorable convergence characteristics in gradient-based optimization methods.

A second example showing the benefits of using a mean Keplerian ephemeris is a trajectory that departs Earth and targets the Moon's position in a heliocentric frame with a time of flight of 352 days, so that the trajectory remains close to the Earth. Figure 6.3 shows the results for targeting a real Moon ephemeris. Subfigure (a) shows the origin offset using real ephemerides, and (b) uses the mean Keplerian ephemerides. The wavy nature of the real ephemeris origin offset is clearly seen in this example. These two examples demonstrate that numerical methods applied to space trajectories are more well-behaved when the spacecraft and the gravitating bodies are subject to the same dynamics.

6.4.1 Keplerian ephemeris generation

It is beneficial, therefore, to create an ephemeris that represents the target bodies' states (B) about the central body (A) in the ZSOI model, but that approximates the real n-body ephemerides closely. This ephemeris generation is accomplished in two steps: a geometric generation to obtain a close approximation of the desired trajectory, and a least squares correction to ensure close ephemeris matching.

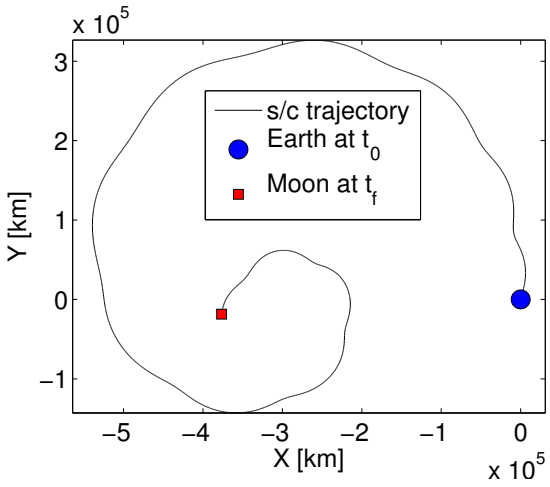

(a) Spacecraft position targeting real Moon ephemerides. Position corrected with real Earth ephemerides

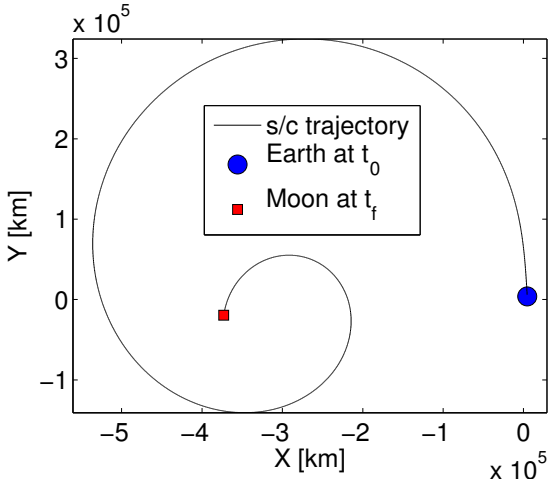

(b) Spacecraft position targeting real Moon ephemerides. Position corrected with Kep. Earth ephemerides

Figure 6.3: Geocentric representation of heliocentric Lunar targeting trajectory using Earth positions in different ephemerides for origin offset

6.4.1.1 Geometric generation

Over a time period of interest, say t_0 to t_f, and at a time interval dt, SPICE is queried to obtain the actual ephemeris state of B with respect to A over the time span. At each queried time, the ephemeris state is converted to Keplerian orbital elements through a standard routine. For n distinct times in the range $[t_0, t_f]$, there are n distinct osculating values for each orbital element (a, e, i, Ω, ω, and ν_0). The goal is to obtain a best fit for a mean element set.

It is especially important to match the mean motion of B about A, and taking the mean of the semimajor axis values will not reliably generate a Keplerian ephemeris that is close enough to the real ephemeris. To obtain a satisfactory value for a, the angular motion of the real ephemeris state of B is accumulated throughout

the time period of interest. At each time step, the angle is calculated between the position vector and and a reference axis in the osculating orbital plane at t_0. At the end of the time period, the mean motion is calculated from the full accumulated angle. The relevant steps are summarized in Algorithm 3.

Algorithm 3 Determining mean motion for the mean Keplerian ephemerides

1: Initialize $m = 0$
2: At t_0, calculate θ_0, the angle between $\mathbf{r}_0$ and the reference axis (the eccentricity vector at t_0).
3: **for all** $t_0 < t \leq t_f$ **do**
4: Calculate θ, the angle between $\mathbf{r}$ and the reference axis.
5: **if** $\theta_{i-1} < \theta_0$ **and** $\theta_i > \theta_0$ **then**
6: Increment $m = m + 1$
7: **end if**
8: **end for**
9: At t_f, calculate the angle α between $\mathbf{r}_0$ and $\mathbf{r}_f$, taking care to account for quadrant issues for the possibility of an angle $\pi < \alpha < 2\pi$.
10: Finally, calculate the full angle traversed over the timespan as $\Theta = 2\pi m + \alpha$.
11: Calculate the mean motion from the full angle traversed using Eq. (6.2).

The mean motion may be obtained as the total traversed angle divided by the total timespan:

$$n_B = \frac{\Theta}{t_f - t_0} \tag{6.2}$$

From this equation, the semimajor axis that best represents the overall mean motion of B about A is found as:

$$a_B = \left[\frac{\mu_A}{n_B^2}\right]^{1/3} \tag{6.3}$$

The next four orbital elements may be reasonably found as the mean of their osculating values throughout the time period. Any error this introduces, especially in Ω and ω, is corrected in the least squares procedure in the following subsection.

$$e_B = \text{mean}(e), \quad i_B = \text{mean}(i), \quad \Omega_B = \text{mean}(\Omega), \quad \omega_B = \text{mean}(\omega) \tag{6.4}$$

Finally, the true anomaly at t_0 must be found to complete the orbital element set, which leads to a completed Keplerian ephemeris. Since all other orbital elements have been defined, there now exists a true perifocal plane which contains the Keplerian orbit. The initial true anomaly, $\nu_{B,0}$, is found as the angle between the projection of $\mathbf{r}_0$ on this perifocal plane and the perifocal frame $+x$ axis, which points toward periapsis.

$$\nu_{B,0} = \cos^{-1}\left(\frac{\mathbf{r}_0 \cdot [1,0,0]^\top}{|\mathbf{r}_0|}\right) \tag{6.5}$$

The result of Eq. (6.5) must be appropriately checked for necessary quadrant corrections.

This algorithm results in the six Keplerian orbital elements which define a Keplerian two-body ephemeris. This result is converted to a Cartesian state at the initial time, and a least squares correction algorithm is applied to this initial state to optimize the match between the real and Keplerian ephemerides.

6.4.1.2 Least squares correction

The initial state $\mathbf{x}_0 = [\mathbf{r}_0, \mathbf{v}_0]^\top$ is iteratively corrected from the geometric guess to minimize the sum of the squares of the distances between the positions of the two ephemerides at equally-spaced times throughout the defined time span of interest. This correction is accomplished by using a batch correction algorithm [106], which is common in estimation problems. In short, the initial state is propagated in the two-body model to the times of interest along with the state transition matrix $\mathbf{\Phi}$. Denoting the real ephemeris values as the "observations" and the propagated states as the "computed" values, an error vector $\mathbf{y}$ is formed at time t:

$$\mathbf{y} = \mathbf{r}_{real}(t) - \mathbf{r}_{kepler}(t) \tag{6.6}$$

By using an iterative least squares correction with $\mathbf{\Phi}$, the elements of the error vector in Eq. (6.6) is minimized at each time step. This process involves iteration on the initial Cartesian state vector $\mathbf{x}_0$, and usually converges in a few steps since the initial guess from the geometric method is close to the least squares solution. In a two-body sense, $\mathbf{x}_0$ is sufficient to characterize the ephemeris, since ephemeris states of a conic section may be obtained by simply propagating the initial state in a two-body model.

6.4.2 Interpolation of the ephemerides

Ephemeris queries in large software packages such as SPICE can be prohibitively slow. To facilitate quick ephemeris calls for the large number of calculations

required in this algorithm, both the SPICE ephemerides and the fake ephemerides are loaded into a spline fitting algorithm [5]. At some time interval dt over the full time span t_0 to t_f, the SPICE state for the target body about the central body is found and loaded into the spline routine, along with the auxiliary Keplerian ephemeris. Spline fitting facilitates quick querying of the state of each target body about the central body for any time during the time span.

6.4.3 Ephemeris comparison

The real and Keplerian ephemerides may be compared by simple vector subtraction of the position throughout the time span of interest. Good ephemeris matching is shown by a constant mean offset of position throughout the time span. The ephemeris matching steps are intended to obtain as close a match as possible, but due to dynamical differences between the models assumed in the two ephemerides, there is a non-zero offset that remains. Figure 6.4 demonstrates the ephemeris comparison for Ganymede and Callisto orbiting about Jupiter. The difference in position of each body in the two ephemerides oscillates over time, but there is no secular growth, indicating that the ephemerides (and, especially, the mean motions) are well-matched.

6.5 Differential correction for v_∞ matching

If the initial ZSOI trajectory is in an ephemeris model other than the mean Keplerian ephemerides created in the previous section, then the trajectory must be re-converged in the new ephemerides (see Algorithm 2). An initial ZSOI trajectory is often constructed using the full n-body ephemerides, or a close approximation

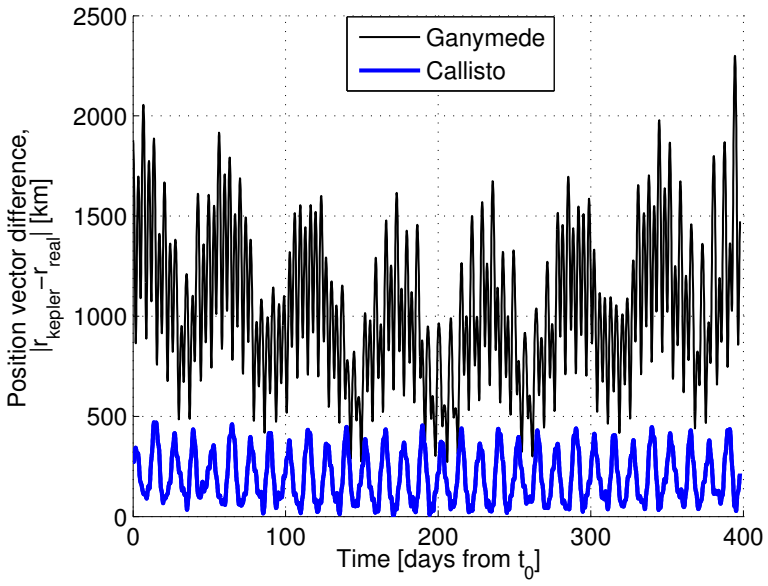

Figure 6.4: Variation in orbital position between the Keplerian and real ephemerides for Ganymede and Callisto

of these ephemerides. Because the Keplerian ephemerides are created to be very close to the full n-body ephemerides, the difference between ZSOI and Keplerian ephemerides is small, and so the trajectory correction is also small.

A simple differential correction scheme is utilized, where the intermediate encounter flyby times are differentially corrected to match interior v_∞ constraints. Matching is accomplished with a Newton-Raphson differential corrector. For n encounters, there are $n-2$ parameters (the flyby times of the intermediate encounters, which does not include the initial and final encounters) and $n-2$ constraints, which are the matching v_∞ parameters at each intermediate encounter. Denote the flyby times as a vector $\mathbf{t}$, and the constraints as a vector $\mathbf{c}$, both of which are $(n-2)\times 1$. To drive $\mathbf{c}$ to zero, the differential correction proceeds iteratively according to Eq. (6.7).

At each step of the correction, the trajectory is re-calculated between each encounter at the specified encounter times using Lambert targeting, which is described extensively in the literature (e.g., see Battin [7] and Vallado [109] for derivations and algorithms) and is summarized in Section 4.2.1.

$$\mathbf{t}_{i+1} = \mathbf{t}_i - \left[\frac{\partial \mathbf{c}}{\partial \mathbf{t}}\right]^{-1} \mathbf{c} \tag{6.7}$$

The correction proceeds until the constraints have all been matched to within a certain tolerance (which is set to 1 m/s in the work in this chapter). In practice, only a few iterations are needed. The matrix $[\partial \mathbf{c}/\partial \mathbf{t}]$ may be found by any partial derivative method. In this chapter, the matrix is calculated via a forward differencing numerical method.

Upon convergence of the Newton-Raphson scheme in Eq. (6.7), the user has a trajectory that is fully converged in a ZSOI mean Keplerian ephemeris system.

6.6 Continuation to n-body dynamics

A continuation method is now introduced to include the effects of an n-body ephemeris model. A control parameter $\kappa \in [0, 1]$ is defined that controls the dynamics and ephemeris model used, with $\kappa = 0$ representing a purely ZSOI Keplerian model and $\kappa = 1$ representing an n-body ephemeris dynamical model. By incrementally increasing this control parameter, feasible solutions are calculated in models that approach the desired n-body dynamics. The continuation problem is posed such

that the ZSOI model is the limit as $\kappa \to 0$, and the initial guess is already converged in this ZSOI model.

The control parameter κ is tied to three important aspects of the model: body ephemerides, body radii, and body masses (which relate to sphere of influence sizes). The ephemeris used for each value of κ is linearly related to the real and Keplerian ephemerides according to Eq. (6.1)[2]. In this manner, the endpoint values of κ (0 and 1) use the two exact ephemerides at the algorithm's disposal (Keplerian and real), and the values in between are obtained via a simple linear weighting function. This approach is similar to the methodology used by Lantoine and Russell for intermoon halo-to-halo transfers [59].

A similar method is employed to vary the radius and mass (and sphere of influence) of each body; this method is depicted in Figure 6.1. In the ZSOI model, each target body is a point mass that instantaneously turns the trajectory. Additionally, it is assumed that the effects of the central body and third bodies are nonexistent for the "instantaneous" flyby of the ZSOI model. Around each target body (TB), the mass of all bodies is varied by κ. Around the central body (CB), the mass of the central body remains constant, while the masses of the target bodies are tied to κ. Eq. (6.8) summarizes the body radii (ρ) and the mass parameter (μ) values at each value of κ for the different regions that the spacecraft traverses.

[2]A more robust way to vary the ephemeris would be to calculate a new auxiliary ephemeris for every value of κ (for example, by numerically propagating body states according to the dynamics at the current value of κ).

$$\mu_{CB} = \begin{cases} \kappa \cdot \mu_{CB,final} & \text{if about target body} \\ \mu_{CB,final} & \text{if about central body} \end{cases}$$

$$\mu_{TB} = \kappa \cdot \mu_{TB,final} \tag{6.8}$$

$$\rho_{TB} = \kappa \cdot \rho_{TB,final}$$

At any iteration in the continuation method, the equations of motion of the spacecraft about the central body are given by Eq. (6.9), where μ_{CB} and μ_{TB} are calculated according to Eq. (6.8). Note that $\mathbf{r}_{TB,i}$ is the i^{th} target body ephemeris position with respect to the central body. These equations of motion are identical to the n-body equations of motion given in Eq. (2.4), but with slightly different vector notation.

$$\ddot{\mathbf{r}} = -\mu_{CB}\frac{\mathbf{r}}{r^3} - \sum_{i=1}^{n} \mu_{TB,i}\left(\frac{\mathbf{r}_{TB,i}}{r_{TB,i}^3} + \frac{\mathbf{r} - \mathbf{r}_{TB,i}}{|\mathbf{r} - \mathbf{r}_{TB,i}|^3}\right) \tag{6.9}$$

Similarly, the equations of motion of the spacecraft about any target body i are given by Eq. (6.10).

$$\begin{aligned} \mathbf{r}_{rel} &= \mathbf{r}_{TB,j} - \mathbf{r}_{TB,i} \\ \ddot{\mathbf{r}} &= -\mu_{TB,i}\frac{\mathbf{r}}{r^3} + \mu_{CB}\left(\frac{\mathbf{r}_{TB,i}}{r_{TB,i}^3} - \frac{\mathbf{r} + \mathbf{r}_{TB,i}}{|\mathbf{r} + \mathbf{r}_{TB,i}|^3}\right) ... \\ &... - \sum_{j=1, j\neq i}^{n} \mu_{TB,j}\left(\frac{\mathbf{r}_{rel}}{|\mathbf{r}_{rel}|^3} + \frac{\mathbf{r} - \mathbf{r}_{rel}}{|\mathbf{r} - \mathbf{r}_{rel}|^3}\right) \end{aligned} \tag{6.10}$$

In the algorithm utilized here, a feasible solution is known for $\kappa = 0$, which is the ZSOI model. Subsequently, κ is iteratively incremented to $\kappa_{i+1} = \kappa_i + \Delta\kappa$, where

$\Delta\kappa$ is a constant step size defined by the user. Alternatively, a predictor-corrector scheme may be implemented to dynamically change the step size, but a constant step size is assumed here. This approach amounts to utilizing the most basic embedding algorithm to walk the parameters incrementally along a solution curve (assumed to be smooth and well-behaved) to the final, desired model [3].

At each step, the converged states from the previous κ value are kept (other than the flyby periapsis states, which are altered to preserve flyby turning angles), and are assumed to represent a reasonable first guess to the feasible solution at the new value of the control parameter. This type of formulation is similar to the continuation methods used in other works to determine families of trajectories [9, 21, 24, 75, 116].

Some care must be taken in how κ is incremented at each step for a fixed $\Delta\kappa$. For a small number of target bodies or for short transfer times, it is best to set $\Delta\kappa$ to relatively large value to save computation time. In fact, for very simple problems (such as single body-to-body transfers with a small flight time), it may be possible to set $\Delta\kappa$ to 1. This scenario represents a case where the ZSOI converged solution is an acceptable guess to the n-body ephemeris model, which is an assumption that is often made by mission designers. The ability to add a control parameter generalizes this practice. Paffenroth, Doedel, and Dichmann [75] provide a concise mathematical and graphical depiction of the notion of the basin of attraction for κ. Large values of $\Delta\kappa$ may lead to a solution in a different family of trajectories, or may prevent the algorithm from converging at all.

6.7 Solving the "Inner Loop" sub-problem

Continuation methods require repeated solutions to a number of "inner loop" subproblems connected via the continuation parameter. This section describes the method to solve the sub-problem at each related iteration. In this solution approach, a multiple shooting method is used to break the trajectory into several segments. Because interbody trajectories often operate in regions with fast-changing dynamics that can greatly alter the final solution of the problem, it is common practice to separate the full trajectory into several segments and converge the solution with intermediate patch points, similar to the patch point methods presented in previous chapters.

6.7.1 Patch points

The patch points are defined by flight times from the close approach time at each encounter. These flight times are intended to occur at the approximate location of the sphere of influence (SOI) of each body.

Define the radius of the sphere of influence as the commonly-used Eq. (6.11). Note that the gravitational parameter μ_B is multiplied by the control parameter κ. The quantity r_{AB} is the distance between the central body and the target body, and the subscripts A and B denote the central and target bodies, respectively.

$$r_{SOI} = r_{AB} \left(\frac{\kappa \mu_B}{\mu_A} \right)^{2/5} \tag{6.11}$$

An estimate for the time of flight from periapsis to the SOI may be found through the true, hyperbolic, and mean anomalies. Denote this fixed time of flight as Δ_{SOI}, which depends only upon the geometry of the hyperbolic flyby and the radius of the SOI.

For flyby encounter i, it is now possible to obtain the SOI patch times with respect to the periapsis flyby time $t_{p,i}$. The patch times are given as t_i^- and t_i^+ in Eq. (6.12).

$$t_i^- = t_{p,i} - \Delta_{SOI} \qquad t_i^+ = t_{p,i} + \Delta_{SOI} \tag{6.12}$$

The patch times are not held constant between continuation steps. Because each new value of κ leads to a change in the target body mass, according to Eq. (6.8), the fixed estimate for the SOI flight time Δ_{SOI} is altered for each target body at each κ subproblem.

6.7.2 Intermediate states

The state of the ZSOI trajectory at the halfway point (in time) between each encounter is used as the intermediate state. A schematic of the patch times with intermediate times for an example of three target bodies is given in Figure 6.5.

For encounter i at t_i and of body $i+1$ at t_{i+1}, the intermediate time is found by Eq. (6.13).

$$t_{inter,i} = \frac{t_i + t_{i+1}}{2} \tag{6.13}$$

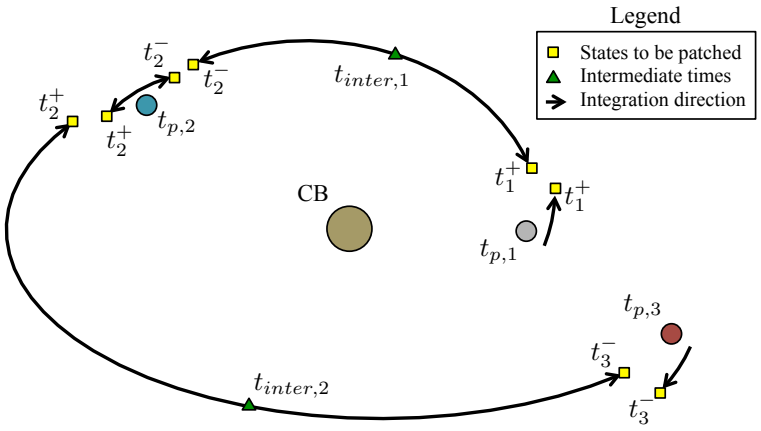

Figure 6.5: Patch states and intermediate times for three target bodies

This time is a fixed parameter for each solution increment, and is not allowed to vary. Recall that the state of the spacecraft $[\mathbf{r}_i, \mathbf{v}_i]^\top$ is known with respect to the central body at each flyby time from the initial Lambert problem solution. This state is simply propagated forward in time from t_i to $t_{inter,i}$ to determine the state $[\mathbf{r}_{inter,i}, \mathbf{v}_{inter,i}]^\top$. For n encounters, there exist $n-1$ intermediate times, each with six defined state elements.

6.7.3 Parameters and constraints

It is now possible to fully define the parameters and constraints used in this approach to the inner loop solution. Qualitatively, the constraints are that the resulting trajectory must be continuous in position and velocity, and that the initial and final states with respect to the terminal bodies represent periapsis states.

The free time parameters are the n flyby periapsis times: $t_{p,1}$, $t_{p,2}$, ... , $t_{p,n}$. The intermediate times are fixed at the midpoint time between body encounters,

found according to Eq. (6.13). Additionally, the patch times are fixed with respect to the body encounter time, according to Eq. (6.12). The encounter times are free, but the time Δ_{SOI} is fixed for each flyby.

The state at each non-terminal encounter n is represented by the state vector given in Eq. (6.14). This specific formulation of the state vector is chosen because the parameters do not vary significantly between steps of the continuation procedure, regardless of the value of $\Delta\kappa$.

$$\mathbf{x}_{p,n} = \begin{bmatrix} r_{p,n}/\rho_{body,n} \\ \alpha_{p,n} \\ \beta_{p,n} \\ v_{\infty,n} \\ \alpha_{vp,n} \\ \beta_{vp,n} \end{bmatrix}_{6\times 1} \tag{6.14}$$

In Eq. (6.14), α_p and β_p are spherical angle parameters for the position vector in the chosen reference frame and α_{vp} and β_{vp} are spherical angle parameters for the periapsis velocity vector. The periapsis speed is computed using two-body dynamics from the value of v_∞. The first quantity in Eq. (6.14) represents the ratio of the flyby periapsis radius to the body radius at each step of the continuation method. This quantity remains nearly constant through the continuation process, since both quantities in the ratio change nearly linearly with the continuation parameter κ.

Since the parameters are expected to remain relatively constant (well-behaved) through the continuation procedure, the use of a constant $\Delta\kappa$ is justified. If the parameters varied significantly (e.g., if $r_{p,n}$ were used instead of $r_{p,n}/\rho_{body,n}$), then a predictor-corrector or pseudo arc-length algorithm would be useful.

The state at the terminal bodies is also given by Eq. (6.14), but since the desired close approach distance at the terminal bodies is user-defined and is scaled linearly by κ at each continuation step, the magnitude of the position at periapsis is not included as a free parameter. Finally, the intermediate states are represented by the position and velocity vectors $[\mathbf{r}_{inter,1}, \mathbf{v}_{inter,1}]^\top$, ... , $[\mathbf{r}_{inter,n-1}, \mathbf{v}_{inter,n-1}]^\top$. These parameters are all free to be varied by the solver.

In all, there are n free time parameters, $6(n-2)$ full periapsis states elements, $6(n-1)$ intermediate state elements, and 10 total terminal body state elements. This yields a total of $13n-8$ state elements. Note that an initial guess must be obtained for the flyby parameters, which may be found by examining the flyby geometry of the velocity vectors from the Lambert targeting routine from the ZSOI solution. This procedure is described in detail in Appendix F.

Constraints are separated into equality and inequality constraints. The equality constraints consist of the patch continuity constraints and the endpoint periapsis constraints, the latter of which are represented by a simple dot product, where $(\mathbf{r}_p \cdot \mathbf{v}_p) = 0$ must be satisfied in the body-centric frame. The position and velocity equality constraints are weighted such that they match to within 1 km and 1 m/s when the feasibility tolerance of the optimizer is met. The inequality constraints ensure that time increases monotonically with each event, and that the periapsis altitudes of the intermediate flybys are above some user-prescribed limit. Note that the body radii, used to calculate flyby altitudes, are defined according to Eq. (6.8).

In all, there are $12(n-2)$ constraints at the non-terminal encounters, 12 total constraints at the terminal bodies, and 2 terminal periapsis constraints, for a total

of $12n - 10$ equality constraints. There are $n - 1$ intermediate times, $n - 1$ flyby times after periapsis, $n - 1$ flyby times before periapsis, n periapsis times, and $n - 2$ flyby altitude constraints for a total of $5n - 5$ inequality constraints. It is worth noting that this problem may easily be cast as an optimization problem rather than a feasibility problem if there is a suitable cost parameter to be minimized.

6.7.4 Gradients

The implementation of this algorithm in this chapter utilizes the well-known large-scale SQP optimization algorithm SNOPT [40] with no objective function to obtain a feasible solution to the trajectory continuity problem. Like many optimization methods, SNOPT requires the gradients of the constraints with respect to the parameters. These gradients are accurately calculated using complex step differentiation, which is a novel method related to finite differencing based on perturbing the state parameters by a small complex term. Details of this highly accurate and relatively fast method may be found in Ref. [65].

6.8 Examples and results

Two examples are presented: an interplanetary transfer from Earth to Jupiter using flybys of Venus and Earth, and a seven-encounter tour of three Jovian moons. A tour extension is presented for the Jovian moon example, demonstrating the chaining of sequential segments together to form longer tours.

6.8.1 Earth-Venus-Venus-Earth-Jupiter (EVVEJ) transfer

An interplanetary example involving five encounters is chosen to demonstrate the utility of the algorithm. An initial ZSOI trajectory is obtained using EXPLORE, a patched conics tour generating program external to this dissertation developed by Demyan Lantukh and Dr. Ryan Russell at UT-Austin. A trajectory tour leaving Earth, flying twice by Venus and once by Earth, and arriving at Jupiter, is chosen as an initial ZSOI tour. This trajectory is sufficiently complex so as to likely benefit from the continuation procedure.

After tuning the continuation parameters, the values $\kappa_0 = 0.05$ and $\Delta\kappa = 0.05$ were found to converge well using the continuation algorithm. For the converged solution, the specified initial and final radii about Earth and Jupiter are $r_{p,f} =$ 10,000 km and $r_{p,f} = 100{,}000$ km, respectively. The converged solution was obtained with a total CPU runtime of 332 seconds (see Section 2.5 for computer platform specifications).

Figure 6.6 shows the final converged trajectory from Earth to Jupiter via two Venus flybys and an Earth flyby, with the orbits of the Venus, Earth, and Jupiter about the Sun shown as thin lines.

It is informative to see how relevant parameters vary throughout the continuation process, and to visualize how the flyby trajectories vary with different values of the control parameter κ. Figure 6.7 shows the variation of independent parameters through the continuation process for the EVVEJ transfer (Note that the horizontal axis in each subfigure is the independent control parameter κ). The parameters

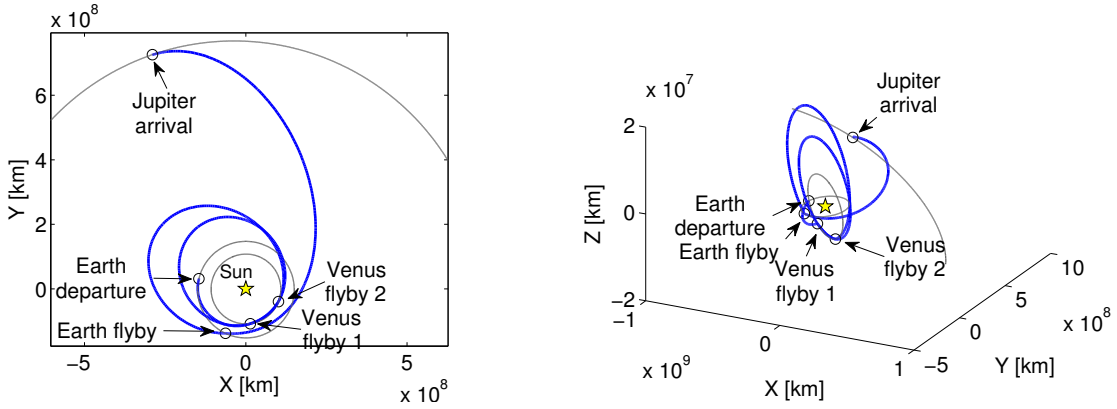

(a) 2D transfer

(b) 3D transfer - axis scaling is unequal

Figure 6.6: Converged EVVEJ transfer.

shown are: time of encounter periapsis (deviation from the initial guess), the v_∞ of each flyby, the position right ascension and declination (α and β), the periapsis radii in terms of flyby body radii, and the periapsis velocity vector heading in right ascension and declination (α_v and β_v).

Other than the encounter time, the parameters are nearly constant through the entire continuation process. The encounter times, while not constant, vary smoothly through each continuation step. Note that although the boundary times of the initial and final encounters may be held constant throughout the continuation process, the Earth departure and Jupiter arrival times are allowed to be free in this scenario. The well-behaved nature of the parameters suggests that the speed of convergence may improve if $\Delta\kappa$ is carefully increased to a higher value. The fact that most parameters are constant suggests that the algorithm may converge directly when $\kappa_0 = 1$, although the variation of the flyby time suggests the necessity of the continuation method.

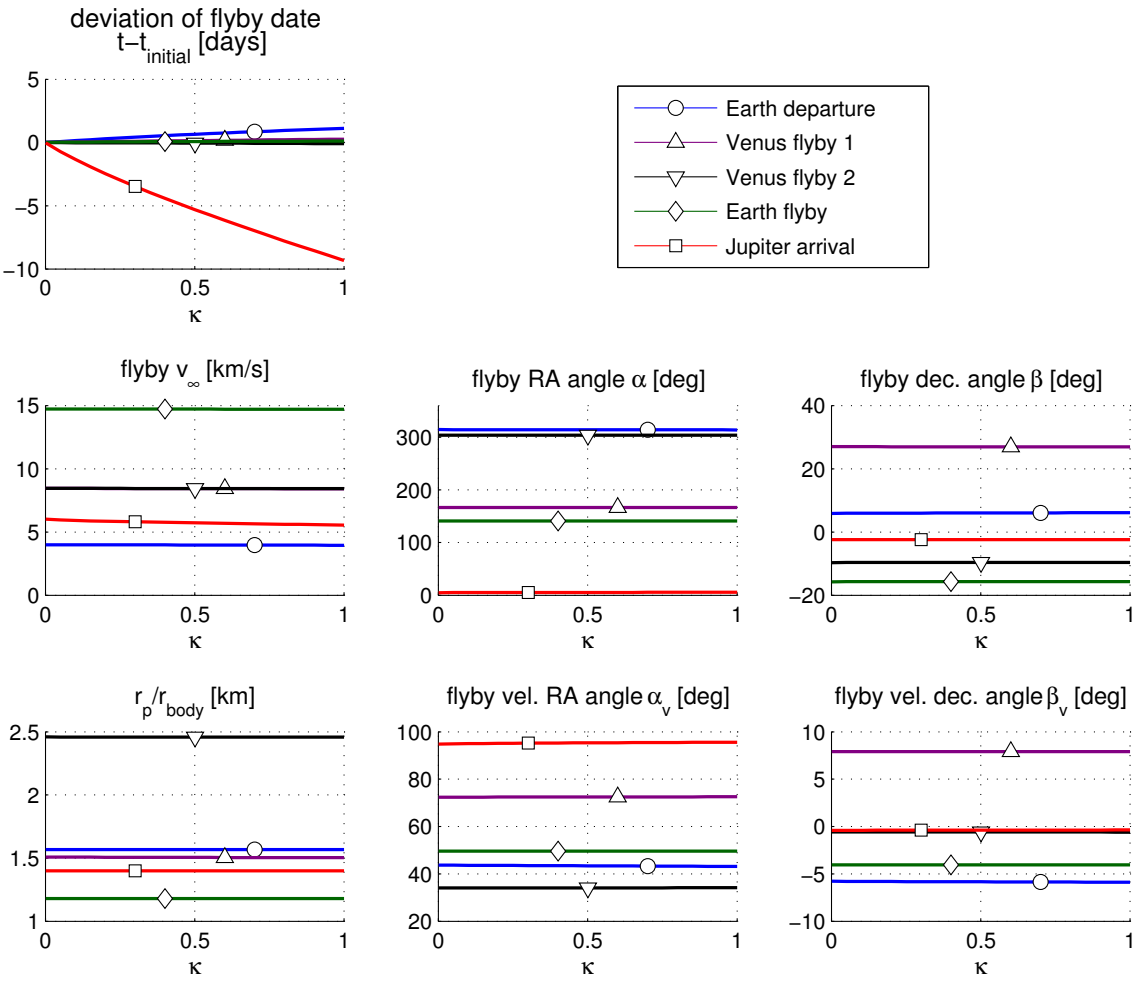

Figure 6.7: Variation of model parameters through continuation for the EVVEJ transfer

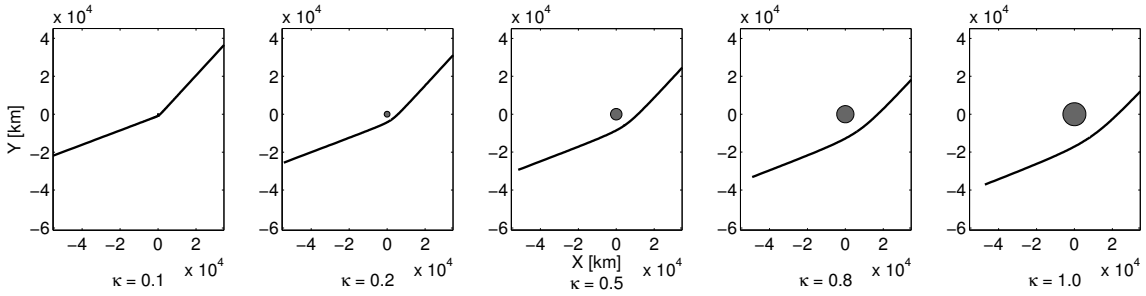

Figure 6.8: Successive iterations of the second flyby trajectory at Venus

Figure 6.8 shows actual results analogous to the theoretical depiction in Figure 6.1. The flyby shown is the second flyby trajectory at Venus in a Venus-centered inertial frame. As κ is increased, the algorithm increases the flyby periapsis between successive iterations to maintain the same hyperbolic turning angle, and the radius of Venus is artificially increased in a linear fashion. The mass and radius of Venus are linearly related to the continuation parameter κ, so the depicted size of Venus at each step is increases with changing κ.

6.8.2 Seven encounter tour of three Jovian moons

The second example is a seven-encounter tour of three of the Jovian moons. The spacecraft follows an encounter order of: Callisto - Ganymede - Ganymede - Callisto - Ganymede - Europa - Ganymede (CGGCGEG). This trajectory is complex, involves a large number of intermediate flybys with multiple revolutions about the central body, and is in a region of fast-changing non-Keplerian dynamics. The result shown is converged using an initial $\kappa_0 = 0.02$ and $\Delta\kappa = 0.02$, with both the initial and final radii at $r_{p,f} = 3000$ km. The continuation process completed in 22 minutes.

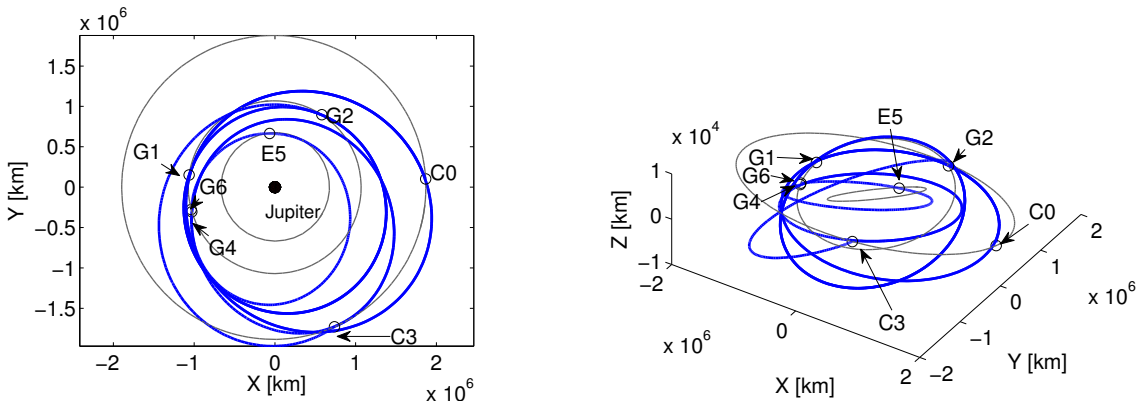

(a) 2D transfer

(b) 3D transfer - axis scaling is unequal

Figure 6.9: Converged CGGCGEG transfer

Figure 6.9 shows the final converged tour, with Jupiter as the central body and the orbit of each moon in question shown as thin lines. The distance of the spacecraft from Jupiter is shown in Figure 6.10, with encounter close approach times shown as dashed lines. Note that the epoch time (t_0) is JD 2461287.866. Encounters labeled with a G are Ganymede, C are Callisto, and E is Europa. Encounters are numbered sequentially from 0. The formatting of this figure is modeled after a similar figure in the work by Campagnola, Buffington, and Petropoulos [19].

Figure 6.11 shows the variation of the model parameters through the continuation process. Unlike the EVVEJ variation in Figure 6.7, the model parameters do not remain nearly constant (again, note that the horizontal axis in each subfigure is the independent control parameter κ). This behavior signifies the necessity of a continuation procedure; the scenario does not converge directly for $\kappa_0 = 1$. It is evident that the converged values for some parameters vary significantly between a near-ZSOI case ($\kappa << 1$) and the full ephemeris model ($\kappa = 1$). Because of this

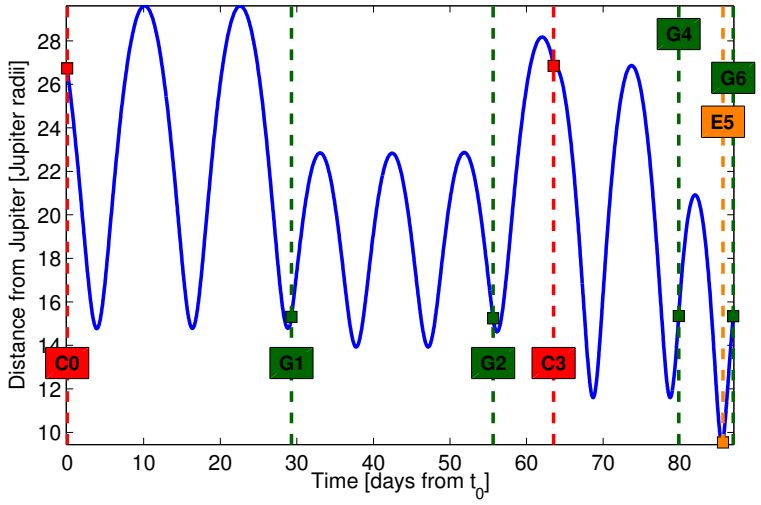

Figure 6.10: Distance from Jupiter throughout tour.

variation through the continuation, the initial ZSOI guess for the parameters is not a sufficiently good initial guess for the full model, and using these parameters directly as an initial guess leads to lack of convergence. By applying the continuation methodology, however, a converged solution is found.

The ability to find a continuous solution may be limited by the problem itself, as a given ZSOI trajectory may not exist ballistically in a full ephemeris model without violating constraints. The existence of a solution in a full model is dependent on a variety of factors, including the number of encounters and how closely the full ephemeris dynamics are modeled as being Keplerian. The ability of the algorithm to find these solutions is sensitive to inner loop software parameters such as convergence tolerance, maximum parameter step size, and the continuation step size $\Delta\kappa$. Some cases with a high number of flybys proceed with acceptable convergence properties

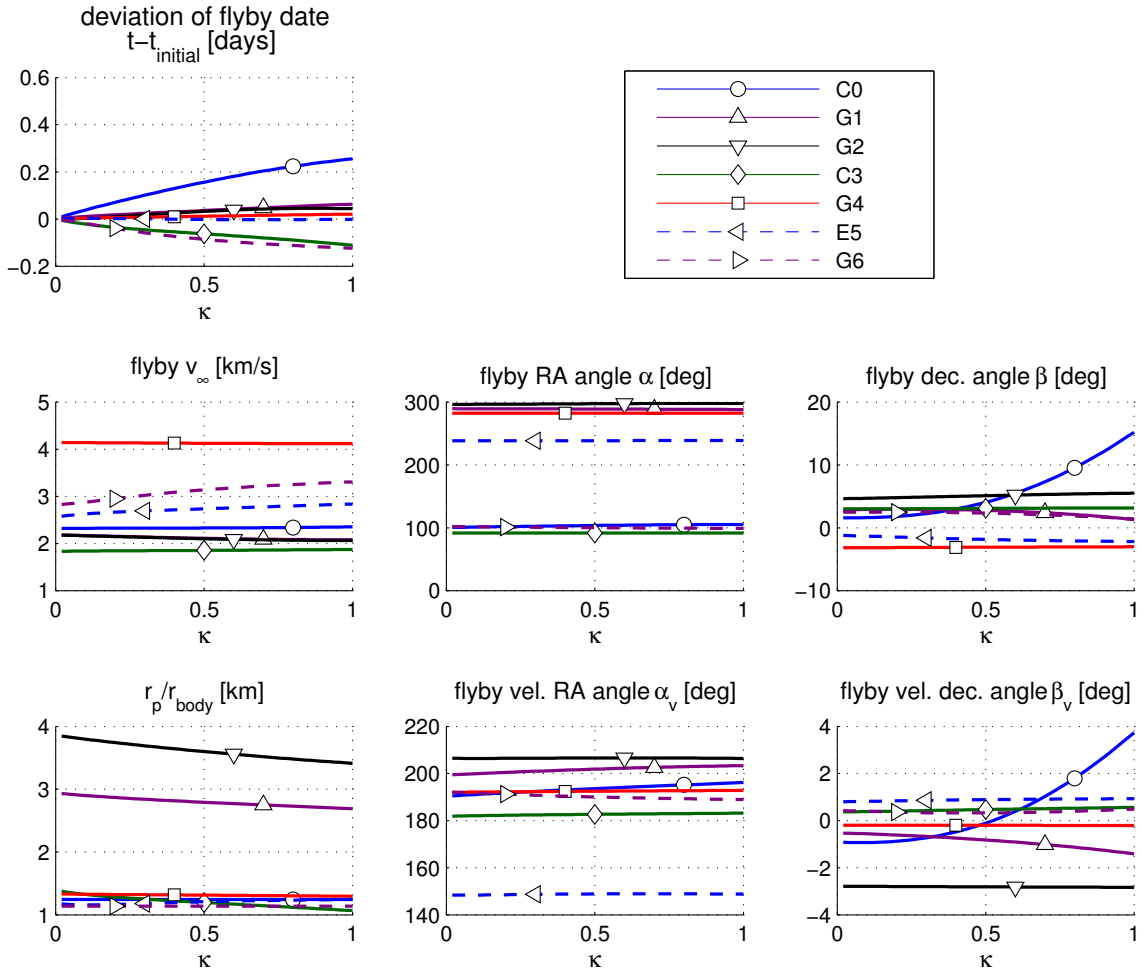

Figure 6.11: Variation of model parameters through the continuation process for the CGGCGEG transfer.

until larger values of κ are encountered, at which point convergence fails and no solution is found. In many of these cases, the solution does not exist with positive flyby altitudes, which may indicate that these many-encounter ZSOI tour solutions simply do not admit a continuous ballistic solution.

In the terminology of continuation methods, the inability to find a solution that satisfies all constraints for $\kappa = 1$ may potentially indicate the nonexistence of a smooth curve connecting the two homotopy levels $\kappa = 0$ and $\kappa = 1$. Of course, the inability to find a solution may not be due to the underlying structure of the problem, but rather to the implementation of the algorithm (e.g. choice of $\Delta\kappa$). Likewise, multiple solutions may exist for the $\kappa = 1$ level; smooth curves may branch during the continuation, and multiple "zero points" (solution states) of the final level are certainly admissible.

The likelihood of success in transitioning to the full ephemeris can be improved by including extra margins in the equivalent flyby altitudes and reducing the number of encounters in the ZSOI initial guess. Another possible solution is to allow for intermediate Δv maneuvers on each transfer leg, and to cast the problem as a minimization of the overall Δv.

6.8.3 Patched moon tour

In practice, longer ballistic tours may be constructed by patching together solutions with fewer encounters, allowing for small Δv discrepancies at the bodies used to patch the tours. In the Jovian moon tour solution with seven encounters, the flyby state at Europa (E5) may be used as the initial state in a subsequent tour,

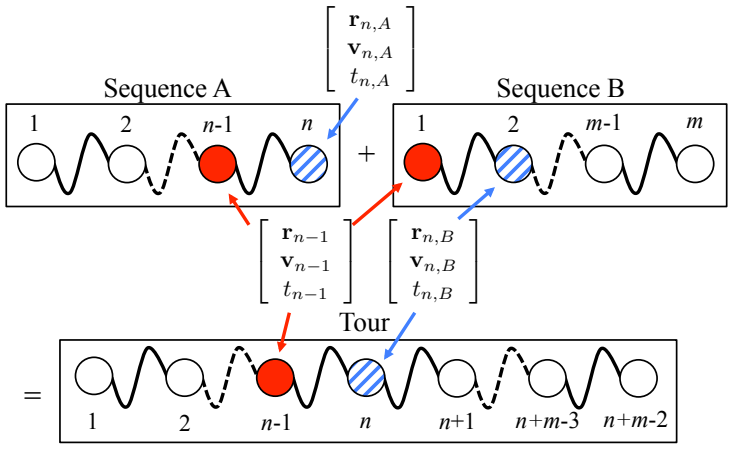

Figure 6.12: Schematic of patching tours together into chains

and solutions of arbitrary length may be constructed by chaining smaller sequences together. This procedure is shown schematically in Figure 6.12 (in the figure, each box is a separate continuation run, and the states shown are converged in the n-body model [$\kappa = 1$]). An example patched tour is shown in Figure 6.13. This extension continues the CGGCGEG tour by patching an EGGEGGE tour, effectively adding five more encounters. In the procedure, a small Δv (≤ 1 m/s) is allowed at the patch time immediately after the patching body (Europa, in this case), while periapsis state and flyby time are held constant. Current design practice is to chain shorter (one or two flyby) solutions together to form longer tours [18]; the algorithm presented here extends the capability of tour design to include more encounters in a single calculation sequence.

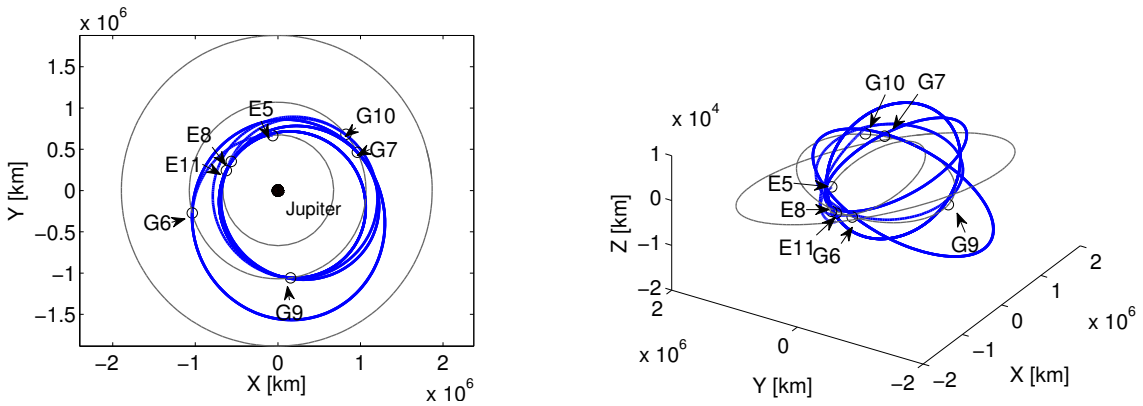

(a) 2D transfer

(b) 3D transfer - axis scaling is unequal

Figure 6.13: Converged EGGEGGE extension

6.9 Chapter conclusion

In designing tour missions to planets or moons, mission designers often begin with a patched conics zero sphere of influence (ZSOI) model, or other simplistic dynamical model. To ultimately fly a trajectory, however, the simplistic trajectory must be transferred to a continuous, integrated trajectory that takes into account n-body gravity and ephemeris locations. This transition is frequently overlooked.

This chapter presents a multi-part method to take a ZSOI initial guess and converge a ballistic trajectory in an n-body ephemeris model. This approach uses a continuation method, where a control parameter is tied to body masses, ephemerides, and sphere of influence sizes. Qualitative properties of the initial guess are preserved, and the bounds of the control parameter replicate the patched conics and full-ephemeris models exactly. An auxiliary Keplerian ephemeris is introduced to facilitate the calculation of "fake" ephemerides at each step in the continuation process. These ephemerides are continuously defined at any control parameter value,

and have applications outside of this continuation method algorithm, where they may be applied to a variety of trajectory problems where a smooth ephemeris is beneficial.

Two examples are given: one of a heliocentric EVVEJ transfer, and one of a Jovian moon tour with the solution to a ballistic seven-encounter tour. For the method presented, the maximum number of encounters for a Jovian moon tour is typically between five to nine, depending on the scenario. Longer tours may be designed by patching together multiple cases, extending the number of encounters possible in the full ephemeris model.

This continuation method has applications in designing interplanetary trajectories and in small-body tour design, where a trajectory in simplified dynamics is usually not an acceptable initial guess for converging an n-body ephemeris trajectory. In simpler models with relatively few flybys or slow-changing dynamics, this method allows for simple model design trades. In more complex models with faster changing dynamics or more target bodies, the method may be used to increase the number of sequential flybys that may be designed simultaneously. Overall, this method presents a continuous and differentiable pathway between a patched conics ZSOI model and a full n-body gravitational model, and is applicable to designing accurate flybys and tours.

The material presented here originated from the desire for a better initial guess routine to incorporate a Lunar flyby for Earth-centered FRTs (see Section 5.3.2.1). The method developed in this chapter may be used to convert any trajectory or

set of trajectories in simplistic models to full n-body dynamical models, and is not constrained to the specific situation from which it originated.

Chapter 7

Conclusion

7.1 Dissertation summary

The heart of this dissertation is the development of methods for computing initial guesses and optimal solutions for trajectories to Near-Earth Asteroids by utilizing orbits that ballistically return to the Earth. There are multiple phases in this process, and as with any mission design procedure, the problem is approached in successively more realistic and complex dynamical models. The benefit of utilizing the specific type of trajectory described in this dissertation is that it provides an abort option that uses no propellant. In planning future manned missions beyond Lunar orbit, it will be critical to incorporate an aspect of crew risk mitigation into the trajectory design. In the event of fuel loss or engine failure, Free Return Trajectories provide a viable (and perhaps, the only) option to return the crew to the Earth.

Additionally, this dissertation addresses trajectory design across different dynamical frameworks. A method is described to transition low-fidelity trajectories to high-fidelity dynamics using a continuation method. These trajectories need not be limited to the free return variety; the method may be applied to any trajectory that performs body flybys, such as interplanetary or inter-moon tours.

In Chapter 1, a summary of the relevant literature is presented, with previous works organized by topic, and each topic related to the work presented in the dissertation. The various dynamical systems and constants are described in Chapter 2.

The concept of an Earth-centered Free Return Trajectory is discussed in Chapter 3. The most basic solar system dynamical model is used first to describe trajectories that return to the Earth with no deterministic velocity maneuvers. Subsequently, trajectories that return to the Earth are found in the three-body problem with the Earth and the Sun as the only gravitating bodies. A systematic algorithm is developed to search through hundreds of thousands of initial conditions and converge parameters to obtain smooth, continuous, and differentiable trajectories that are independent of destination. These trajectories are compared to their two-body counterparts, and classified into family types according to prominent shape and time of flight characteristics.

The Free Return Trajectories are applied to Near-Earth Asteroid rendezvous in Chapter 4. The library of free returns is searched with an algorithm to automatically determine the best trajectory to utilize and the best pair of departure and arrival times with the target asteroid. An initial guess is generated and subsequently converged in the three-body problem with the Earth and the Sun. The converged trajectory is locally optimal in a Δv sense, and represents a continuous pathway to the selected asteroid. The mission profile is that of a hybrid free return trajectory, which utilizes a free return for the first segment of the mission, but departs at some time to rendezvous with the objective asteroid. The spacecraft stays with the aster-

oid for some amount of time before optimally departing for return to Earth. This scheme incorporates the risk mitigation aspect by allowing the spacecraft to stay on the free return if a mission anomaly occurs, bypassing the intermediate maneuver and returning to Earth.

Chapter 5 presents an alternative scheme to the results presented in Chapter 4, by utilizing the Moon for a flyby on the Earth departure leg to lower the Δv cost. For one example asteroid, it is shown that flying by the Moon decreases the amount of Δv capability required, even while introducing some inherent risk by performing a ballistic Lunar flyby. An algorithm is developed that computes an initial guess and then converges a locally optimal solution in the full n-body ephemerides. The solution satisfies the same constraints as in the three-body dynamics of Chapter 4.

Finally, in Chapter 6, a continuation algorithm is described that transitions trajectories from low-fidelity dynamical models to high-fidelity dynamical models. This concept arose while developing the algorithm in Chapter 5 to obtain a more robust method of determining the initial guess for Lunar flyby. The algorithm and results presented in Chapter 6 are not limited to Free Return Trajectories or Lunar flyby. Rather, the algorithm has been broadened to include computation of fully integrated, n-body dynamical ballistic trajectories in an interplanetary or inter-moon framework. With a starting trajectory obtained in a two-body patched conics model, the algorithm successively transitions the trajectory to a full-ephemeris, full-dynamics model, and retains the ballistic nature and the qualitative properties of the body flybys.

7.2 Dissertation contributions

The major contributions of this dissertation to the body of knowledge are listed below.

1. A method to construct a library of feasible Free Return Trajectories that return to the Earth in a three-body model is given, and trajectories are classified into several different families.

2. The concept of utilizing a Free Return Trajectory to rendezvous with a Near-Earth Asteroid is presented. Both concepts separately are not new, but combining them into one applied problem is novel to the literature. A method of computing initial guesses and converging optimal trajectories is also described.

3. An argument is presented for the use of free returns for manned missions to Near Earth Asteroids. The use of these trajectories lowers risk appreciably in a qualitative manner by providing a no-fuel abort option for manned missions. The trajectories are shown to be feasible from a Δv perspective, and costs can be further lowered by taking advantage of Lunar flyby scenarios.

4. A novel continuation method is presented to assist mission designers in obtaining full-ephemeris versions of trajectories that visit multiple bodies. The current practice is usually to construct tour sequences only a few bodies at a time. The results presented in this dissertation demonstrate an increase in the number of sequential bodies that can be converged at one time from a patched conic model, and an extension to the trajectory may be used to patch an additional tour to the end with a very small Δv maneuver.

7.3 Related publications

The majority of the work contained in this dissertation has been presented previously at conferences, and/or published in peer-reviewed journals. Chapter 3 contains work presented at the 2013 Space Flight Mechanics Meeting in Lihue, HI [13]. Chapter 4 also contains work from Ref. [13], and incorporates material published in the Journal of Guidance, Control, and Dynamics [14]. Chapter 5 was presented at the 2013 Astrodynamics Specialist Conference in Hilton Head, SC [12]; the conference material was developed in collaboration with Sonia Hernandez, a fellow graduate student at UT-Austin. Finally, Chapter 6 was presented at the 2014 Space Flight Mechanics Meeting in Santa Fe, NM [11]. A related paper has been submitted for publication to the Journal of the Astronautical Sciences [10].

7.4 Future work

Future work arising from the work presented in this dissertation will involve some or all of the following tasks that will contribute to the field.

- Applying the continuation method to the Lunar flyby problem, to obtain a more robust initial guess for the optimizer
- Including more robust capability in the continuation method, such as branch detection, predictor-corrector steps, and arc-length parameterization
- Conducting a broader search for good initial guesses for a larger subset of Near-Earth Asteroids, with the goal of computing Free Return Trajectories with lower Δv cost

- Incorporating a finite-thrust conversion routine for the impulsive trajectories presented
- Including actual asteroid size, mass, and shape to determine relevant flyby and rendezvous parameters
- Determining a way to automatically classify families of Free Return Trajectories by common characteristics, rather than relying on manual classification
- Computing the reachable domain of Free Return Trajectories in a theoretical sense, given a limiting departure velocity from Earth

7.5 Concluding remarks

The subject of Near-Earth Asteroid rendezvous, both with robotic and manned missions, is a rich field of study. The hope of presenting the material in this dissertation is that mission design in the coming years will benefit from this description of computing Free Return Trajectories as a no-fuel abort option on these potentially risky missions. The continuation method is presented as a potentially useful tool for both robotic and manned mission design. As humanity extends its reaches into the Solar System, novel algorithms and methods to design trajectories will continue to be needed, and the work presented in this dissertation simply represents a small contribution in our global effort to continue to explore beyond our world.

Appendices

Appendix A

Analytical Gradients for Computing Earth-centered Free Return Trajectories

This appendix contains analytical gradients of the cost function and constraints for determining and classifying Earth-centered FRTs (Chapter 3). For the sequential quadratic programming (SQP) optimization routine, these gradients are calculated using the variational equations given in Eq. (3.13) with the numerical integration of the state transition matrix given in Eq. (3.12). Each term in the equality and inequality constraint vectors ($\mathbf{c}$ and $\mathbf{d}$ in Eq. (3.11), respectively) is given a subscript here for brevity; e.g. the n^{th} term listed in the inequality constraint vector is shown here as $\mathbf{d}_n$.

Additionally, the state transition matrix is divided into four 3×3 submatrices, so that the state transition matrix from t_a to t_b is denoted as:

$$\mathbf{\Phi}_{ba} = \left[\begin{array}{c|c} \mathbf{A}_{ba} & \mathbf{B}_{ba} \\ \hline \mathbf{C}_{ba} & \mathbf{D}_{ba} \end{array}\right]$$

The analytical gradients are given in the following equations. Note that t_m represents the patch time of the trajectory segments, which is equivalent to $(t_0+t_f)/2$ in Figure 3.20 and Eq. (3.5).

A.1 Equality constraint gradients

Due to the coupled nature of δ according to Eq. (3.4), some equations contain a term $\mathbf{\Delta}_\phi$, $\mathbf{\Delta}_\lambda$, or $\mathbf{\Delta}_\alpha$, which are described separately. These terms are evaluated at the time denoted by their second subscript.

$$\frac{\partial \mathbf{c}_1}{\partial \phi_0} = -\mathbf{A}_{m0} r_0 \begin{bmatrix} -\sin\phi_0 \cos\lambda_0 \\ -\sin\phi_0 \sin\lambda_0 \\ \cos\phi_0 \end{bmatrix} - \mathbf{B}_{m0} v_0 \begin{bmatrix} -\sin\delta_0 \cos\alpha_0 \\ -\sin\delta_0 \sin\alpha_0 \\ \cos\delta_0 \end{bmatrix} \mathbf{\Delta}_{\phi,0}$$

$$\frac{\partial \mathbf{c}_2}{\partial \phi_0} = -\mathbf{C}_{m0} r_0 \begin{bmatrix} -\sin\phi_0 \cos\lambda_0 \\ -\sin\phi_0 \sin\lambda_0 \\ \cos\phi_0 \end{bmatrix} - \mathbf{D}_{m0} v_0 \begin{bmatrix} -\sin\delta_0 \cos\alpha_0 \\ -\sin\delta_0 \sin\alpha_0 \\ \cos\delta_0 \end{bmatrix} \mathbf{\Delta}_{\phi,0}$$

$$\frac{\partial \mathbf{c}_1}{\partial \lambda_0} = -\mathbf{A}_{m0} r_0 \begin{bmatrix} -\cos\phi_0 \sin\lambda_0 \\ \cos\phi_0 \cos\lambda_0 \\ 0 \end{bmatrix} - \mathbf{B}_{m0} v_0 \begin{bmatrix} -\sin\delta_0 \cos\alpha_0 \\ -\sin\delta_0 \sin\alpha_0 \\ \cos\delta_0 \end{bmatrix} \mathbf{\Delta}_{\lambda,0}$$

$$\frac{\partial \mathbf{c}_2}{\partial \lambda_0} = -\mathbf{C}_{m0} r_0 \begin{bmatrix} -\cos\phi_0 \sin\lambda_0 \\ \cos\phi_0 \cos\lambda_0 \\ 0 \end{bmatrix} - \mathbf{D}_{m0} v_0 \begin{bmatrix} -\sin\delta_0 \cos\alpha_0 \\ -\sin\delta_0 \sin\alpha_0 \\ \cos\delta_0 \end{bmatrix} \mathbf{\Delta}_{\lambda,0}$$

$$\frac{\partial \mathbf{c}_1}{\partial v_0} = -\mathbf{B}_{m0} \begin{bmatrix} \cos\delta_0 \cos\alpha_0 \\ \cos\delta_0 \sin\alpha_0 \\ \sin\delta_0 \end{bmatrix}, \qquad \frac{\partial \mathbf{c}_2}{\partial v_0} = -\mathbf{D}_{m0} \begin{bmatrix} \cos\delta_0 \cos\alpha_0 \\ \cos\delta_0 \sin\alpha_0 \\ \sin\delta_0 \end{bmatrix}$$

$$\frac{\partial \mathbf{c}_1}{\partial \alpha_0} = -\mathbf{B}_{m0} v_0 \begin{bmatrix} -\cos\delta_0 \sin\alpha_0 \\ \cos\delta_0 \cos\alpha_0 \\ 0 \end{bmatrix} - \mathbf{B}_{m0} v_0 \begin{bmatrix} -\sin\delta_0 \cos\alpha_0 \\ -\sin\delta_0 \sin\alpha_0 \\ \cos\delta_0 \end{bmatrix} \mathbf{\Delta}_{\alpha,0}$$

$$\frac{\partial \mathbf{c}_2}{\partial \alpha_0} = -\mathbf{D}_{m0} v_0 \begin{bmatrix} -\cos\delta_0 \sin\alpha_0 \\ \cos\delta_0 \cos\alpha_0 \\ 0 \end{bmatrix} - \mathbf{D}_{m0} v_0 \begin{bmatrix} -\sin\delta_0 \cos\alpha_0 \\ -\sin\delta_0 \sin\alpha_0 \\ \cos\delta_0 \end{bmatrix} \mathbf{\Delta}_{\alpha,0}$$

$$\frac{\partial \mathbf{c}_1}{\partial \phi_f} = \mathbf{A}_{mf} r_f \begin{bmatrix} -\sin\phi_f \cos\lambda_f \\ -\sin\phi_f \sin\lambda_f \\ \cos\phi_f \end{bmatrix} + \mathbf{B}_{mf} v_f \begin{bmatrix} -\sin\delta_f \cos\alpha_f \\ -\sin\delta_f \sin\alpha_f \\ \cos\delta_f \end{bmatrix} \mathbf{\Delta}_{\phi,f}$$

$$\frac{\partial \mathbf{c}_2}{\partial \phi_f} = \mathbf{C}_{mf} r_f \begin{bmatrix} -\sin\phi_f \cos\lambda_f \\ -\sin\phi_f \sin\lambda_f \\ \cos\phi_f \end{bmatrix} + \mathbf{D}_{mf} v_f \begin{bmatrix} -\sin\delta_f \cos\alpha_f \\ -\sin\delta_f \sin\alpha_f \\ \cos\delta_f \end{bmatrix} \mathbf{\Delta}_{\phi,f}$$

$$\frac{\partial \mathbf{c}_1}{\partial \lambda_f} = \mathbf{A}_{mf} r_f \begin{bmatrix} -\cos\phi_f \sin\lambda_f \\ \cos\phi_f \cos\lambda_f \\ 0 \end{bmatrix} + \mathbf{B}_{mf} v_f \begin{bmatrix} -\sin\delta_f \cos\alpha_f \\ -\sin\delta_f \sin\alpha_f \\ \cos\delta_f \end{bmatrix} \mathbf{\Delta}_{\lambda,f}$$

$$\frac{\partial \mathbf{c}_2}{\partial \lambda_f} = \mathbf{C}_{mf} r_f \begin{bmatrix} -\cos\phi_f \sin\lambda_f \\ \cos\phi_f \cos\lambda_f \\ 0 \end{bmatrix} + \mathbf{D}_{mf} v_f \begin{bmatrix} -\sin\delta_f \cos\alpha_f \\ -\sin\delta_f \sin\alpha_f \\ \cos\delta_f \end{bmatrix} \mathbf{\Delta}_{\lambda,f}$$

$$\frac{\partial \mathbf{c}_1}{\partial v_f} = \mathbf{B}_{mf} \begin{bmatrix} \cos\delta_f \cos\alpha_f \\ \cos\delta_f \sin\alpha_f \\ \sin\delta_f \end{bmatrix}, \qquad \frac{\partial \mathbf{c}_2}{\partial v_f} = \mathbf{D}_{mf} \begin{bmatrix} \cos\delta_f \cos\alpha_f \\ \cos\delta_f \sin\alpha_f \\ \sin\delta_f \end{bmatrix}$$

$$\frac{\partial \mathbf{c}_1}{\partial \alpha_f} = \mathbf{B}_{mf} v_f \begin{bmatrix} -\cos\delta_f \sin\alpha_f \\ \cos\delta_f \cos\alpha_f \\ 0 \end{bmatrix} + \mathbf{B}_{mf} v_f \begin{bmatrix} -\sin\delta_f \cos\alpha_f \\ -\sin\delta_f \sin\alpha_f \\ \cos\delta_f \end{bmatrix} \mathbf{\Delta}_{\alpha,f}$$

$$\frac{\partial \mathbf{c}_2}{\partial \alpha_f} = \mathbf{D}_{mf} v_f \begin{bmatrix} -\cos\delta_f \sin\alpha_f \\ \cos\delta_f \cos\alpha_f \\ 0 \end{bmatrix} + \mathbf{D}_{mf} v_f \begin{bmatrix} -\sin\delta_f \cos\alpha_f \\ -\sin\delta_f \sin\alpha_f \\ \cos\delta_f \end{bmatrix} \mathbf{\Delta}_{\alpha,f}$$

$$\frac{\partial \mathbf{c}_1}{\partial t_m} = -\mathbf{v}_1, \qquad \frac{\partial \mathbf{c}_2}{\partial t_m} = -\ddot{\mathbf{r}}_1$$

$$\frac{\partial \mathbf{c}_1}{\partial t_f} = -\mathbf{A}_{mf}\mathbf{v}_f - \mathbf{B}_{mf}\ddot{\mathbf{r}}_f, \qquad \frac{\partial \mathbf{c}_2}{\partial t_f} = -\mathbf{C}_{mf}\mathbf{v}_f - \mathbf{D}_{mf}\ddot{\mathbf{r}}_f$$

Where:

$$\mathbf{\Delta}_\phi = \frac{\left(\sin\alpha\sin\lambda + \cos\alpha\cos\lambda\right)\left(\tan^2\phi + 1\right)}{\left(\sin\alpha\sin\lambda + \cos\alpha\cos\lambda\right)^2 + \tan^2\phi}$$

$$\mathbf{\Delta}_\lambda = \frac{\cos\alpha\sin\lambda - \cos\lambda\sin\alpha}{\cot\phi\left(\sin\alpha\sin\lambda + \cos\alpha\cos\lambda\right)^2 + \tan\phi}$$

$$\mathbf{\Delta}_\alpha = -\frac{\cos\alpha\sin\lambda - \cos\lambda\sin\alpha}{\cot\phi\left(\sin\alpha\sin\lambda + \cos\alpha\cos\lambda\right)^2 + \tan\phi}$$

A.2 Inequality constraint gradients

The only non-zero gradients are given below.

$$\frac{\partial \mathbf{d}_1}{\partial t_m} = 1, \qquad \frac{\partial \mathbf{d}_2}{\partial t_f} = 1, \qquad \frac{\partial \mathbf{d}_3}{\partial t_m} = -1, \qquad \frac{\partial \mathbf{d}_3}{\partial t_f} = -1, \qquad \frac{\partial \mathbf{d}_4}{\partial t_m} = 1,$$

$$\frac{\partial \mathbf{d}_4}{\partial t_f} = 1, \qquad \frac{\partial \mathbf{d}_5}{\partial v_0} = 1, \qquad \frac{\partial \mathbf{d}_6}{\partial v_f} = 1, \qquad \frac{\partial \mathbf{d}_7}{\partial v_0} = -1, \qquad \frac{\partial \mathbf{d}_8}{\partial v_f} = -1$$

Appendix B

Accessible Near-Earth Asteroid Orbital Elements and Initial Guesses

This appendix pertains to the NEA destinations and initial guess dates for the FRT-to-NEA rendezvous problem in Chapter 4. Table B.1 contains the osculating orbital elements for the five most accessible NEAs in a Δv sense, according to the NHATS survey [2]. Table B.2 gives the initial guess event dates for each NEA rendezvous case.

In Table B.1, note that NEAs may be classified into different types, based on their semimajor axis, perihelion distance, and aphelion distance. The classification types are each named after an asteroid of that specific type: Atiras (163693 Atira), Atens (2062 Aten), Apollos (1862 Apollo), and Amors (1221 Amor)[1].

[1]Definitions of classification types may be found from JPL's Near Earth Object Program website, accessible at `http://neo.jpl.nasa.gov/neo/groups.html`. Last accessed 3 June 2014

Table B.1: Asteroid destinations

Name	2000 SG344	2006 BZ147	2009 HC	2001 FR85	2012 UV136
Type	Aten	Apollo	Apollo	Aten	Apollo
NHATS Δv (km/s)	3.556	4.184	4.504	4.557	5.054
Epoch (JD)	2456200.5	2456200.5	2456400.5	2456400.5	2456400.5
a (AU)	0.9775209163283	1.023544592219	1.039399273821	0.9827831955759	1.005852224385
e	0.06689812308950	0.09865382126613	0.1256976981516	0.02789365084104	0.1384102351015
i (deg)	0.1111697147738	1.409251753404	3.778071141868	5.244771224602	2.218138035745
Ω (deg)	192.1305783940	139.838409547	203.8233492055	183.071722826	210.9190260343
ω (deg)	275.1353645151	94.74217142863	269.8422021781	233.562063763	290.1546780057463
M (deg)	60.14272860509	63.57403853828	359.027088608	260.7667378991	78.49757209528

Table B.2: Initial guess dates for NEA rendezvous

Name	2000 SG344	2006 BZ147	2009 HC	2001 FR85	2012 UV136
FRT selected	IV^-	IV^-	III^+	I^-	IV^-
Departure date (t_0)	2027 Apr 12	2037 Aug 25	2025 Oct 25	2038 Oct 06	2021 May 19
FRT departure date (t_c)	2028 Jan 31	2037 Sep 30	2026 Nov 05	2038 Nov 11	2021 Sep 14
End of Lambert traj. (t_a)	2028 Jun 29	2038 Jan 08	2027 Jan 24	2039 Apr 10	2021 Dec 03
FRT return to Earth (t_{FR})	2028 Apr 10	2038 Aug 25	2027 Apr 07	2039 Apr 06	2022 May 18

Appendix C

Analytical Gradients for FRT-to-NEA Optimization

This appendix pertains to obtaining the Δv-optimal solution for NEA rendezvous using an FRT in the CRTBP (Chapter 4). Presented here are the analytical gradients of the cost function (total Δv) and constraints with respect to the parameters in the parameter vector (see Eq. (4.2)).

C.1 Definitions

$$\Delta\mathbf{v}_a \equiv \mathbf{v}_a(t_a) - \mathbf{v}_{sc}^{FWD}(t_a)$$

$$\Delta\mathbf{v}_d \equiv \mathbf{v}_{sc}^{BWD}(t_d) - \mathbf{v}_a(t_d)$$

$$\mathbf{\Phi}_{ba} \equiv \left[\begin{array}{c|c} \mathbf{A}_{ba} & \mathbf{B}_{ba} \\ \hline \mathbf{C}_{ba} & \mathbf{D}_{ba} \end{array}\right]$$

$$\mathbf{g} \equiv \ddot{\mathbf{r}}$$

C.2 Cost function

$$\frac{\partial J}{\partial t_0} = \frac{\Delta\mathbf{v}_a^\top}{\Delta v_a}\left(\mathbf{C}_{a0}\mathbf{v}_0 + \mathbf{D}_{a0}\mathbf{g}_{sc}(t_0)\right) \tag{C.1}$$

$$\frac{\partial J}{\partial t_c} = -\frac{\Delta\mathbf{v}_a^\top}{\Delta v_a}\left[\mathbf{C}_{ac}\left(\mathbf{v}_{sc}^{FWD-}(t_c) - \mathbf{v}_{sc}^{FWD+}(t_c)\right) + \mathbf{D}_{ac}\left(\mathbf{g}_{sc}^{FWD-}(t_c) - \mathbf{g}_{sc}^{FWD+}(t_c)\right)\right] \tag{C.2}$$

$$\frac{\partial J}{\partial t_a} = \frac{\Delta \mathbf{v}_a^\top}{\Delta v_a}\left(\mathbf{g}_a(t_a) - \mathbf{g}_{sc}^{FWD}(t_a)\right) \tag{C.3}$$

$$\frac{\partial J}{\partial t_d} = \frac{\Delta \mathbf{v}_d^\top}{\Delta v_d}\left(\mathbf{g}_a(t_d) - \mathbf{g}_{sc}^{FWD}(t_d)\right) \tag{C.4}$$

$$\frac{\partial J}{\partial t_{FR}} = 0 \tag{C.5}$$

$$\frac{\partial J}{\partial t_f} = \frac{\Delta \mathbf{v}_d^\top}{\Delta v_d}\left(-\mathbf{C}_{df}\mathbf{v}_f - \mathbf{D}_{df}\mathbf{g}_{sc}(t_f)\right) \tag{C.6}$$

$$\frac{\partial J}{\partial \lambda_0} = \frac{\Delta \mathbf{v}_a^\top}{\Delta v_a}\left(-\mathbf{C}_{a0} r_0 \begin{bmatrix} -\cos\zeta_0 \sin\lambda_0 \\ -\sin\zeta_0 \sin\lambda_0 \\ \cos\lambda_0 \end{bmatrix}\right) \tag{C.7}$$

$$\frac{\partial J}{\partial \lambda_{FR}} = 0 \tag{C.8}$$

$$\frac{\partial J}{\partial \lambda_f} = \frac{\Delta \mathbf{v}_d^\top}{\Delta v_d}\left(-\mathbf{C}_{df} r_f \begin{bmatrix} -\cos\zeta_f \sin\lambda_f \\ -\sin\zeta_f \sin\lambda_f \\ \cos\lambda_f \end{bmatrix}\right) \tag{C.9}$$

$$\frac{\partial J}{\partial \zeta_0} = \frac{\Delta \mathbf{v}_a^\top}{\Delta v_a}\left(-\mathbf{C}_{a0} r_0 \begin{bmatrix} -\sin\zeta_0 \cos\lambda_0 \\ \cos\zeta_0 \cos\lambda_0 \\ 0 \end{bmatrix}\right) \tag{C.10}$$

$$\frac{\partial J}{\partial \zeta_{FR}} = 0 \tag{C.11}$$

$$\frac{\partial J}{\partial \zeta_f} = \frac{\Delta \mathbf{v}_d^\top}{\Delta v_d}\left(\mathbf{C}_{df} r_f \begin{bmatrix} -\sin\zeta_f \cos\lambda_f \\ \cos\zeta_f \cos\lambda_f \\ 0 \end{bmatrix}\right) \tag{C.12}$$

$$\frac{\partial J}{\partial \mathbf{v}_0} = \frac{\Delta \mathbf{v}_0^\top}{\Delta v_0} - \frac{\Delta \mathbf{v}_a^\top}{\Delta v_a}\mathbf{D}_{a0} \tag{C.13}$$

$$\frac{\partial J}{\partial \Delta \mathbf{v}_c} = \frac{\Delta \mathbf{v}_c^\top}{\Delta v_c} - \frac{\Delta \mathbf{v}_a^\top}{\Delta v_a}\mathbf{D}_{ac} \tag{C.14}$$

$$\frac{\partial J}{\partial \mathbf{v}_{FR}} = \mathbf{0}_{3\times 1} \tag{C.15}$$

$$\frac{\partial J}{\partial \mathbf{v}_f} = \frac{\Delta \mathbf{v}_d^\top}{\Delta v_d}\mathbf{D}_{df} \tag{C.16}$$

C.3 Inequality constraints

Nonzero inequality constraints are given here. The i^{th} element of the inequality constraint vector $\mathbf{d}$ is denoted as d_i.

$$\frac{\partial d_1}{\partial t_0} = 1 \tag{C.17}$$

$$\frac{\partial d_2}{\partial t_c} = -1, \quad \frac{\partial d_2}{\partial t_a} = 1 \tag{C.18}$$

$$\frac{\partial d_3}{\partial t_c} = -1, \quad \frac{\partial d_3}{\partial t_{FR}} = 1 \tag{C.19}$$

$$\frac{\partial d_4}{\partial t_d} = -1, \quad \frac{\partial d_4}{\partial t_f} = 1 \tag{C.20}$$

$$\frac{\partial d_5}{\partial t_0} = -1, \quad \frac{\partial d_5}{\partial t_c} = 1 \tag{C.21}$$

$$\frac{\partial d_6}{\partial t_a} = -1, \quad \frac{\partial d_6}{\partial t_d} = 1 \tag{C.22}$$

$$\frac{\partial d_7}{\partial t_a} = 1, \quad \frac{\partial d_7}{\partial t_{FR}} = -1 \tag{C.23}$$

$$\frac{\partial d_8}{\partial \lambda_{FR}} = -\mathbf{v}_{FR} r_f \begin{bmatrix} -\cos\zeta_{FR}\sin\lambda_{FR} \\ -\sin\zeta_{FR}\sin\lambda_{FR} \\ \cos\lambda_{FR} \end{bmatrix} \tag{C.24}$$

$$\frac{\partial d_9}{\partial \lambda_f} = -\mathbf{v}_f r_f \begin{bmatrix} -\cos\zeta_f\sin\lambda_f \\ -\sin\zeta_f\sin\lambda_f \\ \cos\lambda_f \end{bmatrix} \tag{C.25}$$

$$\frac{\partial d_8}{\partial \zeta_{FR}} = -\mathbf{v}_{FR} r_f \begin{bmatrix} -\sin\zeta_{FR}\cos\lambda_{FR} \\ \cos\zeta_{FR}\cos\lambda_{FR} \\ 0 \end{bmatrix} \tag{C.26}$$

$$\frac{\partial d_9}{\partial \zeta_f} = -\mathbf{v}_f r_f \begin{bmatrix} -\sin\zeta_f\cos\lambda_f \\ \cos\zeta_f\cos\lambda_f \\ 0 \end{bmatrix} \tag{C.27}$$

$$\frac{\partial d_8}{\partial \mathbf{v}_{FR}} = -\mathbf{r}_{FR} \tag{C.28}$$

$$\frac{\partial d_9}{\partial \mathbf{v}_f} = -\mathbf{r}_f \tag{C.29}$$

C.4 Equality constraints

Nonzero equality constraints are given here. The i^{th} element of the inequality constraint vector $\mathbf{c}$ is denoted as c_i.

$$\frac{\partial c_1}{\partial t_0} = -\left(\mathbf{A}_{c0}\mathbf{v}_0 + \mathbf{B}_{c0}\mathbf{g}_{sc}(t_0)\right) \tag{C.30}$$

$$\frac{\partial c_2}{\partial t_0} = -\left(\mathbf{C}_{c0}\mathbf{v}_0 + \mathbf{D}_{c0}\mathbf{g}_{sc}(t_0)\right) \tag{C.31}$$

$$\frac{\partial c_3}{\partial t_0} = -\left(\mathbf{A}_{a0}\mathbf{v}_0 + \mathbf{B}_{a0}\mathbf{g}_{sc}(t_0)\right) \tag{C.32}$$

$$\frac{\partial c_1}{\partial t_c} = \mathbf{v}_{sc}^{FWD-}(t_c) - \mathbf{v}_{sc}^{BWD}(t_c) \tag{C.33}$$

$$\frac{\partial c_2}{\partial t_c} = \mathbf{g}_{sc}^{FWD-}(t_c) - \mathbf{g}_{sc}^{BWD}(t_c) \tag{C.34}$$

$$\frac{\partial c_3}{\partial t_c} = \mathbf{A}_{ac}\left(\mathbf{v}_{sc}^{FWD-}(t_c) - \mathbf{v}_{sc}^{FWD+}(t_c)\right) + \mathbf{B}_{ac}\left(\mathbf{g}_{sc}^{FWD-}(t_c) - \mathbf{g}_{sc}^{FWD+}(t_c)\right) \tag{C.35}$$

$$\frac{\partial c_3}{\partial t_a} = \mathbf{v}_{sc}(t_a) - \mathbf{v}_a(t_a) \tag{C.36}$$

$$\frac{\partial c_4}{\partial t_d} = \mathbf{v}_{sc}(t_d) - \mathbf{v}_a(t_d) \tag{C.37}$$

$$\frac{\partial c_1}{\partial t_{FR}} = \mathbf{A}_{cFR}\mathbf{v}_{sc}(t_{FR}) + \mathbf{B}_{cFR}\mathbf{g}_{sc}(t_{FR}) \tag{C.38}$$

$$\frac{\partial c_2}{\partial t_{FR}} = \mathbf{C}_{cFR}\mathbf{v}_{sc}(t_{FR}) + \mathbf{D}_{cFR}\mathbf{g}_{sc}(t_{FR}) \tag{C.39}$$

$$\frac{\partial c_4}{\partial t_f} = -\mathbf{A}_{df}\mathbf{v}_{sc}(t_{FR}) - \mathbf{B}_{df}\mathbf{g}_{sc}(t_f) \tag{C.40}$$

$$\frac{\partial c_1}{\partial \lambda_0} = \mathbf{A}_{c0} r_0 \begin{bmatrix} -\cos\zeta_0 \sin\lambda_0 \\ -\sin\zeta_0 \sin\lambda_0 \\ \cos\lambda_0 \end{bmatrix} \tag{C.41}$$

$$\frac{\partial c_2}{\partial \lambda_0} = \mathbf{C}_{c0} r_0 \begin{bmatrix} -\cos\zeta_0 \sin\lambda_0 \\ -\sin\zeta_0 \sin\lambda_0 \\ \cos\lambda_0 \end{bmatrix} \tag{C.42}$$

$$\frac{\partial c_3}{\partial \lambda_0} = \mathbf{A}_{a0} r_0 \begin{bmatrix} -\cos\zeta_0 \sin\lambda_0 \\ -\sin\zeta_0 \sin\lambda_0 \\ \cos\lambda_0 \end{bmatrix} \tag{C.43}$$

$$\frac{\partial c_5}{\partial \lambda_0} = \frac{\mathbf{v}_0 \times \mathbf{h}_0}{r_0 v_0 h_0} r_0 \begin{bmatrix} -\cos\zeta_0 \sin\lambda_0 \\ -\sin\zeta_0 \sin\lambda_0 \\ \cos\lambda_0 \end{bmatrix} - \frac{h_0}{v_0 r_0^3} \mathbf{r}_{sc}(t_0) r_0 \begin{bmatrix} -\cos\zeta_0 \sin\lambda_0 \\ -\sin\zeta_0 \sin\lambda_0 \\ \cos\lambda_0 \end{bmatrix} \tag{C.44}$$

$$\frac{\partial c_1}{\partial \lambda_{FR}} = \mathbf{A}_{cFR} r_f \begin{bmatrix} -\cos\zeta_{FR} \sin\lambda_{FR} \\ -\sin\zeta_{FR} \sin\lambda_{FR} \\ \cos\lambda_{FR} \end{bmatrix} \tag{C.45}$$

$$\frac{\partial c_2}{\partial \lambda_{FR}} = \mathbf{C}_{cFR} r_f \begin{bmatrix} -\cos\zeta_{FR} \sin\lambda_{FR} \\ -\sin\zeta_{FR} \sin\lambda_{FR} \\ \cos\lambda_{FR} \end{bmatrix} \tag{C.46}$$

$$\frac{\partial c_6}{\partial \lambda_{FR}} = \frac{\mathbf{v}_{FR} \times \mathbf{h}_{FR}}{r_f v_{FR} h_{FR}} r_f \begin{bmatrix} -\cos\zeta_{FR} \sin\lambda_{FR} \\ -\sin\zeta_{FR} \sin\lambda_{FR} \\ \cos\lambda_{FR} \end{bmatrix} - \frac{h_{FR}}{v_{FR} r_f^3} \mathbf{r}_{sc}(t_{FR}) r_f \begin{bmatrix} -\cos\zeta_{FR} \sin\lambda_{FR} \\ -\sin\zeta_{FR} \sin\lambda_{FR} \\ \cos\lambda_{FR} \end{bmatrix} \tag{C.47}$$

$$\frac{\partial c_4}{\partial \lambda_f} = \mathbf{A}_{df} r_f \begin{bmatrix} -\cos\zeta_f \sin\lambda_f \\ -\sin\zeta_f \sin\lambda_f \\ \cos\lambda_f \end{bmatrix} \tag{C.48}$$

$$\frac{\partial c_7}{\partial \lambda_f} = \frac{\mathbf{v}_f \times \mathbf{h}_f}{r_f v_f h_f} r_f \begin{bmatrix} -\cos\zeta_f \sin\lambda_f \\ -\sin\zeta_f \sin\lambda_f \\ \cos\lambda_f \end{bmatrix} - \frac{h_f}{v_f r_f^3} \mathbf{r}_{sc}(t_f) r_f \begin{bmatrix} -\cos\zeta_f \sin\lambda_f \\ -\sin\zeta_f \sin\lambda_f \\ \cos\lambda_f \end{bmatrix} \tag{C.49}$$

$$\frac{\partial c_1}{\partial \zeta_0} = \mathbf{A}_{c0} r_0 \begin{bmatrix} -\sin\zeta_0 \cos\lambda_0 \\ \cos\zeta_0 \cos\lambda_0 \\ 0 \end{bmatrix} \tag{C.50}$$

$$\frac{\partial c_2}{\partial \zeta_0} = \mathbf{C}_{c0} r_0 \begin{bmatrix} -\sin\zeta_0 \cos\lambda_0 \\ \cos\zeta_0 \cos\lambda_0 \\ 0 \end{bmatrix} \tag{C.51}$$

$$\frac{\partial c_3}{\partial \zeta_0} = \mathbf{A}_{a0} r_0 \begin{bmatrix} -\sin\zeta_0 \cos\lambda_0 \\ \cos\zeta_0 \cos\lambda_0 \\ 0 \end{bmatrix} \tag{C.52}$$

$$\frac{\partial c_5}{\partial \zeta_0} = \frac{\mathbf{v}_0 \times \mathbf{h}_0}{r_0 v_0 h_0} r_0 \begin{bmatrix} -\sin\zeta_0 \cos\lambda_0 \\ \cos\zeta_0 \cos\lambda_0 \\ 0 \end{bmatrix} - \frac{h_0}{v_0 r_0^3} \mathbf{r}_{sc}(t_0) r_0 \begin{bmatrix} -\sin\zeta_0 \cos\lambda_0 \\ \cos\zeta_0 \cos\lambda_0 \\ 0 \end{bmatrix} \tag{C.53}$$

$$\frac{\partial c_1}{\partial \zeta_{FR}} = \mathbf{A}_{cFR} r_f \begin{bmatrix} -\sin\zeta_{FR} \cos\lambda_{FR} \\ \cos\zeta_{FR} \cos\lambda_{FR} \\ 0 \end{bmatrix} \tag{C.54}$$

$$\frac{\partial c_2}{\partial \zeta_{FR}} = \mathbf{C}_{cFR} r_f \begin{bmatrix} -\sin\zeta_{FR} \cos\lambda_{FR} \\ \cos\zeta_{FR} \cos\lambda_{FR} \\ 0 \end{bmatrix} \tag{C.55}$$

$$\frac{\partial c_6}{\partial \zeta_{FR}} = \frac{\mathbf{v}_{FR} \times \mathbf{h}_{FR}}{r_f v_{FR} h_{FR}} r_f \begin{bmatrix} -\sin\zeta_{FR} \cos\lambda_{FR} \\ \cos\zeta_{FR} \cos\lambda_{FR} \\ 0 \end{bmatrix} - \frac{h_{FR}}{v_{FR} r_f^3} \mathbf{r}_{sc}(t_{FR}) r_f \begin{bmatrix} -\sin\zeta_{FR} \cos\lambda_{FR} \\ \cos\zeta_{FR} \cos\lambda_{FR} \\ 0 \end{bmatrix} \tag{C.56}$$

$$\frac{\partial c_4}{\partial \zeta_f} = \mathbf{A}_{df} r_f \begin{bmatrix} -\sin\zeta_f \cos\lambda_f \\ \cos\zeta_f \cos\lambda_f \\ 0 \end{bmatrix} \tag{C.57}$$

$$\frac{\partial c_7}{\partial \zeta_f} = \frac{\mathbf{v}_f \times \mathbf{h}_f}{r_f v_f h_f} r_f \begin{bmatrix} -\sin\zeta_f \cos\lambda_f \\ \cos\zeta_f \cos\lambda_f \\ 0 \end{bmatrix} - \frac{h_f}{v_f r_f^3} \mathbf{r}_{sc}(t_f) r_f \begin{bmatrix} -\sin\zeta_f \cos\lambda_f \\ \cos\zeta_f \cos\lambda_f \\ 0 \end{bmatrix} \tag{C.58}$$

$$\frac{\partial c_1}{\partial \mathbf{v}_0} = \mathbf{B}_{c0}, \qquad \frac{\partial c_2}{\partial \mathbf{v}_0} = \mathbf{D}_{c0}, \qquad \frac{\partial c_3}{\partial \mathbf{v}_0} = \mathbf{B}_{a0} \tag{C.59}$$

$$\frac{\partial c_5}{\partial \mathbf{v}_0} = \frac{\mathbf{h}_0 \times \mathbf{r}_{sc}(t_0)}{h_0 r_0 v_0} - \frac{h_0}{r_0 v_0^3} \mathbf{v}_0 \tag{C.60}$$

$$\frac{\partial c_3}{\partial \Delta \mathbf{v}_c} = \mathbf{B}_{ac} \tag{C.61}$$

$$\frac{\partial c_1}{\partial \mathbf{v}_{FR}} = -\mathbf{B}_{cFR} \tag{C.62}$$

$$\frac{\partial c_2}{\partial \mathbf{v}_{FR}} = -\mathbf{D}_{cFR} \tag{C.63}$$

$$\frac{\partial c_6}{\partial \mathbf{v}_{FR}} = \frac{\mathbf{h}_{FR} \times \mathbf{r}_{sc}(t_{FR})}{h_{FR} r_f v_{FR}} - \frac{h_{FR}}{r_f v_{FR}^3} \mathbf{v}_{FR} \tag{C.64}$$

$$\frac{\partial c_4}{\partial \mathbf{v}_f} = -\mathbf{B}_{df} \tag{C.65}$$

$$\frac{\partial c_7}{\partial \mathbf{v}_f} = \frac{\mathbf{h}_f \times \mathbf{r}_{sc}(t_f)}{h_f r_f v_f} - \frac{h_f}{r_f v_f^3} \mathbf{v}_f \tag{C.66}$$

Appendix D

Determining the Lunar Flyby State

This appendix pertains to the chapter on utilizing a Lunar flyby to enter into an FRT for NEA rendezvous (Chapter 5). The targeting algorithm described in Section 5.3.2.1 iterates on two spherical angles , ϕ and λ, at Lunar flyby. The following routine is used to determine the state at Lunar flyby given these two angles and the incoming velocity vector of the spacecraft.

1. Calculate the incoming hyperbolic excess velocity from the Earth-to-Moon segment:

$$\mathbf{v}_{\infty}^{-} = \mathbf{v}_{sc}^{-} - \mathbf{v}_{moon} \tag{D.1}$$

2. Calculate the flyby direction and angular momentum direction with respect to the moon:

$$\hat{\mathbf{r}}_p = \begin{bmatrix} \cos\phi\cos\lambda \\ \cos\phi\sin\lambda \\ \sin\phi \end{bmatrix}, \qquad \hat{\mathbf{h}} = \frac{\hat{\mathbf{r}}_p \times \mathbf{v}_{\infty}^{-}}{|\hat{\mathbf{r}}_p \times \mathbf{v}_{\infty}^{-}|} \tag{D.2}$$

3. Find the turning angle δ by which the velocity vector is rotated through the flyby:

$$\delta = \pi - 2\cos^{-1}\left(\frac{\hat{\mathbf{r}}_p \cdot \mathbf{v}_{\infty}^{-}}{|\mathbf{v}_{\infty}^{-}|}\right) \tag{D.3}$$

4. Using an axis-angle rotation scheme, rotate the $\mathbf{v}_{\infty}^{-}$ vector about the $\hat{\mathbf{h}}$ vector by angle δ to obtain $\mathbf{v}_{\infty}^{+}$.

5. With angle δ, the magnitude of the close approach flyby radius may be found:

$$e = \frac{1}{\sin(\delta/2)} \quad \Rightarrow \quad |\mathbf{r}_p| = \frac{\mu_{moon}(e-1)}{|\mathbf{v}_\infty^-|^2} \tag{D.4}$$

6. Obtain the energy E, semimajor axis a, and angular momentum h magnitudes of the flyby:

$$E = \frac{|\mathbf{v}_\infty^-|^2}{2}, \qquad a = \frac{-\mu_{moon}}{2E}, \qquad h = \sqrt{\mu_{moon} a(1-e^2)} \tag{D.5}$$

7. Finally, obtain the speed at close approach from the close approach distance and angular momentum:

$$|\mathbf{v}_p| = \frac{h}{|\mathbf{r}_p|} \quad \Rightarrow \quad \mathbf{r}_p = |\mathbf{r}_p| \begin{bmatrix} \cos\phi\cos\lambda \\ \cos\phi\sin\lambda \\ \sin\phi \end{bmatrix}, \quad \mathbf{v}_p = |\mathbf{v}_p| \frac{\mathbf{v}_\infty^+ + \mathbf{v}_\infty^-}{|\mathbf{v}_\infty^+ + \mathbf{v}_\infty^-|} \tag{D.6}$$

Appendix E

Analytical Gradients for the Lunar Flyby Problem

For the chapter on utilizing a Lunar flyby to enter into an FRT for NEA rendezvous (Chapter 5), this appendix gives the analytical gradients of the cost function and constraints with respect to the problem parameters. These gradients are calculated using the variational equations given in Eq. (3.13) with the numerical integration of the state transition matrix given in Eq. (3.12). Each term in the equality and inequality constraint vectors ($\mathbf{c}$ and $\mathbf{d}$ in Eq. (5.1), respectively) is given a subscript here for brevity; e.g. the n^{th} term listed in the inequality constraint vector is shown here as $\mathbf{d}_n$.

Additionally, the state transition matrix is divided into four 3×3 submatrices, so that the state transition matrix from t_a to t_b is denoted as:

$$\mathbf{\Phi}_{ba} = \left[\begin{array}{c|c} \mathbf{A}_{ba} & \mathbf{B}_{ba} \\ \hline \mathbf{C}_{ba} & \mathbf{D}_{ba} \end{array}\right]$$

Analytical gradients are given in the following equations. All gradients are given for the cost function, and non-zero gradients are given for the inequality and equality constraints. Define $\Delta\mathbf{v}_a$ as the vector difference between the asteroid and the spacecraft at t_a and $\Delta\mathbf{v}_d$ as the vector difference between the asteroid and the spacecraft at t_d. Define $\mathbf{g}$ as the acceleration vector at a given time.

E.1 Cost function gradients

$$\frac{\partial J}{\partial t_0} = 0 \qquad \frac{\partial J}{\partial t_m} = 0 \qquad \frac{\partial J}{\partial t_{SOI}} = \frac{\Delta \mathbf{v}_a^\top}{\Delta v_a} \left(\mathbf{C}_{as} \mathbf{v}_{SOI} + \mathbf{D}_{as} \mathbf{g}(t_{SOI}) \right)$$

$$\frac{\partial J}{\partial t_c} = -\frac{\Delta \mathbf{v}_a^\top}{\Delta v_a} \left(\mathbf{C}_{ac} \left(\mathbf{v}^-(t_c) - \mathbf{v}^+(t_c) \right) \right) \qquad \frac{\partial J}{\partial t_a} = \frac{\Delta \mathbf{v}_a^\top}{\Delta v_a} \left(\mathbf{g}_a(t_a) - \mathbf{g}_{sc}(t_a) \right)$$

$$\frac{\partial J}{\partial t_d} = \frac{\Delta \mathbf{v}_d^\top}{\Delta v_d} \left(\mathbf{g}_{sc}(t_d) - \mathbf{g}_a(t_d) \right) \qquad \frac{\partial J}{\partial t_{FR}} = 0 \qquad \frac{\partial J}{\partial t_f} = -\frac{\Delta \mathbf{v}_d^\top}{\Delta v_d} \left(\mathbf{C}_{df} \mathbf{v}_f + \mathbf{D}_{df} \mathbf{g}(t_f) \right)$$

$$\frac{\partial J}{\partial i_0} = 0 \qquad \frac{\partial J}{\partial \Omega_0} = 0 \qquad \frac{\partial J}{\partial \nu_0} = 0$$

$$\frac{\partial J}{\partial \phi_{SOI}} = \frac{\Delta \mathbf{v}_a^\top}{\Delta v_a} \left(-\mathbf{C}_{as} r_{SOI} \begin{bmatrix} -\cos\lambda_{SOI} \sin\phi_{SOI} \\ -\sin\lambda_{SOI} \sin\phi_{SOI} \\ \cos\phi_{SOI} \end{bmatrix} \right) \qquad \frac{\partial J}{\partial \phi_{FR}} = 0$$

$$\frac{\partial J}{\partial \phi_f} = \frac{\Delta \mathbf{v}_d^\top}{\Delta v_d} \left(\mathbf{C}_{df} r_f \begin{bmatrix} -\cos\lambda_f \sin\phi_f \\ -\sin\lambda_f \sin\phi_f \\ \cos\phi_f \end{bmatrix} \right)$$

$$\frac{\partial J}{\partial \lambda_{SOI}} = \frac{\Delta \mathbf{v}_a^\top}{\Delta v_a} \left(-\mathbf{C}_{as} r_{SOI} \begin{bmatrix} -\sin\lambda_{SOI} \cos\phi_{SOI} \\ \cos\lambda_{SOI} \cos\phi_{SOI} \\ 0 \end{bmatrix} \right) \qquad \frac{\partial J}{\partial \lambda_{FR}} = 0$$

$$\frac{\partial J}{\partial \lambda_f} = \frac{\Delta \mathbf{v}_d^\top}{\Delta v_d} \left(\mathbf{C}_{df} r_f \begin{bmatrix} -\sin\lambda_f \cos\phi_f \\ \cos\lambda_f \cos\phi_f \\ 0 \end{bmatrix} \right) \qquad \frac{\partial J}{\partial \mathbf{r}_m} = 0$$

$$\frac{\partial J}{\partial \Delta v_0} = 1 \qquad \frac{\partial J}{\partial \mathbf{v}_m} = \mathbf{0}_{3\times 1} \qquad \frac{\partial J}{\partial \mathbf{v}_{SOI}} = -\frac{\Delta \mathbf{v}_a^\top}{\Delta v_a} \mathbf{D}_{as}$$

$$\frac{\partial J}{\partial \Delta \mathbf{v}_c} = \frac{\Delta \mathbf{v}_c^\top}{\Delta v_c} - \frac{\Delta \mathbf{v}_a^\top}{\Delta v_a} \mathbf{D}_{ac} \qquad \frac{\partial J}{\partial \mathbf{v}_{FR}} = \mathbf{0}_{3\times 1} \qquad \frac{\partial J}{\partial \mathbf{v}_f} = \frac{\Delta \mathbf{v}_d^\top}{\Delta v_d} \mathbf{D}_{df}$$

E.2 Inequality constraint gradients

$$\frac{\partial \mathbf{d}_1}{\partial t_0} = 1 \qquad \frac{\partial \mathbf{d}_2}{\partial t_0} = -1 \qquad \frac{\partial \mathbf{d}_2}{\partial t_m} = 1 \qquad \frac{\partial \mathbf{d}_3}{\partial t_m} = -1 \qquad \frac{\partial \mathbf{d}_3}{\partial t_{SOI}} = 1$$

$$\frac{\partial \mathbf{d}_4}{\partial t_c} = -1 \qquad \frac{\partial \mathbf{d}_4}{\partial t_a} = 1 \qquad \frac{\partial \mathbf{d}_5}{\partial t_c} = -1 \qquad \frac{\partial \mathbf{d}_5}{\partial t_{FR}} = 1 \qquad \frac{\partial \mathbf{d}_6}{\partial t_d} = -1 \qquad \frac{\partial \mathbf{d}_6}{\partial t_f} = 1$$

$$\frac{\partial \mathbf{d}_7}{\partial t_{SOI}} = -1 \qquad \frac{\partial \mathbf{d}_7}{\partial t_c} = 1 \qquad \frac{\partial \mathbf{d}_8}{\partial t_a} = -1 \qquad \frac{\partial \mathbf{d}_8}{\partial t_d} = 1 \qquad \frac{\partial \mathbf{d}_9}{\partial t_0} = 1 \qquad \frac{\partial \mathbf{d}_9}{\partial t_{FR}} = -1$$

$$\frac{\partial \mathbf{d}_{10}}{\partial \mathbf{r}_m} = \frac{\mathbf{r}_m^\top}{r_m} \qquad \frac{\partial \mathbf{d}_{11}}{\partial \mathbf{v}_{FR}} = -\frac{\mathbf{v}_{FR}^\top}{v_{FR}} \qquad \frac{\partial \mathbf{d}_{12}}{\partial \mathbf{v}_f} = -\frac{\mathbf{v}_f^\top}{v_f}$$

E.3 Equality constraint gradients

$$\frac{\partial \mathbf{c}_1}{\partial t_0} = \mathbf{A}_{10}\mathbf{v}_{sc}(t_0) + \mathbf{B}_{10}\mathbf{g}_{sc}(t_0)$$

$$\frac{\partial \mathbf{c}_1}{\partial t_m} = -\mathbf{A}_{1m}\mathbf{v}_m - \mathbf{B}_{1m}\mathbf{g}_{sc}(t_m) + \left(\mathbf{v}_{sc}^{+}(t_1) - \mathbf{v}_{sc}^{-}(t_1)\right) + \mathbf{A}_{1m}\mathbf{v}_{moon}(t_m) + \mathbf{B}_{1m}\mathbf{g}_{moon}(t_m)$$

$$\frac{\partial \mathbf{c}_1}{\partial i_0} = -\mathbf{A}_{10} r_0 \begin{bmatrix} \sin(-\Omega_0)\sin(-i_0)\sin(\nu_0) \\ \cos(-\Omega_0)\sin(-i_0)\sin(\nu_0) \\ \cos(-i_0)\sin(\nu_0) \end{bmatrix} - \ldots$$

$$\ldots \mathbf{B}_{10}\left[\mathbf{I}_{3\times 3}\left(1 + \frac{\Delta v_0}{|\mathbf{v}_{LEO}|}\right) - \frac{\Delta v_0 \mathbf{v}_{LEO}\mathbf{v}_{LEO}^{\top}}{|\mathbf{v}_{LEO}|^3}\right]|\mathbf{v}_{LEO}| \begin{bmatrix} \sin(-\Omega_0)\sin(-i_0)\cos(\nu_0) \\ \cos(-\Omega_0)\sin(-i_0)\cos(\nu_0) \\ \cos(-i_0)\cos(\nu_0) \end{bmatrix}$$

$$\frac{\partial \mathbf{c}_1}{\partial \Omega_0} = -\mathbf{A}_{10} r_0 \begin{bmatrix} \sin(-\Omega_0)\cos(\nu_0) - \cos(-\Omega_0)\cos(-i_0)\sin(\nu_0) \\ \cos(-\Omega_0)\cos(\nu_0) + \sin(-\Omega_0)\cos(-i_0)\sin(\nu_0) \\ 0 \end{bmatrix} - \ldots$$

$$\ldots \mathbf{B}_{10}\left[\mathbf{I}_{3\times 3}\left(1 + \frac{\Delta v_0}{|\mathbf{v}_{LEO}|}\right) - \frac{\Delta v_0 \mathbf{v}_{LEO}\mathbf{v}_{LEO}^{\top}}{|\mathbf{v}_{LEO}|^3}\right]|\mathbf{v}_{LEO}| \ldots$$

$$\ldots \begin{bmatrix} -\sin(-\Omega_0)\sin(\nu_0) - \cos(-\Omega_0)\cos(-i_0)\cos(\nu_0) \\ -\cos(-\Omega_0)\sin(\nu_0) + \sin(-\Omega_0)\cos(-i_0)\cos(\nu_0) \\ 0 \end{bmatrix}$$

$$\frac{\partial \mathbf{c}_1}{\partial \nu_0} = -\mathbf{A}_{10} r_0 \begin{bmatrix} -\cos(-\Omega_0)\sin(\nu_0) + \sin(-\Omega_0)\cos(-i_0)\cos(\nu_0) \\ \sin(-\Omega_0)\sin(\nu_0) + \cos(-\Omega_0)\cos(-i_0)\cos(\nu_0) \\ -\sin -i_0 \cos \nu_0 \end{bmatrix} - \ldots$$

$$\ldots \mathbf{B}_{10}\left[\mathbf{I}_{3\times 3}\left(1 + \frac{\Delta v_0}{|\mathbf{v}_{LEO}|}\right) - \frac{\Delta v_0 \mathbf{v}_{LEO}\mathbf{v}_{LEO}^{\top}}{|\mathbf{v}_{LEO}|^3}\right]|\mathbf{v}_{LEO}| \ldots$$

$$\ldots \begin{bmatrix} -\cos(-\Omega_0)\cos(\nu_0) - \sin(-\Omega_0)\cos(-i_0)\sin(\nu_0) \\ \sin(-\Omega_0)\cos(\nu_0) - \cos(-\Omega_0)\cos(-i_0)\sin(\nu_0) \\ \sin -i_0 \sin \nu_0 \end{bmatrix}$$

$$\frac{\partial \mathbf{c}_1}{\partial \mathbf{r}_m} = \mathbf{A}_{1m} \qquad \frac{\partial \mathbf{c}_1}{\partial \Delta v_0} = -\mathbf{B}_{10}\frac{\mathbf{v}_{LEO}}{|\mathbf{v}_{LEO}|} \qquad \frac{\partial \mathbf{c}_1}{\partial \mathbf{v}_m} = \mathbf{B}_{1m}$$

$$\frac{\partial \mathbf{c}_2}{\partial t_m} = \mathbf{A}_{2m}\mathbf{v}_m + \mathbf{B}_{2m}\mathbf{g}_{sc}(t_m) + \left(\mathbf{v}_{sc}^{+}(t_2) - \mathbf{v}_{sc}^{-}(t_2)\right) - \mathbf{A}_{2m}\mathbf{v}_{moon}(t_m) - \mathbf{B}_{2m}\mathbf{g}_{moon}(t_m)$$

$$\frac{\partial \mathbf{c}_2}{\partial t_{SOI}} = -\mathbf{A}_{2SOI}\mathbf{v}_{SOI} - \mathbf{B}_{2SOI}\mathbf{g}_{sc}(t_{SOI})$$

$$\frac{\partial \mathbf{c}_2}{\partial \phi_{SOI}} = \mathbf{A}_{2SOI} r_{SOI} \begin{bmatrix} -\cos(\lambda_{SOI})\sin(\phi_{SOI}) \\ -\sin(\lambda_{SOI})\sin(\phi_{SOI}) \\ \cos(\phi_{SOI}) \end{bmatrix}$$

$$\frac{\partial \mathbf{c}_2}{\partial \lambda_{SOI}} = \mathbf{A}_{2SOI} r_{SOI} \begin{bmatrix} -\sin(\lambda_{SOI})\cos(\phi_{SOI}) \\ \cos(\lambda_{SOI})\cos(\phi_{SOI}) \\ 0 \end{bmatrix}$$

$$\frac{\partial \mathbf{c}_2}{\partial \mathbf{r}_m} = -\mathbf{A}_{2m} \qquad \frac{\partial \mathbf{c}_2}{\partial \mathbf{v}_m} = -\mathbf{B}_{2m} \qquad \frac{\partial \mathbf{c}_2}{\partial \mathbf{v}_{SOI}} = \mathbf{B}_{2SOI}$$

$$\frac{\partial \mathbf{c}_3}{\partial t_{SOI}} = -\mathbf{A}_{cSOI}\mathbf{v}_{SOI} - \mathbf{B}_{cSOI}\mathbf{g}_{sc}(t_{SOI}) \qquad \frac{\partial \mathbf{c}_3}{\partial t_c} = \mathbf{v}_{sc}^{-}(t_c) - \mathbf{v}_{sc}^{+}(t_c)$$

$$\frac{\partial \mathbf{c}_3}{\partial t_{FR}} = \mathbf{A}_{cFR}\mathbf{v}_{sc}(t_{FR}) + \mathbf{B}_{cFR}\mathbf{g}_{sc}(t_{FR})$$

$$\frac{\partial \mathbf{c}_3}{\partial \phi_{SOI}} = \mathbf{A}_{cSOI} r_{SOI} \begin{bmatrix} -\cos(\lambda_{SOI})\sin(\phi_{SOI}) \\ -\sin(\lambda_{SOI})\sin(\phi_{SOI}) \\ \cos(\phi_{SOI}) \end{bmatrix}$$

$$\frac{\partial \mathbf{c}_3}{\partial \phi_{FR}} = -\mathbf{A}_{cFR} r_{FR} \begin{bmatrix} -\cos(\lambda_{FR})\sin(\phi_{FR}) \\ -\sin(\lambda_{FR})\sin(\phi_{FR}) \\ \cos(\phi_{FR}) \end{bmatrix}$$

$$\frac{\partial \mathbf{c}_3}{\partial \lambda_{SOI}} = \mathbf{A}_{cSOI} r_{SOI} \begin{bmatrix} -\sin(\lambda_{SOI})\cos(\phi_{SOI}) \\ \cos(\lambda_{SOI})\cos(\phi_{SOI}) \\ 0 \end{bmatrix}$$

$$\frac{\partial \mathbf{c}_3}{\partial \lambda_{FR}} = -\mathbf{A}_{cFR} r_{FR} \begin{bmatrix} -\sin(\lambda_{FR})\cos(\phi_{FR}) \\ \cos(\lambda_{FR})\cos(\phi_{FR}) \\ 0 \end{bmatrix}$$

$$\frac{\partial \mathbf{c}_3}{\partial \mathbf{v}_{SOI}} = \mathbf{B}_{cSOI} \qquad \frac{\partial \mathbf{c}_3}{\partial \mathbf{v}_{FR}} = -\mathbf{B}_{cFR}$$

$$\frac{\partial \mathbf{c}_4}{\partial t_{SOI}} = -\mathbf{A}_{aSOI}\mathbf{v}_{SOI} - \mathbf{B}_{aSOI}\mathbf{g}_{sc}(t_{SOI}) \qquad \frac{\partial \mathbf{c}_4}{\partial t_c} = \mathbf{A}_{ac}\left(\mathbf{v}_{sc}^{-}(t_c) - \mathbf{v}_{sc}^{+}(t_c)\right)$$

$$\frac{\partial \mathbf{c}_4}{\partial t_a} = \mathbf{v}_{sc}(t_a) - \mathbf{v}_a(t_a) \qquad \frac{\partial \mathbf{c}_4}{\partial \phi_{SOI}} = \mathbf{A}_{as}\mathbf{r}_{SOI} \begin{bmatrix} -\cos(\lambda_{SOI})\sin(\phi_{SOI}) \\ -\sin(\lambda_{SOI})\sin(\phi_{SOI}) \\ \cos(\phi_{SOI}) \end{bmatrix}$$

$$\frac{\partial \mathbf{c}_4}{\partial \lambda_{SOI}} = \mathbf{A}_{as}\mathbf{r}_{SOI} \begin{bmatrix} -\sin(\lambda_{SOI})\cos(\phi_{SOI}) \\ \cos(\lambda_{SOI})\cos(\phi_{SOI}) \\ 0 \end{bmatrix}$$

$$\frac{\partial \mathbf{c}_4}{\partial \mathbf{v}_{SOI}} = \mathbf{B}_{as} \qquad \frac{\partial \mathbf{c}_4}{\partial \Delta\mathbf{v}_c} = \mathbf{B}_{ac}$$

$$\frac{\partial \mathbf{c}_5}{\partial t_d} = \mathbf{v}_{sc}(t_d) - \mathbf{v}_a(t_d) \qquad \frac{\partial \mathbf{c}_5}{\partial t_f} = -\mathbf{A}_{df}\mathbf{v}_f - \mathbf{B}_{df}\mathbf{g}_{sc}(t_f)$$

$$\frac{\partial \mathbf{c}_5}{\partial \phi_f} = \mathbf{A}_{df} r_f \begin{bmatrix} -\cos(\lambda_f)\sin(\phi_f) \\ -\sin(\lambda_f)\sin(\phi_f) \\ \cos(\phi_f) \end{bmatrix}$$

$$\frac{\partial \mathbf{c}_5}{\partial \lambda_f} = \mathbf{A}_{df} r_f \begin{bmatrix} -\sin(\lambda_f)\cos(\phi_f) \\ \cos(\lambda_f)\cos(\phi_f) \\ 0 \end{bmatrix} \qquad \frac{\partial \mathbf{c}_5}{\partial \mathbf{v}_f} = \mathbf{B}_{df}$$

$$\frac{\partial \mathbf{c}_6}{\partial t_0} = \mathbf{C}_{10}\mathbf{v}_0 + \mathbf{D}_{10}\mathbf{g}_{sc}(t_0)$$

$$\frac{\partial \mathbf{c}_6}{\partial t_m} = -\mathbf{C}_{1m}\mathbf{v}_m - \mathbf{D}_{1m}\mathbf{g}_{sc}(t_m) + \left(\mathbf{g}_{sc}^{+}(t_1) - \mathbf{g}_{sc}^{-}(t_1)\right) + \mathbf{C}_{1m}\mathbf{v}_{moon}(t_m) + \mathbf{D}_{1m}\mathbf{g}_{moon}(t_m)$$

$$\frac{\partial \mathbf{c}_6}{\partial i_0} = -\mathbf{C}_{10} r_0 \begin{bmatrix} \sin(-\Omega_0)\sin(-i_0)\sin(\nu_0) \\ \cos(-\Omega_0)\sin(-i_0)\sin(\nu_0) \\ \cos(-i_0)\sin(\nu_0) \end{bmatrix} - \ldots$$

$$\ldots \mathbf{D}_{10}\left[\mathbf{I}_{3\times 3}\left(1 + \frac{\Delta v_0}{|\mathbf{v}_{LEO}|}\right) - \frac{\Delta v_0 \mathbf{v}_{LEO}\mathbf{v}_{LEO}^{\top}}{|\mathbf{v}_{LEO}|^3}\right]|\mathbf{v}_{LEO}| \begin{bmatrix} \sin(-\Omega_0)\sin(-i_0)\cos(\nu_0) \\ \cos(-\Omega_0)\sin(-i_0)\cos(\nu_0) \\ \cos(-i_0)\cos(\nu_0) \end{bmatrix}$$

$$\frac{\partial \mathbf{c}_6}{\partial \Omega_0} = -\mathbf{C}_{10} r_0 \begin{bmatrix} \sin(-\Omega_0)\cos(\nu_0) - \cos(-\Omega_0)\cos(-i_0)\sin(\nu_0) \\ \cos(-\Omega_0)\cos(\nu_0) + \sin(-\Omega_0)\cos(-i_0)\sin(\nu_0) \\ 0 \end{bmatrix} - \ldots$$

$$\ldots \mathbf{D}_{10}\left[\mathbf{I}_{3\times 3}\left(1 + \frac{\Delta v_0}{|\mathbf{v}_{LEO}|}\right) - \frac{\Delta v_0 \mathbf{v}_{LEO}\mathbf{v}_{LEO}^{\top}}{|\mathbf{v}_{LEO}|^3}\right]|\mathbf{v}_{LEO}| \ldots$$

$$\ldots \begin{bmatrix} -\sin(-\Omega_0)\sin(\nu_0) - \cos(-\Omega_0)\cos(-i_0)\cos(\nu_0) \\ -\cos(-\Omega_0)\sin(\nu_0) + \sin(-\Omega_0)\cos(-i_0)\cos(\nu_0) \\ 0 \end{bmatrix}$$

$$\frac{\partial \mathbf{c}_6}{\partial \nu_0} = -\mathbf{C}_{10} r_0 \begin{bmatrix} -\cos(-\Omega_0)\sin(\nu_0) + \sin(-\Omega_0)\cos(-i_0)\cos(\nu_0) \\ \sin(-\Omega_0)\sin(\nu_0) + \cos(-\Omega_0)\cos(-i_0)\cos(\nu_0) \\ -\sin -i_0 \cos \nu_0 \end{bmatrix} - \ldots$$

$$\ldots \mathbf{D}_{10} \left[\mathbf{I}_{3\times 3} \left(1 + \frac{\Delta v_0}{|\mathbf{v}_{LEO}|} \right) - \frac{\Delta v_0 \mathbf{v}_{LEO} \mathbf{v}_{LEO}^\top}{|\mathbf{v}_{LEO}|^3} \right] |\mathbf{v}_{LEO}| \ldots$$

$$\ldots \begin{bmatrix} -\cos(-\Omega_0)\cos(\nu_0) - \sin(-\Omega_0)\cos(-i_0)\sin(\nu_0) \\ \sin(-\Omega_0)\cos(\nu_0) - \cos(-\Omega_0)\cos(-i_0)\sin(\nu_0) \\ \sin -i_0 \sin \nu_0 \end{bmatrix}$$

$$\frac{\partial \mathbf{c}_6}{\partial \mathbf{r}_m} = \mathbf{C}_{1m} \qquad \frac{\partial \mathbf{c}_6}{\partial \Delta v_0} = -\mathbf{D}_{10} \frac{\mathbf{v}_{LEO}}{|\mathbf{v}_{LEO}|} \qquad \frac{\partial \mathbf{c}_6}{\partial \mathbf{v}_m} = \mathbf{D}_{1m}$$

$$\frac{\partial \mathbf{c}_7}{\partial t_m} = \mathbf{C}_{2m}\mathbf{v}_m + \mathbf{D}_{2m}\mathbf{g}_{sc}(t_m) + \left(\mathbf{g}_{sc}^+(t_2) - \mathbf{g}_{sc}^-(t_2)\right) - \mathbf{C}_{2m}\mathbf{v}_{moon}(t_m) - \mathbf{D}_{2m}\mathbf{g}_{moon}(t_m)$$

$$\frac{\partial \mathbf{c}_7}{\partial t_{SOI}} = -\mathbf{C}_{2SOI}\mathbf{v}_{SOI} - \mathbf{D}_{2SOI}\mathbf{g}_{sc}(t_{SOI})$$

$$\frac{\partial \mathbf{c}_7}{\partial \phi_{SOI}} = \mathbf{C}_{2SOI} r_{SOI} \begin{bmatrix} -\cos(\lambda_{SOI})\sin(\phi_{SOI}) \\ -\sin(\lambda_{SOI})\sin(\phi_{SOI}) \\ \cos(\phi_{SOI}) \end{bmatrix}$$

$$\frac{\partial \mathbf{c}_7}{\partial \lambda_{SOI}} = \mathbf{C}_{2SOI} r_{SOI} \begin{bmatrix} -\sin(\lambda_{SOI})\cos(\phi_{SOI}) \\ \cos(\lambda_{SOI})\cos(\phi_{SOI}) \\ 0 \end{bmatrix}$$

$$\frac{\partial \mathbf{c}_7}{\partial \mathbf{r}_m} = -\mathbf{C}_{2m} \qquad \frac{\partial \mathbf{c}_7}{\partial \mathbf{v}_m} = -\mathbf{D}_{2m} \qquad \frac{\partial \mathbf{c}_7}{\partial \mathbf{v}_{SOI}} = \mathbf{D}_{2SOI}$$

$$\frac{\partial \mathbf{c}_8}{\partial t_{SOI}} = -\mathbf{C}_{cSOI}\mathbf{v}_{SOI} - \mathbf{D}_{cSOI}\mathbf{g}_{sc}(t_{SOI}) \qquad \frac{\partial \mathbf{c}_8}{\partial t_c} = \mathbf{g}_{sc}^{-}(t_c) - \mathbf{g}_{sc}^{+}(t_c)$$

$$\frac{\partial \mathbf{c}_8}{\partial t_{FR}} = \mathbf{C}_{cFR}\mathbf{v}_{sc}(t_{FR}) + \mathbf{D}_{cFR}\mathbf{g}_{sc}(t_{FR})$$

$$\frac{\partial \mathbf{c}_8}{\partial \phi_{SOI}} = \mathbf{C}_{cSOI} r_{SOI} \begin{bmatrix} -\cos(\lambda_{SOI})\sin(\phi_{SOI}) \\ -\sin(\lambda_{SOI})\sin(\phi_{SOI}) \\ \cos(\phi_{SOI}) \end{bmatrix}$$

$$\frac{\partial \mathbf{c}_8}{\partial \phi_{FR}} = -\mathbf{C}_{cFR} r_{FR} \begin{bmatrix} -\cos(\lambda_{FR})\sin(\phi_{FR}) \\ -\sin(\lambda_{FR})\sin(\phi_{FR}) \\ \cos(\phi_{FR}) \end{bmatrix}$$

$$\frac{\partial \mathbf{c}_8}{\partial \lambda_{SOI}} = \mathbf{C}_{cSOI} r_{SOI} \begin{bmatrix} -\sin(\lambda_{SOI})\cos(\phi_{SOI}) \\ \cos(\lambda_{SOI})\cos(\phi_{SOI}) \\ 0 \end{bmatrix}$$

$$\frac{\partial \mathbf{c}_8}{\partial \lambda_{FR}} = -\mathbf{C}_{cFR} r_{FR} \begin{bmatrix} -\sin(\lambda_{FR})\cos(\phi_{FR}) \\ \cos(\lambda_{FR})\cos(\phi_{FR}) \\ 0 \end{bmatrix}$$

$$\frac{\partial \mathbf{c}_8}{\partial \mathbf{v}_{SOI}} = \mathbf{D}_{cSOI} \qquad \frac{\partial \mathbf{c}_8}{\partial \mathbf{v}_{FR}} = -\mathbf{D}_{cFR}$$

Appendix F

Obtaining Flyby States for the Continuation Problem

This appendix details the process of obtaining the body flyby states from the solutions of Lambert's problem for a ZSOI flyby problem (Chapter 6). The approach taken here differs slightly depending on whether the encounter is an intermediate encounter (with both an incoming and departing leg) or a terminal encounter (with only an incoming or outgoing leg, but not both), and each case is detailed separately.

F.1 Finding the close approach flyby state at an intermediate encounter

With an appropriate initial guess in the ZSOI model, the spacecraft's pre- and post-flyby states are known at each intermediate encounter with respect to the central body, and the $\mathbf{v}_\infty$ vectors may be found. Denote $\mathbf{v}_\infty^-$ as the hyperbolic excess velocity before the flyby, and $\mathbf{v}_\infty^+$ as the hyperbolic excess velocity vector after the flyby, with the same magnitude as $\mathbf{v}_\infty^-$.

Figure F.1 shows the vectors and geometry for the flyby in a reference frame fixed with the intermediate body, where $\mathbf{r}_p$ and $\mathbf{v}_p$ are the periapsis position and velocity vectors, respectively.

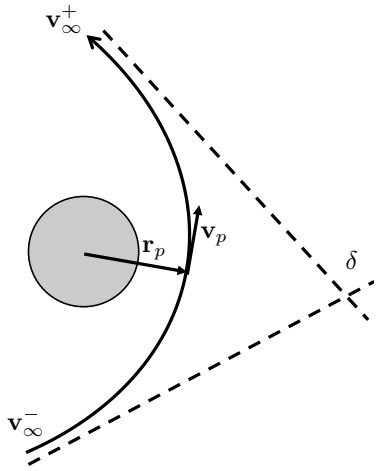

Figure F.1: Schematic of a flyby for an intermediate encounter

The turning angle δ and eccentricity e of the flyby are found in Eq. (F.1) by using the dot product of the two $\mathbf{v}_\infty$ vectors, assuming an initial guess where the magnitude of the $\mathbf{v}_\infty$ vectors are equal.

$$\delta = \cos^{-1}\left(\frac{\mathbf{v}_\infty^- \cdot \mathbf{v}_\infty^+}{|\mathbf{v}_\infty|^2}\right) \qquad e = \frac{1}{\sin(\delta/2)} \tag{F.1}$$

The unit direction of the position of the periapsis location with respect to the flyby body may be found by using just the two $\mathbf{v}_\infty$ vectors:

$$\hat{r}_p = \frac{\mathbf{v}_\infty^- - \mathbf{v}_\infty^+}{|\mathbf{v}_\infty^- - \mathbf{v}_\infty^+|} \tag{F.2}$$

The representation for the direction of the $\hat{v}_p$ vector is found first by calculating the direction of the angular momentum vector, which is orthogonal to the plane of the flyby, and therefore orthogonal to the two $\mathbf{v}_\infty$ vectors:

$$\hat{h} = \frac{\mathbf{v}_\infty^- \times \mathbf{v}_\infty^+}{|\mathbf{v}_\infty^- \times \mathbf{v}_\infty^+|} \tag{F.3}$$

At periapsis, the velocity vector is perpendicular to the position vector with respect to the flyby body. The unit direction of this velocity vector is orthogonal to both the periapsis position and the angular momentum, which are both unit vectors:

$$\hat{v}_p = \hat{h} \times \hat{r}_p \tag{F.4}$$

The magnitude of the periapsis position and velocity are found next, using another representation for eccentricity and conservation of energy during the flyby:

$$r_p = \frac{\mu(e-1)}{|\mathbf{v}_\infty|^2} \qquad v_p = \sqrt{|\mathbf{v}_\infty|^2 + \frac{2\mu}{r_p}} \tag{F.5}$$

The full state at the periapsis of the flyby is now given by combining the direction and magnitude information:

$$\mathbf{r}_p = r_p \hat{r}_p \qquad \mathbf{v}_p = v_p \hat{v}_p \tag{F.6}$$

F.2 Finding the initial or final state at a terminal encounter

At a terminal encounter, only an arrival or a departure occurs, and there is only one $\mathbf{v}_\infty$ vector. A different method is employed to calculate an appropriate periapsis state. It is assumed that the magnitude of the position vector is known at initial departure and final rendezvous.

To begin, the angular momentum direction of the spacecraft is found, which is related to the angular momentum direction of the target body $\mathbf{h}_B$. The vector $\mathbf{v}_\infty$ refers to the outgoing hyperbolic velocity vector of the spacecraft relative to the initial body, and the incoming hyperbolic velocity vector for the final body, both of which are known from the initial guess Lambert ZSOI solution. The vectors $\mathbf{r}_B$ and $\mathbf{v}_B$ are the position and velocity of the target body with respect to the central body.

$$\mathbf{h}_B = \mathbf{r}_B \times \mathbf{v}_B \qquad \mathbf{b} = \mathbf{v}_\infty \times \mathbf{h}_B \qquad \Rightarrow \qquad \hat{h} = \frac{\mathbf{b} \times \mathbf{v}_\infty}{|\mathbf{b} \times \mathbf{v}_\infty|} \tag{F.7}$$

The hyperbolic eccentricity and turning angle may be found by using the following two relations, where the initial and final radii (r_p) are known.

$$e = 1 + \frac{r_p \left|\mathbf{v}_\infty\right|^2}{\mu_B} \qquad \delta = 2\sin^{-1}(1/e) \tag{F.8}$$

With an angular momentum direction defined, the periapsis velocity vector direction $\hat{v}_p$ is found by rotating $\mathbf{v}_\infty^-$ by $\delta/2$ about $\hat{h}$ for the initial body (or rotating $\mathbf{v}_\infty^+$ by $-\delta/2$ about $\hat{h}$ for the final body). This rotation may be accomplished with any standard rotation routine that uses an Euler axis and angle.

At periapsis, the velocity vector is orthogonal to the position vector with respect to the flyby body. The direction of this position vector is found by using $\hat{v}_p$ and $\hat{h}$, which are both unit vectors:

$$\hat{r}_p = \hat{v}_p \times \hat{h} \tag{F.9}$$

The magnitude of the periapsis velocity vector is found by using the second equation in Eq. (F.5). Finally, the full state at periapsis is found. Recall that the initial and final radii must be pre-defined by the user.

$$\mathbf{r}_p = r_p \hat{r}_p \qquad \mathbf{v}_p = v_p \hat{v}_p \tag{F.10}$$

Appendix G

Initial Conditions for Free Return Trajectories

The digital archive of this dissertation contains a supplementary text file called `FRT_initial_conditions.txt`. This file contains a library of Free Return Trajectories in the Sun-Earth/Moon three-body problem. The initial conditions are given as position and velocity elements, and each Free Return is listed in order of total time of flight. The header for the file is given below.

```
#-----------------------------------------------------------------
#
# INITIAL CONDITIONS FOR FREE RETURN TRAJECTORIES
#
# These are initial conditions in the J2000 inertial frame,
#    centered at Earth in the CRTBP model.  Gravity of only
#    the Sun and the Earth-Moon combined mass is considered.
# The Sun is at [-1AU,0,0], and the Earth/Moon is at [0,0,0]
#
# Grav. param of Sun = 1.32712440018E11 km^3/s^2
# Grav. param of Earth/Moon = 4.035032405E8 km^3/s^2
# Distance from Sun to Earth/Moon (1AU) = 1.49597870691E8 km
```

```
#
# Columns are:
# 1. ID of FRT (counter from 1)
# 2. Time of flight [days]
# 3. X initial position [km]
# 4. Y initial position [km]
# 5. Z initial position [km]
# 6. X initial velocity [km/s]
# 7. Y initial velocity [km/s]
# 8. Z initial velocity [km/s]
#
#------------------------------------------------------------------------
```

References

[1] Daniel R. Adamo, Jon D. Giorgini, Paul a. Abell, and Rob R. Landis. Asteroid Destinations Accessible for Human Exploration: A Preliminary Survey in Mid-2009. *Journal of Spacecraft and Rockets*, 47(6):994–1002, 2010.

[2] National Aeronautics and Space Administration. Near-Earth Object Human Space Flight Accessible Targets Study (NHATS). Accessible on-line at `http://neo.jpl.nasa.gov/nhats/`. Accessed 10 June 2012.

[3] E. L. Allgower and K. Georg. *Numerical Continuation Methods: An Introduction*. Springer, New York, 1990.

[4] Harwell Subroutine Library Archive. VF13. Oxfordshire, England, 2001. Accessible on-line at `http://www.hsl.rl.ac.uk`. Last accessed 10 June 2014.

[5] Nitin Arora and Ryan P. Russell. A Fast, Accurate, and Smooth Planetary Ephemeris Retrieval System. *Celestial Mechanics and Dynamical Astronomy*, 108(2):107–124, 2010.

[6] Maria Antonietta Barucci, a. F. Cheng, P. Michel, L. a. M. Benner, R. P. Binzel, P. a. Bland, H. Böhnhardt, J. R. Brucato, A. Campo Bagatin, P. Cerroni, E. Dotto, A. Fitzsimmons, I. a. Franchi, S. F. Green, L.-M. Lara, J. Licandro, B. Marty, K. Muinonen, A. Nathues, J. Oberst, a. S. Rivkin, F. Robert,

R. Saladino, J. M. Trigo-Rodriguez, S. Ulamec, and M. Zolensky. MarcoPolo-R Near Earth Asteroid Sample Return Mission. *Experimental Astronomy*, 33(2-3):645–684, 2011.

[7] R. Battin. *An Introduction to the Mathematics and Methods of Astrodynamics, Revised ed.* American Institute of Aeronautics and Astronautics, Reston, VA, 1999.

[8] Ronald L Berry. Launch Window and Translunar, Lunar Orbit, and Transearth Trajectory Planning and Control for the Apollo 11 Lunar Landing Mission. In *Proceedings of the AIAA 8th Aerospace Sciences Meeting*, volume 70-24, pages AIAA paper No. 70–24, 1970.

[9] James Douglas Biggs and Colin McInnes. Solar Sail Formation Flying for Deep-Space Remote Sensing. *Journal of Spacecraft and Rockets*, 46(3):670–678, 2009.

[10] N. Bradley and R. Russell. A Continuation Method for Converting Trajectories from Patched Conics to Full Gravity Models. In review, submitted for publication to the Journal of the Astronautical Sciences. Submitted 30 April, 2014. Minor revisions requested 29 July, 2014.

[11] N. Bradley and R. Russell. A Continuation Method for Converting Trajectories from Patched Conics to Full Gravity Models. In *Proc. 24st AAS/AIAA Space Flight Mechanics Meeting, Santa Fe, New Mexico*, 2014.

[12] Nicholas Bradley, Sonia Hernandez, and Ryan P Russell. Optimized Free-Return Trajectories to Near-Earth Asteroids via Lunar Flyby. In *Proceedings of the AAS/AIAA Astrodynamics Specialist Conference Conference*, pages 3353–3369, 2013.

[13] Nicholas Bradley and Cesar Ocampo. Classification of Distant Earth-Return Trajectories for Near-Earth Asteroid Mission Applications. In *Proceedings of the AAS/AIAA Space Flight Mechanics Meeting*, pages 3231–3250, 2013.

[14] Nicholas Bradley and Cesar Ocampo. Optimal Free-Return Trajectories to Near-Earth Asteroids. *Journal of Guidance, Control, and Dynamics*, 36(5):1346–1355, 2013.

[15] Brent Buffington and Nathan Strange. Patched-Integrated Gravity-Assist Trajectory Design. In *Proceedings of the AIAA/AAS Astrodynamics Specialist Conference*, pages 403–422, 2007.

[16] D. V. Byrnes and H. L. Hooper. Multi-Conic: A Fast and Accurate Method of Computing Space Flight Trajectories. In *Proceedings of the AAS/AIAA Astrodynamics Conference*, number 70, pages AIAA Paper 70–1062, 1970.

[17] J.-B. Caillau, B. Daoud, and J. Gergaud. Minimum Fuel Control of the Planar Circular Restricted Three-Body Problem. *Celestial Mechanics and Dynamical Astronomy*, 114(1-2):137–150, 2012.

[18] S. Campagnola and G. Lantoine. Personal conversations, 29 January 2014, AAS/AIAA Space Flight Mechanics Meeting, Santa Fe, NM.

[19] Stefano Campagnola, Brent B. Buffington, and Anastassios E. Petropoulos. Jovian Tour Design for Orbiter and Lander Missions to Europa. *Acta Astronautica*, 100:68–81, 2014.

[20] Lorenzo Casalino and Francesco Simeoni. Indirect Optimization of Asteroid Deflection Missions with Electric Propulsion. *Journal of Guidance, Control, and Dynamics*, 35(2):423–433, 2012.

[21] Jordi Casoliva, Josep M. Mondelo, Benjamin F. Villac, Kenneth D. Mease, Esther Barrabes, and Merce Olle. Two Classes of Cycler Trajectories in the Earth-Moon System. *Journal of Guidance, Control, and Dynamics*, 33(5):1623–1640, 2010.

[22] Yang Chen, HeXi Baoyin, and JunFeng Li. Design and Optimization of a Trajectory for Moon Departure Near Earth Asteroid Exploration. *Science China Physics, Mechanics and Astronomy*, 54(4):748–755, 2011.

[23] A.V. Chernov. Optimal Flight to Near-Earth Asteroids with using Electric Propulsion and Gravity Maneuvers. In *Proceedings of the 18th International Symposium on Space Flight Dynamics*, volume 548, 2004.

[24] C Channing Chow and Benjamin F. Villac. Mapping Autonomous Constellation Design Spaces Using Numerical Continuation. *Journal of Guidance, Control, and Dynamics*, 35(5):1426–1434, 2012.

[25] Jason C. H. Chuang, Troy D. Goodson, and John Hanson. Multiple-Burn Families of Optimal Low- and Medium-Thrust Orbit Transfers. *Journal of Spacecraft and Rockets*, 36(6):866–874, 1999.

[26] Camilla Colombo, Massimiliano Vasile, and Gianmarco Radice. Optimal Low-Thrust Trajectories to Asteroids through an Algorithm Based on Differential Dynamic Programming. *Celestial Mechanics and Dynamical Astronomy*, 105(1-3):75–112, 2009.

[27] Bruce A Conway. Optimal Low-Thrust Interception of Earth-Crossing Asteroids. *Journal of Guidance, Control, and Dynamics*, 20(5):995–1002, 1997.

[28] PingYuan Cui, Dong Qiao, HuTao Cui, and EnJie Luan. Target Selection and Transfer Trajectories Design for Exploring Asteroid Mission. *Science China Technological Sciences*, 53(4):1150–1158, 2010.

[29] Bret G Drake. Strategic Considerations of Human Exploration of Near- Earth Asteroids. In *Proceedings of the 2012 IEEE Aerospace Conference*, 2012.

[30] R. Duffard, K. Kumar, S. Pirrotta, M. Salatti, M. Kubínyi, U. Derz, R.M.G. Armytage, S. Arloth, L. Donati, A. Duricic, J. Flahaut, S. Hempel, A. Pollinger, and S. Poulsen. A Multiple-Rendezvous, Sample-Return Mission to Two Near-Earth Asteroids. *Advances in Space Research*, 48(1):120–132, 2011.

[31] David W. Dunham and Robert W. Farquhar. Trajectory Design for a Lunar Mapping and Near-Earth-Asteroid Flyby Mission. In *Spaceflight Mechanics Meeting*, pages 605–624, 1993.

[32] David W Dunham, Robert W Farquhar, and James V McAdams. Recent Gravity-Assist Trajectories for Interplanetary and Solar Exploration. In *Annals of the New York Academy of Sciences*, volume 270, pages 254–270. 2005.

[33] Ariel Edery. Designing Phase 2 for the Double-Lunar Swingby of the Magnetospheric Multiscale (MMS) Mission. In *Proc. 13th AAS/AIAA Space Flight Mechanics Meeting*, 2003.

[34] Jacob A Englander, Bruce A Conway, and Trevor Williams. Automated Interplanetary Trajectory Planning. In *Proceedings of the AAS/AIAA Astrodynamics Specialist Conference*, number August, pages 4517–4537, 2012.

[35] R. W. Farquhar and D. W. Dunham. Earth-Return Trajectory Options for the 1985-86 Halley Opportunity. In *Proc. 20th Aerospace Sciences Meeting, Orlando, Florida*, 1982. AIAA Paper 82-0136.

[36] Robert W Farquhar. The Use of Earth-Return Trajectories for Missions to Comets. *Acta Astronautica*, 44:607–623, 1999.

[37] Heather Franz. Design of Earth Return Orbits for the Wind Mission. In *Proceedings of the 12th Spaceflight Mechanics Meeting*, pages 845–865, 2003.

[38] Pradipto Ghosh and Bruce a. Conway. Numerical Trajectory Optimization with Swarm Intelligence and Dynamic Assignment of Solution Structure. *Journal of Guidance, Control, and Dynamics*, 35(4):1178–1192, 2012.

[39] Jesus Gil-Fernandez, Raul Cadenas, and Mariella Graziano. Analysis of Manned Missions to Near Earth Asteroids. In *Proceedings of the 20th AAS/AIAA Spaceflight Mechanics Meeting*, volume 136, pages 2115–2127, 2010.

[40] Philip E. Gill, Walter Murray, and Michael a. Saunders. SNOPT: An SQP Algorithm for Large-Scale Constrained Optimization. *SIAM Journal on Optimization*, 12(4):979–1006, 2002.

[41] Paul Ricord Griesemer, Cesar Ocampo, and D. S. Cooley. Targeting Ballistic Lunar Capture Trajectories Using Periodic Orbits. *Journal of Guidance, Control, and Dynamics*, 34(3):893–902, 2011.

[42] I. S. Grigoriev and M. P. Zapletin. One Optimization Problem for Trajectories of Spacecraft Rendezvous Mission to a Group of Asteroids. *Cosmic Research*, 47(5):426–437, 2009.

[43] Andrew F Heaton, Nathan J Strange, James M Longuski, and Eugene P Bonfiglio. Automated Design of the Europa Orbiter Tour. *Journal of Spacecraft and Rockets*, 39(1):17–22, 2002.

[44] S. Hernandez and B. Barbee. Design of Round-Trip Trajectories to Near-Earth Asteroids Utilizing a Lunar Flyby. In *Proc. 21st AAS/AIAA Space Flight Mechanics Meeting, New Orleans, Louisiana*, 2011.

[45] Ernest R. Hillje. Entry Aerodynamics at Lunar Return Conditions Obtained from the Flight of Apollo 4. Technical report, 1969.

[46] Alan C. Hindmarsh. DLSODE, 1983. ODEPACK, A Systemized Collection of ODE Solvers. Scientific Computing, R. S. Stepleman, et al.

[47] W. M. Hollister. Periodic Orbits for Interplanetary Flight. *Journal of Spacecraft and Rockets*, 6(4):366–369, 1969.

[48] D. C. Hyland, H. a. Altwaijry, R. Margulieux, J. Doyle, J. Sandberg, B. Young, N. Satak, J. Lopez, S. Ge, and X. Bai. A Mission Template for Exploration and Damage Mitigation of Potential Hazard of Near Earth Asteroids. *Cosmic Research*, 48(5):437–442, 2010.

[49] V. V. Ivashkin. On Trajectories of Spacecraft Re-Entry from a Geostationary Orbit to Earth Using Lunar Gravity Assist. *Doklady Physics*, 51(8):450–453, 2006.

[50] Dario Izzo, Luís F. Simões, Marcus Märtens, Guido C.H.E. de Croon, Aurelie Heritier, and Chit Hong Yam. Search for a Grand Tour of the Jupiter Galilean Moons. In *Proceedings of the 15th Annual conference on Genetic and evolutionary computation conference - GECCO '13*, pages 1301–1308. ACM Press, 2013.

[51] Mark Jesick and Cesar Ocampo. Computation and Optimization of Lunar Orbit Insertion from a Fixed Free Return. *The Journal of the Astronautical Sciences*, 58(1):35–53, 2011.

[52] Mark Jesick and Cesar A Ocampo. Optimal Lunar Orbit Insertion from a Variable Symmetric Free-Return Trajectory. *Journal of Guidance, Control, and Dynamics*, 34(6):1867–1875, 2011.

[53] Mark C Jesick and Cesar A Ocampo. Automated Generation of Symmetric Lunar Free-Return Trajectories. *Journal of Guidance, Control, and Dynamics*, 34(1):98–106, 2011.

[54] James Kennedy and Russell Eberhart. Particle Swarm Optimization. In *Proceedings of the IEEE International Conference on Neural Networks*, pages 1942–1948, 1995.

[55] C.A. Kluever. Comet Rendezvous Mission Design Using Solar Electric Propulsion Spacecraft. *Journal of Spacecraft and Rockets*, 37(5):698–700, 2000.

[56] Jet Propulsion Laboratory. JPL HORIZONS System. Accessible on-line at `http://ssd.jpl.nasa.gov/?horizons`. Accessed 11 August 2014.

[57] Damon Landau and Nathan Strange. Near-Earth Asteroids Accessible to Human Exploration with High-Power Electric Propulsion. In *Proceedings of the AAS/AIAA Astrodynamics Specialist Conference*, pages 635–654, 2011.

[58] Damon F Landau and James M Longuski. Trajectories for Human Missions to Mars, Part 1: Impulsive Transfers. *Journal of Spacecraft and Rockets*, 43(5):1035–1042, 2006.

[59] Gregory Lantoine and Ryan P Russell. Near Ballistic Halo-to-Halo Transfers between Planetary Moons. *Journal of the Astronautical Sciences*, 58(3):335–363, 2011.

[60] CO Lau and ND Hulkower. Accessibility of Near-Earth Asteroids. *Journal of Guidance*, 10(3):225–232, 1987.

[61] M. a. LeCompte, T. R. Meyer, J. Horsewood, C. P. McKay, and D. D. Durda. Early, Short-Duration, Near-Earth-Asteroid Rendezvous Missions. *Journal of Spacecraft and Rockets*, 49(4):731–741, 2012.

[62] Qinqin Luo, Jianfeng Yin, and Chao Han. Design of Earth-Moon Free-Return Trajectories. *Journal of Guidance, Control, and Dynamics*, 36(1):263–271, 2013.

[63] Belinda G. Marchand, Kathleen C. Howell, and Roby S. Wilson. Improved Corrections Process for Constrained Trajectory Design in the n-Body Problem. *Journal of Spacecraft and Rockets*, 44(4):884–897, 2007.

[64] Pierre Martinon, Frederic Bonnans, Julien Laurent-Varin, and Emmanuel Trelat. Numerical Study of Optimal Trajectories with Singular Arcs for an Ariane 5 Launcher. *Journal of Guidance, Control, and Dynamics*, 32(1):51–55, 2009.

[65] Joaquim R R A Martins, Peter Sturdza, and Juan J Alonso. The Complex-Step Derivative Approximation. *ACM Transactions on Mathematical Software*, 29(3):245–262, 2003.

[66] Gregory L. Matloff and Monika Wilga. NEOs as Stepping Stones to Mars and Main-Belt Asteroids. *Acta Astronautica*, 68(5-6):599–602, 2011.

[67] James V McAdams, David W Dunham, Robert W Farquhar, Anthony H Taylor, and B G Williams. Trajectory Design and Maneuver Strategy for the MESSENGER Mission to Mercury. *Journal of Spacecraft and Rockets*, 43(5):1054–1064, 2011.

[68] G Mengali and Alessandro A Quarta. Rapid Solar Sail Rendezvous Missions to Asteroid 99942 Apophis. *Journal of Spacecraft and Rockets*, 46(1):134–140, 2009.

[69] A Miele, T Wang, and S Mancuso. Optimal Free-Return Trajectories for Moon Missions and Mars Missions. *The Journal of the Astronautical Sciences*, 48(2 and 3):183–206, 2000.

[70] Yasuhiro Morita, Jun'ichiro Kawaguchi, Yoshifumi Inatani, and Takashi Abe. Demonstrator of Atmospheric Reentry System with Hyperbolic VelocityDASH. *Acta Astronautica*, 52(1):29–39, 2003.

[71] NASA. Apollo 8 Press Kit. Technical report, 1968.

[72] A. Nathues, H. Boehnhardt, A.W. Harris, C. Jentsch, S. Schaeff, F. Weischede, A. Wiegand, N. Schmitz, W. Goetz, and Z. Kachri. ASTEX: An In Situ Exploration Mission to Two Near-Earth Asteroids. *Advances in Space Research*, 45(1):169–182, 2010.

[73] Cesar Ocampo. Trajectory Analysis for the Lunar Flyby Rescue of AsiaSat-3/HGS-1. *Annals of the New York Academy of Sciences*, 1065:232–253, December 2005.

[74] Cesar Ocampo and Jean-Philippe Munoz. Variational Equations for a Generalized Spacecraft Trajectory Model. *Journal of Guidance, Control, and Dynamics*, 33(5):1615–1622, 2010.

[75] R. C. Paffenroth, E. J. Doedel, and D. J. Dichmann. Continuation of Periodic Orbits Around Lagrange Points and AUTO2000. In *Advances in the Astronautical Sciences*, pages 41–60, 2001.

[76] Sang-Young Park and Kyu-Hong Choi. Optimal Low-Thrust Intercept/Rendezvous Trajectories to Earth-Crossing Objects. *Journal of Guidance, Control, and Dynamics*, 28(5):1049–1055, 2005.

[77] Sang-young Park and I Michael Ross. Two-Body Optimization for Deflecting Earth-Crossing Asteroids. *Journal of Guidance, Control, and Dynamics*, 22(3):415–420, 1999.

[78] Moonish R. Patel, James M. Longuski, and Jon. A Sims. Mars Free Return Trajectories. *Journal of Spacecraft and Rockets*, 35(3):350–354, 1998.

[79] QiBo Peng, HongXin Shen, and HaiYang Li. Free Return Orbit Design and Characteristics Analysis for Manned Lunar Mission. *Science China Technological Sciences*, 54(12):3243–3250, 2011.

[80] Ettore Perozzi, Lorenzo Casalino, Guido Colasurdo, Alessandro Rossi, and Giovanni B Valsecchi. Resonant Fly-By Missions to Near Earth Asteroids. *Celestial Mechanics and Dynamical Astronomy*, 83:49–62, 2002.

[81] Ettore Perozzi, Alessandro Rossi, and Giovanni B Valsecchi. Basic Targeting Strategies for Rendezvous and Flyby Missions to the Near-Earth Asteroids. *Planetary and Space Science*, 49:3–22, 2001.

[82] Gautier Picot. Shooting and Numerical Continuation Methods for Computing Time-Minimal and Energy-Minimal Trajectories in the Earth-Moon System using Low Propulsion. *Discrete and Continuous Dynamical Systems - Series B*, 17(1):245–269, 2011.

[83] Mauro Pontani and Bruce A Conway. Particle Swarm Optimization Applied to Space Trajectories. *Journal of Guidance, Control, and Dynamics*, 33(5):1429–1441, 2010.

[84] Mauro Pontani, Pradipto Ghosh, and Bruce a. Conway. Particle Swarm Optimization of Multiple-Burn Rendezvous Trajectories. *Journal of Guidance, Control, and Dynamics*, 35(4):1192–1207, 2012.

[85] Dong Qiao, Hutao Cui, and Pingyuan Cui. The Design of Transfer Trajectory for Ivar Asteroid Exploration Mission. *Acta Astronautica*, 65(11-12):1553–1560, 2009.

[86] Dong Qiao, Pingyuan Cui, and Hutao Cui. The Nereus Asteroid Rendezvous Mission Design with Multi-Objective Hybrid Optimization. In *Proceedings*

of the Systems and Control in Aerospace and Astronautics Conference, number Ld, pages 587–592. IEEE, 2006.

[87] Dong Qiao, Pingyuan Cui, and Hutao Cui. Proposal for a Multiple-Asteroid-Flyby Mission with Sample Return. *Advances in Space Research*, 50(3):327–333, 2012.

[88] Alessandro A Quarta and G Mengali. Electric Sail Missions to Potentially Hazardous Asteroids. *Acta Astronautica*, 66(9-10):1506–1519, 2010.

[89] Marc D. Rayman, Thomas C. Fraschetti, Carol a. Raymond, and Christopher T. Russell. Dawn: A Mission in Development for Exploration of Main Belt Asteroids Vesta and Ceres. *Acta Astronautica*, 58(11):605–616, 2006.

[90] Ryan P Russell and Cesar A Ocampo. A Geometric Analysis of Half and Full-Revolution Return Trajectories via Planetary Flybys. *Advances in the Astronautical Sciences*, (August), 2004.

[91] Ryan P Russell and Cesar A Ocampo. Systematic Method for Constructing Earth Mars Cyclers Using Free-Return Trajectories. *Journal of Guidance, Control, and Dynamics*, 27(3):321–335, 2004.

[92] Ryan P Russell and Cesar A Ocampo. Geometric Analysis of Free-Return Trajectories Following a Gravity-Assisted Flyby. *Journal of Spacecraft and Rockets*, 42(1):138–151, 2005.

[93] Ryan P Russell and Cesar A Ocampo. Global Search for Idealized Free-Return EarthMars Cyclers. *Journal of Guidance, Control, and Dynamics*, 28(2):194–208, 2005.

[94] Ryan P. Russell and Cesar A. Ocampo. Optimization of a Broad Class of Ephemeris Model Earth-Mars Cyclers. *Journal of Guidance, Control, and Dynamics*, 29(2):354–367, 2006.

[95] Ryan P. Russell and Nathan J. Strange. Cycler Trajectories in Planetary Moon Systems. *Journal of Guidance, Control, and Dynamics*, 32(1):143–157, 2009.

[96] J. P. Sanchez and C. McInnes. Asteroid Resource Map for Near-Earth Space. *Journal of Spacecraft and Rockets*, 48(1):153–165, 2011.

[97] Russell L. Schweickart. Decision Program on Asteroid Threat Mitigation. *Acta Astronautica*, 65(9-10):1402–1408, 2009.

[98] K. Seidelmann. *Explanatory Supplement to the Astronomical Almanac*. University Science Books, California, 1992.

[99] EM Shoemaker and EF Helin. Earth-approaching Asteroids as Targets for Exploration. In *NASA Conference Publication*, volume 2053, pages 245–256, 1978.

[100] Michael a. Shoemaker, Jozef C. van der Ha, and Kazuhisa Fujita. Trajectory Reconstruction of Hayabusa's Atmospheric Reentry. *Acta Astronautica*, 71:151–162, 2012.

[101] Christopher M Spreen, Michael J Mueterthies, Kevin W Kloster, and James M Longuski. Preliminary Analysis of Ballistic Trajectories to Uranus Using Gravity-Assists from Venus, Earth, Mars, Jupiter, and Saturn. In *Proceedings of the AAS/AIAA Astrodynamics Specialist Conference*, pages 3411–3428, 2011.

[102] E.M. Standish, 1998. JPL Planetary and Lunar Ephemerides, DE405/LE405. JPL IOM 312.F-98-048.

[103] Nathan J. Strange and James M. Longuski. Graphical Method for Gravity-Assist Trajectory Design. *Journal of Spacecraft and Rockets*, 39(1):9–16, 2002.

[104] A. A. Sukhanov, H. F. De C. Velho, E. E. Macau, and O. C. Winter. The Aster project: Flight to a Near-Earth Asteroid. *Cosmic Research*, 48(5):443–450, 2010.

[105] V. Szebehely. *Theory of Orbits: The Restricted Problem of Three Bodies*. Academic Press, New York, 1967.

[106] B. Tapley, B. Schutz, and G. Born. *Statistical Orbit Determination*. Elsevier, Burlington, MA, 2004.

[107] Paul V Tartabini, Scott A Striepe, and Richard W Powell. Abort Options for Potential Mars Missions. *Journal of Spacecraft and Rockets*, 31(4):543–549, 1994.

[108] M E Tauber, G E Palmer, and Lily Yang. Earth Atmospheric Entry Studies for Manned Mars Missions. *Journal of Thermophysics and Heat Transfer*, 6(2):193–199, 1992.

[109] D. Vallado. *Fundamentals of Astrodynamics and Applications, Third ed.* Springer, New York, NY, 2007.

[110] Gerhard Venter and Jaroslaw Sobieszczanski-Sobieski. Particle Swarm Optimization. *AIAA Journal*, 41(8):1583–1589, 2003.

[111] R. L. Wagner. The Impact of Free Return Missions on the Apollo System. Technical report, 1966.

[112] Sam Wagner and Bong Wie. Target Asteroid Selection for Human Exploration of Near Earth Objects. In *Proceedings of the 20th AAS/AIAA Spaceflight Mechanics Meeting*, volume 136, pages 2205–2224, 2010.

[113] Roby S Wilson and Kathleen C Howell. Trajectory Design in the Sun Earth Moon System Using Lunar Gravity Assists. *Journal of Spacecraft and Rockets*, 35(2):191–198, 1998.

[114] A.A. Wolf. Free Return Trajectories for Mars Missions. In *Proceedings of the 1st Annual Spaceflight Mechanics Meeting*, volume 1, pages 317–329, 1991.

[115] A.A. Wolf and J.C. Smith. Design of the Cassini Tour Trajectory in the Saturnian System. *Control Engineering Practice*, 3(11):1611–1619, 1995.

[116] Kazuyuki Yagasaki. Computation of Low Energy Earth-to-Moon Transfers with Moderate Flight Time. *Physica D: Nonlinear Phenomena*, 197(3-4):313–331, 2004.

[117] Tetsuya Yamada, Yoshifumi Inatani, Masahisa Honda, and Ken'ich Hirai. Development of Thermal Protection System of the Muses-C/DASH Reentry Capsule. *Acta Astronautica*, 51(1-9):63–72, 2002.

[118] A.K. Zimmer and E. Messerschmid. Going beyond: Target Selection and Mission Analysis of Human Exploration Missions to Near-Earth Asteroids. *Acta Astronautica*, 69(11-12):1096–1109, 2011.

Vita

Nicholas (Nick) Bradley was born in Boulder, Colorado in 1988 to John and Terry Bradley. He grew up in Boulder, and attended the University of Colorado at Boulder from 2005 to 2010. Nick received concurrent B.S. and M.S. degrees from the Department of Aerospace Engineering and Engineering Sciences in May 2010, and began his doctoral work at The University of Texas at Austin in August 2010. He worked with Dr. Cesar Ocampo and Dr. Ryan Russell during his time at UT-Austin. Nick has held several internships at aerospace-related companies (Ball Aerospace, NASA-JPL, SpaceNav LLC), and will be starting a full-time position at NASA-JPL in September 2014. In June 2013, Nick married Rachel Wildrick, and the two are currently finishing their last summer in Austin. The couple will soon pack up for Pasadena, California and head west to more adventures together...

Author's e-mail address: astrobradley-at-gmail.com

This dissertation was typeset with LaTeX[†] by the author.

[†]LaTeX is a document preparation system developed by Leslie Lamport as a special version of Donald Knuth's TeX Program.